Fermi-surface investigations of rare-earth transition-metal compounds

DISSERTATION

zur Erlangung des akademischen Grades

Doctor rerum naturalium
(Dr. rer. nat.)

vorgelegt

der Fakultät
Mathematik und Naturwissenschaften

TECHNISCHE
UNIVERSITÄT
DRESDEN

von

Andrey Polyakov
geboren am 15.01.1985 in Lipetzk, Russland

HLD.

HELMHOLTZ
ZENTRUM DRESDEN
ROSSENDORF

HOCHFELD-MAGNETLABOR DRESDEN
Helmholtz-Zentrum Dresden-Rossendorf
2013

GUTACHTER:

Prof. Dr. Joachim Wosnitza
Prof. Dr. Andrea Bianchi

Eingereicht am: 6. Dezember 2012
Tag der Verteidigung: 29. April 2013

Content

1. Introduction

Owing to significant technological advances, mainly in the growth of new complex rare-earth transition-metal compounds, their fascinating physical properties, arising from incompletely filled d- or f-electron shells with narrow energy bands, attract considerable scientific interest [1]. In some of these materials, the picture of non-interacting free electrons, which describes simple metals well, is not applicable anymore. Instead, interactions between electrons play a crucial role and many new states of matter such as quantum critical points (QCPs), non-Fermi-liquid (NFL) behavior, magnetic order, superconductivity and many others can emerge [2]. These materials are often classified as strongly correlated electron systems and two of the most intriguing classes among this family are the heavy-fermion compounds and the high-temperature superconductors.

In order to understand the mechanism of superconductivity and the role of electronic correlations in these systems the knowledge of the Fermi-surface topology is a prerequisite. In particular, topological changes of the electronic structure upon elemental substitution may give valuable information on the importance of certain bands for the superconducting state. Measurements of quantum oscillations in the magnetization, called de Haas-van Alphen (dHvA) effect, in combination with band-structure calculations are a powerful tool to gain unique information regarding the full three-dimensional topology of the Fermi surface and the renormalization of the band-selective quasiparticle effective masses.

In the course of this work, the Fermi-surface properties of several important representatives of strongly correlated materials have been studied using the de Haas-van Alphen effect.

The results contained in this thesis are organized as follows:

Chapter 2 includes general background of the unusual properties and open physical questions relating the classes of materials that are considered in the core of this thesis.

In Chapter 3 the physical origin of the de Haas-van Alphen oscillations and the effect of a two-dimensional nature of a material to the Fermi surface are outlined. The standard Lifshitz-Kosevich (LK) expression together with the effects of the damping factors are described as well.

Chapter 4 introduces the experimental technique used to detect the dHvA oscillations as well as the available installations to provide the required experimental conditions that were used in this project.

Chapter 5 presents the results of a systematic study of the Fermi-surface, effective-mass, and scattering-rate evolution in $Ce_{1-x}Yb_xCoIn_5$ as a function of the Yb concentration. The quantum-oscillation measurements were realized by means of a capacitive cantilever-torque technique. The angular-resolved dHvA frequencies for both end members $CeCoIn_5$ and $YbCoIn_5$ are very well described by conventional density-functional-theory (DFT) calculations. The Yb-$4f$ occupation number has also been evaluated yielding the results indicating an intermediate Yb valence.

Chapter 6 deals with the comprehensive de Haas-van Alphen measurements performed on the iron-based ternary phosphides $LaFe_2P_2$ and $CeFe_2P_2$. These compounds are isostructural to the high-T_c iron-based superconductor $Ba_{1-x}K_xFe_2As_2$. The angular-dependent observation of the dHvA frequencies show good agreement with DFT calculations for $LaFe_2P_2$. However, for $CeFe_2P_2$ strong disagreement between the calculated and experimentally obtained data was observed. The band-selective effective masses and the mass enhancements at some distinct orientations have also been determined.

The main results obtained during this work are summarized in Chapter 7.

The appendix contains a combined theoretical and experimental investigation of the Fermi-surface properties of the filled skutterudite superconductor $PrPt_4Ge_{12}$.

2. General aspects

2.1. Unconventional superconductivity

Superconductivity, the resistance-free flow of electrical charge, is an amazing phenomenon that was discovered by Kamerlingh Onnes at the University of Leiden in 1911 [3]. Since its first observation in Hg, condensed-matter physicists were fascinated by this effect, which until now is one of the most studied phenomena. Despite the fact, that over the years superconductivity has been found in many other elements and alloys, it required more than half a century to develop a theory able to explain such an exotic low-temperature state of matter on a microscopic level. Started by the ground-breaking work of Cooper in 1956 [4] and Bardeen, Cooper, and Schrieffer (BCS) in 1957 [5], these ideas instantly established into an elegant theory which gave a microscopic explanation of superconductivity by means of singlet Cooper pairs ($\mathbf{k}\uparrow$, $-\mathbf{k}\downarrow$) forming in an energy shell $\hbar\omega_\mathrm{D}$ (ω_D is the Debye frequency) around the Fermi energy ε_F as a result of the electron-phonon interaction.

Not long after the rigorous BCS work it has been suspected that magnetic interactions between the electron spins can also be sufficiently large to give rise to a superconducting state with the Cooper-pair wave function having non-s-wave symmetry. Experimental indication for such an unconventional form of superconductivity, which does not follow to the BCS theory, have been achieved along with the discovery of the first heavy-fermion superconductor in 1979 [6].

Within a short period, several novel classes of superconducting materials such as organics, high-T_c copper oxides, Fe-based pnictides, filled skutterudites, and many others have been discovered. Most of these materials have largely different properties compared to traditional superconductors.

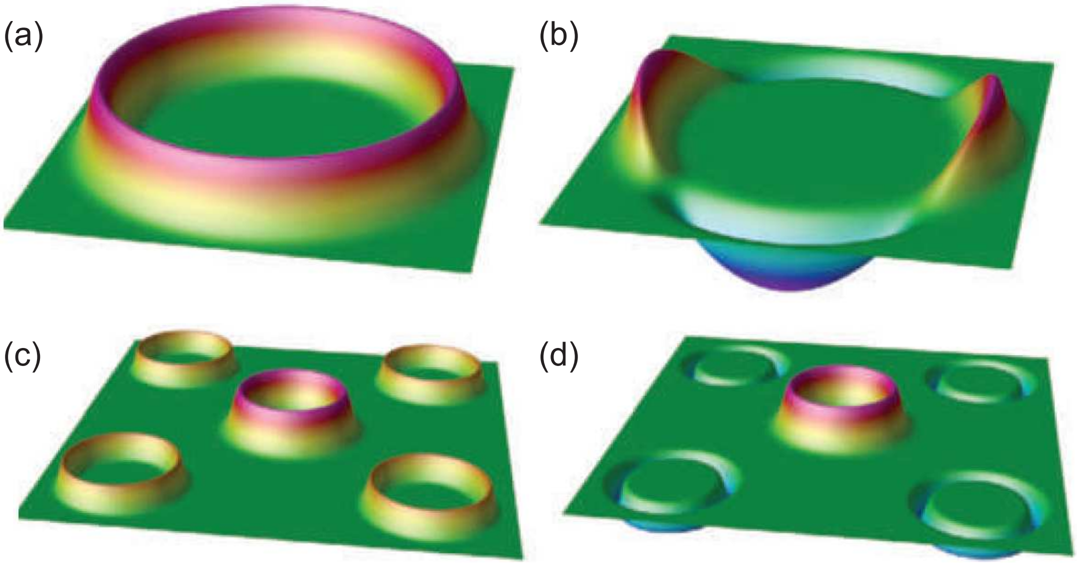

Figure 2.1.: *A schematic representation of the superconducting order parameter in different cases [7]: (a) a conventional s-wave; (b) a d-wave, as is the case in copper oxides; (c) a two-band s-wave with the same sign, as in* MgB_2*; (d) an* $s_{\pm}$ *wave, as is thought to be the case in iron-based superconductors. In (a) and (b), the two-dimensional Fermi surface is approximated by one circle. In (c) and (d), the Fermi surface is approximated by a small circle in the centre surrounded by four larger circles. In all cases, the height of the "rubber sheet" is proportional to the magnitude of the order parameter.*

As a consequence, assumed that for these materials superconductivity arises from a different source than the conventional electron-phonon interactions that are essential in the BCS theory.

In conventional superconductors, superconductivity is mediated by phonons, and the electrons are paired in singlet states with zero angular momentum (*s*-wave type). Thereby, an isotropic superconducting energy gap is developed near the Fermi surface. In unconventional superconductors, the electrons are paired in states with angular momentum greater than zero (*p*- or *d*-wave superconductivity) and characterized by a superconducting order parameter that changes sign in momentum space along certain directions in the Brillouin zone, as is shown in Fig. 2.1. Therefore an anisotropic energy gap vanishes on point nodes or along lines of nodes on the Fermi surface.

However, despite intensive research and many promising ideas, a final experimental determination of what is the origin of the complex attractive forces between electrons giving rise to unconventional superconductivity, so far, remains open.

2.2. The iron-based pnictides

"At the extreme forefront of research in superconductivity is the empirical search for new materials" [8]. With the discovery of high-transition-temperature superconductivity in layered copper-based oxide $La_{2-x}Ba_xCuO_4$ [9] in 1986, a new era of great excitement for the condensed-matter physics community had been initiated. Before and after that, extensive efforts were dedicated to the finding of new transition-metal-based superconductors [10,11], but the T_c of non-Cu-based materials in this category had remained low [12,13].

For about 20 years, only copper oxides opened up the possibility to reach high-temperature superconductivity, but another material class appeared with the discovery of superconductivity in layered iron-based materials by Hosono's group, first in LaFePO ($T_c \approx 3\,\mathrm{K}$) [14] in 2006 and next in fluorine-doped LaFeAsO ($T_c = 26\,\mathrm{K}$) [15] in 2008. Within a short period, the superconducting transition temperature had been increased up to 43 K under high pressure of $\approx 4\,\mathrm{GPa}$ [16], and then reached values up to about 55 K by replacing La by other rare-earth elements (Ce [17], Sr [18], Sm [19], Nd [20], Pr [21], Gd [22], etc. [23]).

Various homologous series of iron-based compounds with different crystal structures were found to support superconductivity. Those families are named after the stoichiometries of their parental prototypes such as "11" of FeSe [24] and $Fe(Se_{1-x}Te_x)_{0.82}$ [25], "111" of LiFeAs [26,27] and NaFeAs [28], "1111" of LaFePO [14] and LaFeAsO [15], "122" of $Ba_{1-x}K_xFe_2As_2$ [29] and $Ba(Fe_{1-x}Co_x)_2As_2$ [30], and more complex layered structures such as "32522" of $(Sr_3Sc_2O_5)Fe_2As_2$ [31] and "42622" of $Sr_4V_2O_6Fe_2As_2$ [32]. Each of these structures, shown in Fig. 2.2, has a common two-dimensional layer based on a square lattice of iron atoms combined with two square lattices of pnictogen (P, As, Sb) or chalcogen (S, Se, Te) atoms.

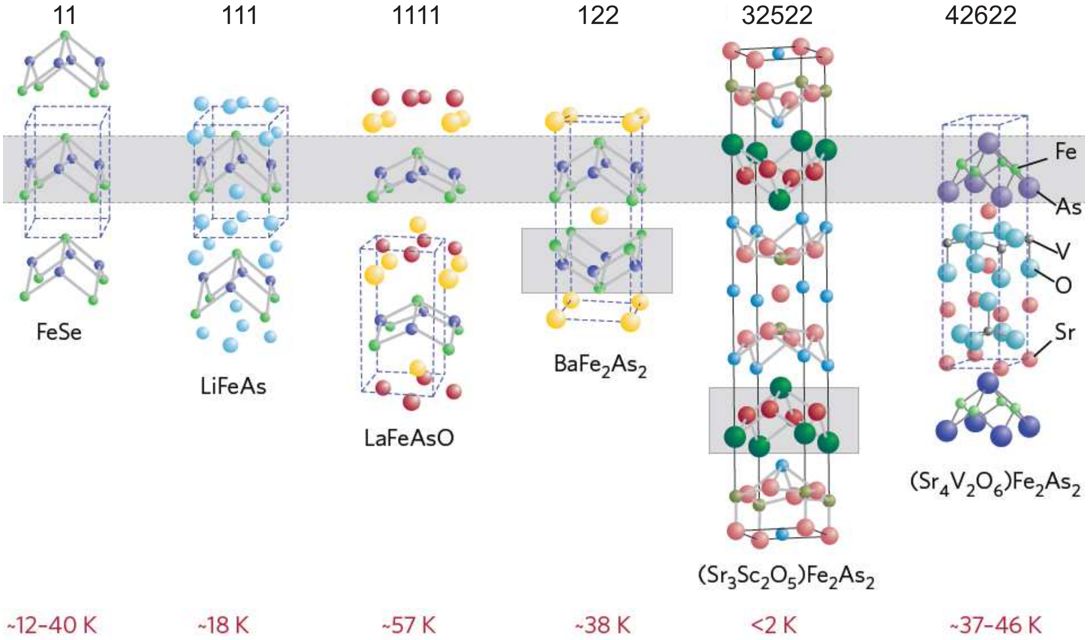

Figure 2.2.: *Six homologous tetragonal crystallographic structures known to support superconductivity in iron-based materials. The temperature stated below each structure is the highest achieved* T_c *up to date for each family [33].*

Up to now, the origin of high-temperature superconductivity in the Fe-based superconductors remains unclear and a highly debated question of primary importance. Many theoretical studies proposed various possible scenarios for the superconducting order parameter in these superconductors. The most popular candidate, focusing on the nesting tendency between cylindrical electron- and hole-like Fermi surfaces, is an electron pairing mediated by antiferromagnetic spin fluctuations with unconventional $s_{\pm}$ pairing symmetry [34–36]. On the other side, there is a theoretical model, based on the multiorbital nature of the iron pnictides, that links superconductivity to orbital ordering [37–39]. This model argues for the superconducting pairing through orbital fluctuations [40–43] or orbital fluctuations mixed with spin fluctuations [44, 45].

Extensive experiments trying to probe the symmetry of the superconducting phase, and thereby helping to elucidate the pairing mechanism of the iron-based high-temperature superconductors have been performed, but the outcome, so far, is quite controversial. A pairing state with a sign reversal of the order parameter between different Fermi-surface sheets is consistent with scanning tunneling microscopy on Fe(Te,Se) [46] and inelastic neutron spectroscopy on (Ba,K)Fe_2As_2 [47], an $s_\pm$-wave symmetry possibly caused by spin fluctuations. The robustness of T_c as a function of the impurities in LaFeAs(O,F) [48] inspires a possible s_{++}-wave superconductivity, which may be caused by orbital fluctuations or a balance of these two pairing mechanisms possibly leading to a crossover from $s_\pm$ to s_{++} symmetry. Bulk-sensitive laser angle-resolved photoemission spectroscopy on P/K-doped $BaFe_2As_2$ [49] reveals an orbital-independent superconducting gap magnitude for the whole Fermi surfaces, which is in strong contradiction to the superconductivity associated with spin fluctuations. In addition, the spin and orbital degrees of freedom might be strongly coupled for the parent and superconducting compounds [44, 45, 50–52].

Despite a tremendous number of publications on the iron-based pnictides, the origin of high-temperature superconductivity in this class of material is still puzzling. Due to the wide variety of different iron-pnictide families and the diverse possible chemical substitutions, experiments taken on different systems or different compounds of the same structural type lead sometimes to controversial results. Further work is needed to provide new or to complement present-day theories of superconductivity in this class of materials.

2.3. The Fulde-Ferrell-Larkin-Ovchinnikov state

In 1964, P. Fulde and R.A. Ferrell (FF) [53], and independently A.I. Larkin and Y.N. Ovchinnikov (LO) [54] have theoretically predicted the existence of novel inhomogeneous superconducting states at high magnetic fields and low temperatures characterized by the formation of Cooper pairs with nonzero total momentum ($\mathbf{k}\uparrow$, $-\mathbf{k} + \mathbf{q}\downarrow$), instead of the ordinary BCS pairs ($\mathbf{k}\uparrow$, $-\mathbf{k}\downarrow$). This superconducting state that belongs to another class of unconventional superconductivity is nowadays known as the

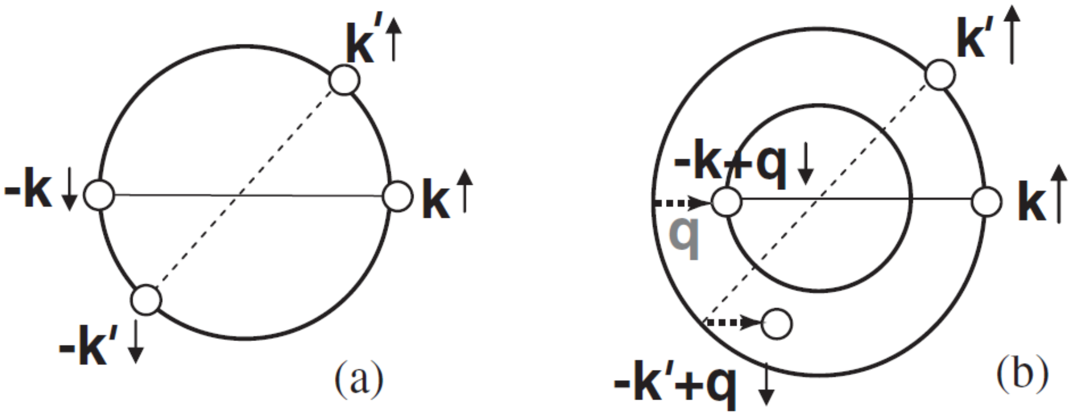

Figure 2.3.: *Schematic figure of pairing states [55]. (a) BCS pairing state (**k**↑, -**k**↓). (b) FFLO pairing state (**k**↑, -**k** + **q**↓). The inner and outer circles represent the Fermi surface of the spin down and up bands, respectively. The electron with -**k′** + **q**↓ is not on the inner Fermi surface.*

Fulde-Ferrell-Larkin-Ovchinnikov state, abbreviated FFLO state (also LOFF state). A fascinating aspect of the FFLO state is that it exhibits inhomogeneous superconducting phases with a spatially oscillating order parameter and spin polarization [55].

Since its first prediction, experimental evidence of the FFLO state has been searched for in different classes of superconducting materials, first in thin films and later in exotic superconductors such as heavy-fermion [55–57] and organic [58] superconductors. However, a number of claims stating possible evidence of such a state later had to be revised or are inconclusive [59], mainly because of the very stringent conditions essential to be realized.

In order that the FFLO state appears in type-II spin-singlet superconducting materials, it is required that:

- the orbital critical field, B_{orb}, is sufficiently larger than the Pauli paramagnetic limit
  $$B_{\mathrm{P}} = \frac{\Delta_0}{2\mu_{\mathrm{B}}} < B_{orb}, \tag{2.1}$$
  where μ_{B} is the Bohr magneton and Δ_0 is the superconducting energy gap at $T = 0$ [60].

More precisely, the Maki parameter [61] should be larger than 1.8 [62]

$$\alpha = \sqrt{2}\frac{B_{orb}}{B_{\mathrm{P}}} > 1.8, \tag{2.2}$$

- the superconductor must be in the clean limit with a mean free path much larger than the coherence length

$$\ell \gg \xi. \tag{2.3}$$

Nowadays very few systems fulfill these necessary conditions for exhibiting the FFLO state. Prime candidates showing strong indication for FFLO are the quasi-two-dimensional organic superconductors [63–65].

2.4. Heavy-fermion physics

The class of heavy-fermion materials belongs to the group of strongly correlated electron systems. This family has emerged as prototypical to study quantum criticality and unconventional superconductivity. In 1975 heavy-fermion behavior was discovered by observing an enormous magnitude of the linear specific-heat coefficient in $CeAl_3$ [66] . Although it was widely thought, that the existence of localized magnetic moments and superconductivity in one material is incompatible, the opposite was shown in 1979 by the discovery of superconductivity in the heavy-fermion compound $CeCu_2Si_2$ [6]. Since that time, the list of this class of materials has rapidly expanded including now more than twenty Ce, Yb, U, Pu, and Pr representatives [67].

In these compounds, the Ruderman-Kittel-Kasuya-Yosida (RKKY) interaction and the Kondo effect compete with each other. This competition is shown schematically in Fig. 2.4 as a function of the magnitude of the magnetic exchange interaction strength, J_{cf}, and the electron density of states at the Fermi level, $D(\varepsilon_F)$ [68].

At room temperature, heavy-fermion materials behave like normal metals and the electrons can be described as a Fermi liquid, where the f-electrons

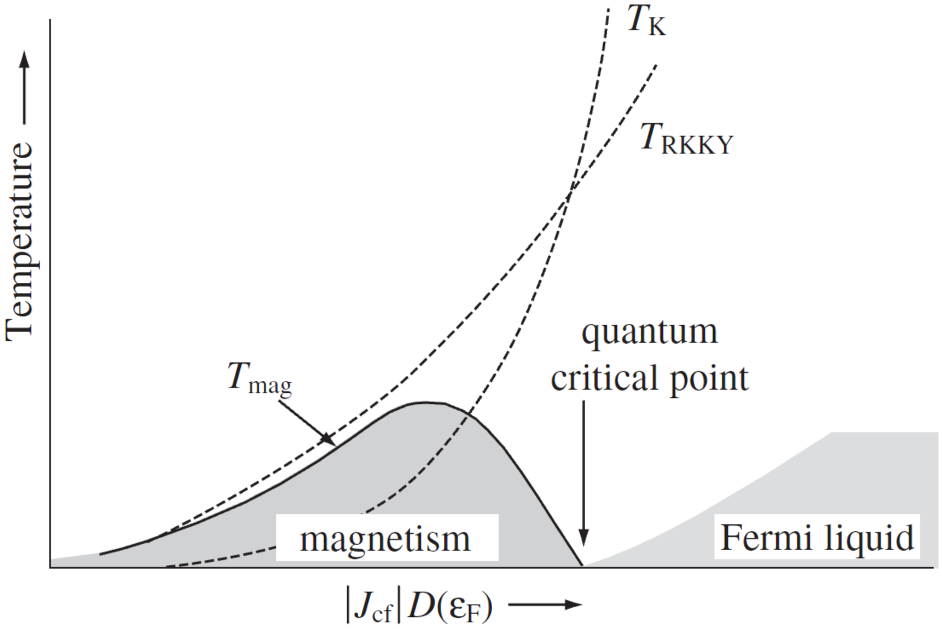

Figure 2.4.: *Doniach's phase diagram indicating competition between the RKKY interaction and the Kondo effect [69]. At the RKKY characteristic temperature, T_{RKKY}, magnetic order occurs in the absence of Kondo screening. Below the Kondo temperature, T_K, the local moments are screened by conduction electrons, giving rise to heavy-fermion behavior. A quantum critical point appears when magnetic ordering temperature, T_{mag}, is suppressed to zero by applying an external control parameter.*

interact weakly with the conduction electrons. With decreasing temperature the RKKY interaction enhances the long-range magnetic order, where the f electrons with the magnetic moments are treated as localized electrons and the indirect $f-f$ interaction is mediated by the spin polarization of the conduction electrons. The RKKY characteristic temperature is given by:

$$T_{\mathrm{RKKY}} \propto J_{cf}^2 D(\varepsilon_F). \tag{2.4}$$

At low temperatures, the properties of most heavy-fermion materials can no longer be described in terms of quasiparticles of the Landau-Fermi-liquid theory. Heavy-fermion behavior arises below a characteristic temperature (typically around 10 K) from the strong Kondo interactions between local moments of electrons in the partially filled f shells of the lanthanide

($4f$) or actinide ($5f$) atoms and itinerant conduction electrons. The Kondo characteristic temperature is described by:

$$T_{\mathrm{K}} \propto \exp(-1/J_{cf}D(\varepsilon_F)). \tag{2.5}$$

As a result of the Kondo effect a large number of low-energy excitations appears. In the ideal Fermi-liquid case these excitations correspond to heavy quasiparticles, whose effective mass m^* is up to several hundred times larger than the bare electron mass m_e. This large effective mass is also reflected in a highly enhanced electronic specific heat, magnetic susceptibility, and quadratic term in the resistivity. As a consequence of the existence of magnetic moments, magnetic ordering can also be observed in these materials at low temperatures [70].

By applying either a magnetic field or hydrostatic or chemically induced pressure the parameter $J_{cf}D(\varepsilon_F)$ can be varied. Thus, in many systems, it becomes possible to suppress the magnetic ordering temperature, T_{mag}, to zero giving rise to a quantum critical point. The discovery of a quantum critical point and non-Fermi-liquid behavior in the phase diagram of heavy-fermion compounds in 1994 led to a new rise of interest in the research of this system [71]. This may also trigger a transition to a superconducting state. The study of superconductivity in heavy-fermion compounds has led to a range of unexpected phenomena and new theories. In fact, local magnetic moments provide unpaired spins, thus destroying the formation of electron pairs, or Cooper pairs, that are usually responsible for superconductivity. That is why it is now widely suspected that heavy-fermion superconductivity is magnetically mediated.

2.5. Non-Fermi-liquid behavior and quantum criticality

At about the same time when Bardeen, Cooper, and Schrieffer established their rigorous BCS work, Landau proposed a phenomenological theory of Fermi liquids that became the standard model for the physics of metals, known as Landau-Fermi-liquid (FL) theory [72]. A key element in this theory is the idea of quasiparticles, i.e., states in the Fermi sea that carry the original charge and spin quantum numbers of the non-interacting particles from which they are derived, but whose mass m^* is renormalized by interactions [72–74]. It explains why some of the properties of an interacting fermion system are very similar to those of the Fermi gas (i.e., non-interacting fermions), and why other properties differ.

Low-lying excitations of the system according to the Fermi-liquid theory exhibit the following properties:

- one of the classic features is a quadratic temperature dependence of the electrical resistivity from its zero-temperature value,

$$\rho = \rho_0 + AT^2, \tag{2.6}$$

- a constant specific-heat coefficient,

$$\frac{C_{el}(T)}{T} = \text{const}, \tag{2.7}$$

  where C_{el} is the electronic part of the specific heat,

- a magnetic susceptibility that tends to a constant Pauli-like value,

$$\chi(T) = \text{const}. \tag{2.8}$$

The term non-Fermi-liquid behavior is used to label systems in which the basic assumptions of the standard Landau-Fermi-liquid theory, that at low energies the electrons in a metal should behave as a collection of weakly interacting particles, is violated. These non-Fermi-liquid systems display a deviation in their low-temperature thermodynamic and transport properties from those of normal metals. Examples for such deviations can be observed at quantum critical points in heavy-fermion metals and high-T_c copper oxides. In the proximity to a quantum critical point, which occurs at zero temperature at the critical value of a non-thermal external control parameter such as pressure, P, chemical doping, x, or magnetic field, B, two ordered ground states compete and the phase diagram is dominated by quantum

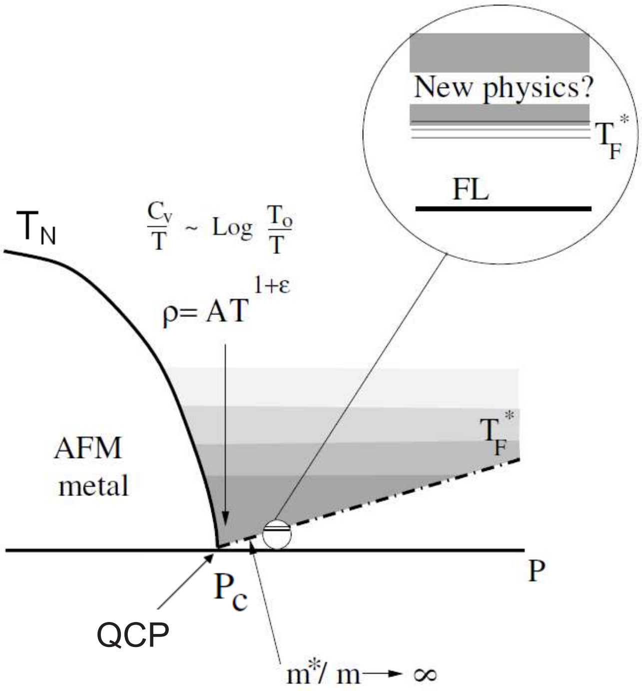

Figure 2.5.: *A schematic illustration of a typical phase diagram for a heavy-fermion metal possessing a quantum critical point [75]. Pressure drives the system from an antiferromagnetic state through a quantum critical point at* P_c*, into the paramagnetic phase below the characteristic temperature* T_F^**, where Fermi-liquid behavior appears. The inset emphasizes the point that if the characteristic temperature goes to zero at the quantum critical point, a new class of universal excitations, known as non-Fermi-liquid behavior, arises in the proximity to the quantum critical point in the region between* T_N *and* T_F^**.*

fluctuations. As the tuning parameter increases beyond the QCP, conventional Fermi-liquid behavior is recovered below a characteristic temperature T_F^*.

Figure 2.5 shows a typical phase diagram for heavy-fermion quantum critical systems, where the transition, at which the system changes from an antiferromagnetic to a paramagnetic metal, is tuned by pressure.

The properties of the metal are radically transformed by critical quantum fluctuations, departing qualitatively from the standard Fermi-liquid behavior. A metallic system containing a quantum critical point to which itinerant electrons have some coupling usually exhibits the following properties [75, 76]:

- Fermi-liquid behavior away from the quantum critical point at low temperatures,
- in the quantum critical region a quasi-linear temperature dependence in the resistivity,

  $$\rho \propto AT^{1+\varepsilon}, \tag{2.9}$$

  with ε in the range $0 - 0.6$,
- a divergent specific-heat coefficient at the critical point. In many cases, the divergence shows a logarithmic temperature dependence,

  $$\gamma(T) = \frac{C_{el}(T)}{T} = \gamma_0 \log \frac{T_0}{T}. \tag{2.10}$$

  This suggests that the characteristic temperature renormalizes to zero and the quasiparticle effective masses diverge,

  $$T_F^* \to 0, \tag{2.11}$$

  $$\frac{m^*}{m} \to \infty. \tag{2.12}$$
- A non-Curie-like spin susceptibility is expected as well,

  $$\chi^{-1}(T) = \chi_0^{-1} + cT^a. \tag{2.13}$$

The understanding of quantum critical point scenarios is of extensive current interest in condensed-matter physics as it can give rise to exotic finite-temperature properties. In addition, there is particular interest in these unusual metallic states, which are believed to promote the formation of novel phases, such as unconventional superconductivity or other unusual physical properties.

3. The de Haas-van Alphen effect

In this chapter, the nature of the quantum oscillations of the magnetization will be briefly outlined as it was first done by Onsager [77] and later by Gold [78], Springford [79], and Shoenberg [80]. This description is based on the semi-classical model of non-interacting Bloch electrons moving through a lattice of a crystal in a magnetic field. Using the Bohr-Sommerfeld quantization condition this model describes the occurrence of magnetic quantum oscillations.

3.1. Onsager relation

In the semi-classical picture the movement of free electrons through a crystal lattice in a magnetic field **B**, giving rise to the Lorentz force, described by

$$\mathbf{F} = -e(\mathbf{v} \times \mathbf{B}) = \hbar\dot{\mathbf{k}}(t), \tag{3.1}$$

where e is the elementary electronic charge, $\mathbf{v}$ is the group velocity of an electron wave packet normal to a surface of constant energy, and $\hbar\mathbf{k}$ is the crystal momentum change in the direction of constant energy, in a plane perpendicular to **B**.

Equation (3.1) can be integrated in time to lead to a direct relation between the trajectory in the real space and the momentum space (**k**-space)

$$\mathbf{k} - \mathbf{k_0} = \frac{-e}{\hbar}(\mathbf{r} - \mathbf{r_0}) \times \mathbf{B}. \tag{3.2}$$

In fact, this means that the projection of the trajectory of the electrons in real space on to a plane normal to **B** is related to that of the wave vector **k** in momentum space by a scaling factor $eB/\hbar$ and a rotation by 90°.

The basic cause for the presence of quantum oscillations is the Bohr-Sommerfeld quantization condition for periodic quantum states. It can be written for canonically conjugate operators **p** and **r** as

$$\oint \mathbf{p} d\mathbf{r} = \left(n + \frac{1}{2}\right) 2\pi\hbar, \tag{3.3}$$

where **p** is the canonical momentum, **r** is the position operator in the plane perpendicular to **B**, and n is an orbital quantum number. Equation (3.3) can be modified in such a way as to quantize the magnetic flux Φ through the area $A(\mathbf{r})$ contained within the real-space orbit

$$\Phi = BA(\mathbf{r}) = \left(n + \frac{1}{2}\right) \frac{2\pi\hbar}{e}. \tag{3.4}$$

Taking into account a scaling factor between the real and the momentum spaces Eq. (3.4) can be rewritten in terms of the quantized area in **k**-space

$$A_{\mathbf{k}}(\varepsilon_n, k_z) = \left(n + \frac{1}{2}\right) \frac{2\pi eB}{\hbar}, \tag{3.5}$$

where $A_{\mathbf{k}}(\varepsilon_n, k_z)$ is the area enclosed by the intersection of the Fermi surface with a plane normal to the magnetic field.

It shows that in a magnetic field due to the quantized periodic motion of the charge carriers the allowed electronic states are condensed in **k**-space on a series of Landau tubes [Fig. 3.1]. These tubes have the form of straight coaxial cylinders with energies ε_n. The degeneracy of each cylinder is such that it is able to contain as many electronic states as lie within the annular cross-sectional area, ΔA, between two neighboring cylinders at zero field.

With increasing magnetic field, the tubes grow that leads to an increase of the degeneracy of each Landau level ε_n and a change of the free energy of the whole system. When a Landau cylinder crosses the boundary of the extremal Fermi-surface cross-sectional area, A_{F}, normal to the magnetic field, the free energy has a maximum. The further rise of B shrinks the Landau tube and, consequently, decreases the free energy. The next Landau cylinder with quantum number $(n-1)$ then start to be the outermost non-empty cylinder and will increase the free energy until $A_{\mathbf{k}} = A_{\mathrm{F}}$ and a new maximum at the free energy is reached. This periodic oscillatory behavior of the free energy is the nature of the magnetic quantum oscillations. The difference between the fields at which two neighboring Landau tubes cross the boundary of the extremal Fermi-surface cross section is given by

$$\frac{1}{B_n} - \frac{1}{B_{n-1}} = \Delta\frac{1}{B} = \frac{2\pi e}{\hbar}\frac{1}{A_{\mathrm{F}}}, \tag{3.6}$$

so that

$$F = \left(\Delta\frac{1}{B}\right)^{-1} = \frac{\hbar A_{\mathrm{F}}}{2\pi e}. \tag{3.7}$$

This result is known as the Onsager relation [77], which describes the relation between the periodicity of the oscillating free energy, its frequency, F, and the extremal cross-sectional area of the Fermi surface, A_{F}.

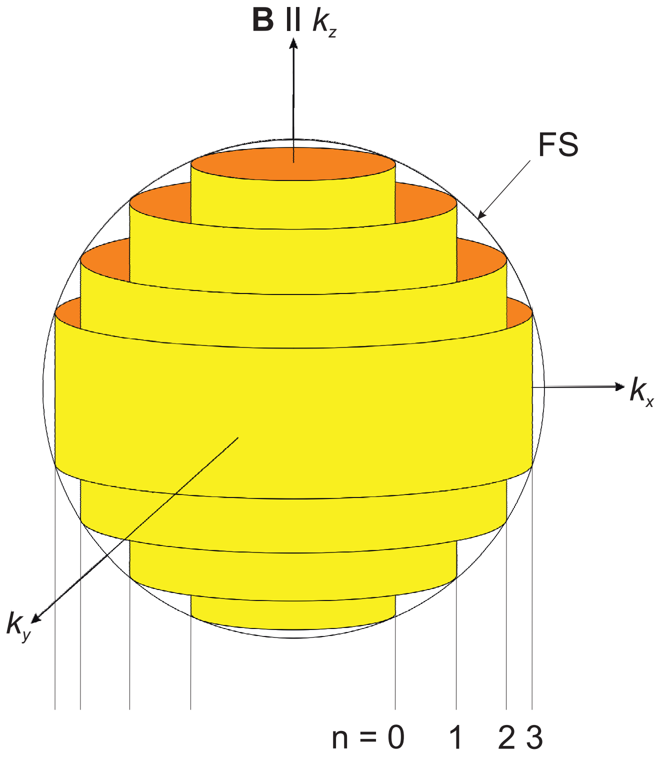

Figure 3.1.: *Schematic representation of the Fermi surface for a free-electron metal. Allowed electron states are condence in the plane perpendicular to the applied magnetic field direction on a series of constant energy surfaces in* **k***-space, known as Landau tubes.*

3.2. Lifshitz-Kosevich formula

The oscillations in the free energy can be determined by measuring many different physical properties such as the resistivity, specific heat, sound attenuation, the magnetization or torque. Since the oscillatory effects are described by similar formulas, this discussion will consider only the oscillatory magnetization.

The discovery of quantum oscillations of the magnetization in a magnetic field by W.J. de Haas and P.M. van Alphen, named after their authors de Haas-van Alphen (dHvA) effect [81], dates back to the year 1930. Independently in the same year Landau had predicted an oscillatory behavior of the magnetization of a metal in a varying magnetic field due to the orbital quantization of the electron motion [82]. However, only after five years the relevance of the theoretical prediction to the experimental observation had been related to each other. Moreover, the importance of this effect as a powerful tool for Fermi surface investigations was not realized before 1950 when Lifshitz [83] and Onsager [77] pointed out that quantum oscillations frequency of the dHvA effect is directly proportional to the extremal cross-sectional area of the Fermi surface. Finally, in 1956 a detailed analytical quantitative theory of quantum oscillations phenomena was established in the work of Lifshitz and Kosevich [84].

As a main result of this elegant theory the Lifshitz-Kosevich formula was derived that well describes the oscillatory part of the magnetization, $\widetilde{M}(B)$, of a sample in a varying magnetic field. The formula was deduced by calculating the gradient of the thermodynamic potential, Ω, with respect to the magnetic field at constant chemical potential, μ,

$$\mathbf{M} = -(\nabla_{\mathrm{B}}\Omega)_{\mu}. \tag{3.8}$$

For a fermionic system, using the Fermi-Dirac statistics and having states of energy ε, the thermodynamic potential can be calculated by a summation over all possible energy states

$$\Omega = -k_{\mathrm{B}}T \sum_{\varepsilon} \ln\left[1 + \exp\left(\frac{\mu - \varepsilon}{k_{\mathrm{B}}T}\right)\right]. \tag{3.9}$$

Further integration over k_z effectively counts in the formula the contribution of the different extremal cross sections of the Fermi surface. The final Lifshitz-Kosevich formula for the components of the oscillatory part of the magnetization parallel ($\widetilde{M}_{\|}$) and perpendicular ($\widetilde{M}_{\perp}$) to the magnetic field is the summation over all contributions

$$\widetilde{M}_{\|} = -\sqrt{\frac{e^5}{2\pi^5\hbar}} \frac{F\sqrt{B}}{m^*\sqrt{A''}} \sum_{p=1}^{\infty} \frac{R_T R_\mathrm{D} R_S}{p^{3/2}} \sin\left[2\pi p\left(\frac{F}{B}-\frac{1}{2}\right) \pm \frac{\pi}{4}\right], \tag{3.10}$$

$$\widetilde{M}_{\perp} = -\frac{1}{F}\frac{dF}{d\Theta}\widetilde{M}_{\|}. \tag{3.11}$$

where F is the de Haas-van Alphen frequency which is proportional to the extremal cross-section of the Fermi surface, p is the harmonic number, and R_T, R_D, and R_S are damping factors. A'' is the local curvature of the Fermi surface, m^* is the cyclotron effective mass which equals the band effective mass in the absence of many-body interactions (electron-electron, electron-phonon interaction, etc.), and $\pi/4$ is the phase shift which is positive for the minimal extremal cross-sections and negative for the maximal.

3.3. Damping factors in the Lifshitz-Kosevich formula

The influence of the temperature, scattering, and electron spin on the dHvA oscillations amplitude can be described by the damping factors R_T, R_D, and R_S. These factors can be considered independently from each other and thus make it possible to extract certain electronic properties characteristic for the studied compound. They can be extracted from the field-, temperature-, and angular dependence of the oscillation amplitude. The physical origin and the quantitative effect on the oscillation amplitude of these damping parameters are considered in more detail in what follows.

Effect of finite temperature R_T

The energy states which are occupied by electrons depend on the density of states (DOS) and on the Fermi-distribution function. The Fermi function, $f(\varepsilon)$, describes the probability that a given electron energy state will be occupied at a finite temperature. It has the following form

$$f(\varepsilon) = 1/(1 + e^{(\varepsilon-\mu)/k_{\mathrm{B}}T}). \tag{3.12}$$

At zero temperature, the Fermi function has the step-like behavior, but at the finite temperatures the distribution of the occupied states at the Fermi level $\varepsilon_{\mathrm{F}} = \mu\,(T = 0)$ is not sharp any more and becomes broadened over the energy range $k_{\mathrm{B}}T$. Hence, the emptying of the Landau tube which passes through the Fermi surface does not take place at a sharply defined field. This result is equivalent to a phase smearing and leads to a reduction of the oscillation amplitude by the factor

$$R_T = \frac{X}{\sinh X}, \tag{3.13}$$

with

$$X = \alpha m^* T/B, \tag{3.14}$$

and where

$$\alpha = \frac{2\pi^2 k_{\mathrm{B}}}{e\hbar} \approx 14.69\,T/K. \tag{3.15}$$

Using the reduction factor, R_T, introduced into the Lifshitz-Kosevich formula the effective cyclotron mass, m^*, of the electrons on the extremal orbit can be extracted by fitting the measured temperature dependence of the oscillations amplitude, where m^* acts as fitting parameter.

Dingle factor R_{D}

Crystal disorder, sample inhomogeneity, and thus impurity effects lead to suppression of amplitude of dHvA oscillations in a very similar way to described above the thermal damping factor. Impurity effect is temperature independent, and affects only the field dependence of the quantum oscillations. It can be explained by scattering of the conduction electrons on impurities after an average relaxation time, τ, which is inversely proportional to the mean free path, ℓ. The sharpness of the quantum level, ε_n, reduces according to the Heisenberg uncertainty principle, that leads to a broadening of the Landau tubes. This reduction function is called the Dingle factor, after its discoverer [85]. Shoenberg expresses the function as

$$R_{\mathrm{D}} = \exp\left(-\frac{\alpha m^* T_{\mathrm{D}}}{B}\right). \tag{3.16}$$

T_{D} is called the Dingle temperature which expressed as a temperature but relates to disorder and impurities as

$$T_{\mathrm{D}} = \frac{\hbar}{2\pi k_{\mathrm{B}}\tau}. \tag{3.17}$$

The scattering rate does not depend exclusively on the mean free path, but also on the size of the Fermi surface and the quasiparticle mass

$$\tau = \frac{\ell}{\langle v_{\mathrm{F}}\rangle} = \frac{m^*\ell}{\hbar\,\langle k_{\mathrm{F}}\rangle}, \tag{3.18}$$

where $\langle v_{\mathrm{F}}\rangle$ is the average Fermi velocity and $\langle k_{\mathrm{F}}\rangle$ correspond to the average momentum vector along the cyclotron orbit. The Fermi wave vector in this equation is an average relating to one cyclotron orbit.

Effect of Zeeman splitting R_S

In a magnetic field the spin degeneracy of each energy level ε is lifted by Zeeman splitting. This effect splits each Landau cylinder into two sets of levels according to the two spin orientations with respect to the magnetic field direction:

$$\varepsilon_{\uparrow} = \varepsilon - \frac{1}{2}g^*\mu_{\mathrm{B}}B, \tag{3.19}$$

$$\varepsilon_{\downarrow} = \varepsilon + \frac{1}{2}g^*\mu_{\mathrm{B}}B.$$

The energy gap which separates these levels is equal $\Delta\varepsilon = g^*\mu_{\mathrm{B}}B$, where $\mu_{\mathrm{B}} = e\hbar/2m_e$ is the Bohr magneton, and g^* is the electronic g-factor that is equal 2,0023 for free electrons, but it may be changed due to spin-orbit coupling. Thus for each Landau cylinder passing through the Fermi surface at increasing field there are two sets of levels giving rise to a phase difference, that leads to a reduction of the oscillations amplitude by the factor

$$R_S = \cos\left(\frac{\pi g^* m^*}{2m_e}\right). \tag{3.20}$$

3.4. Fermi-surface topology and beats in the Yamaji scenario

Since the frequency of quantum oscillations is proportional to the extremal cross-sectional area of the Fermi surface in a plane normal to the applied magnetic field, by rotating the sample it is possible to construct the full three dimensional Fermi-surface topology.

The Fermi surface of a three-dimensional metallic system consists of a sphere [Fig. 3.2(a)], the area of the extremal cross-section, A_{F}, is constant for any magnetic-field orientation. Therefore, the quantum oscillations frequency is also independent of the field angle

$$F(\Theta) = \text{const.} \tag{3.21}$$

The Fermi surface of a two-dimensional system consists of a cylinder [Fig. 3.2(b)], oriented along the k_z direction and connecting the top and bottom of the Brillouin zone. When the applied magnetic field is tilted by Θ from

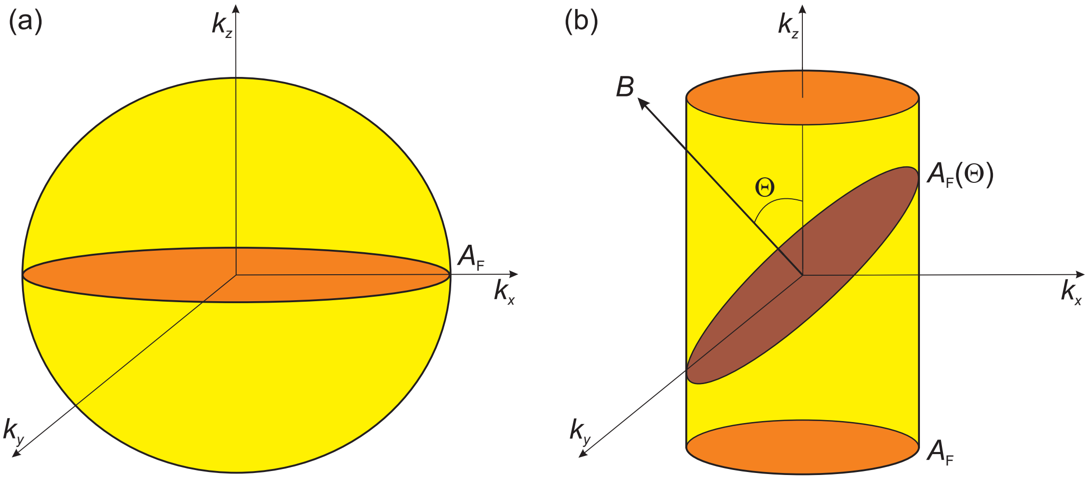

Figure 3.2.: *(a) Spherical Fermi surface of a three-dimensional metallic system. The cross-sectional area is constant. (b) Cylindrical Fermi surface of a two-dimensional material. The extremal cross-section changes as* $1/\cos\Theta$ *when the magnetic field is tilted off-axis.*

k_z towards k_x or k_y the extremal cross-sectional area of the Fermi surface increases as

$$A_{\mathrm{F}}(\Theta) = A_{\mathrm{F}} / \cos\Theta, \tag{3.22}$$

and the corresponding frequency also varies as

$$F(\Theta) = F / \cos\Theta. \tag{3.23}$$

In a more general scenario for a quasi-two-dimensional metal, the Fermi surface is composed of a weakly corrugated cylinder along the k_z axis. The deviation from the ideal cylindrical shape leads to the presence of two cross-sections with slightly different extremal orbits, which vary with field angle according to the Yamaji formula [86],

$$A_{\mathrm{F}}(k_z)\cos\Theta = \pi k_{\mathrm{F}}^2 \pm 4\pi m^* t\cos(ck_z) J_0(ck_{\mathrm{F}}\tan\Theta), \tag{3.24}$$

where k_{F} is the Fermi wave number for $t = 0$ related to A_{F} by equation $A_{\mathrm{F}} = \pi k_{\mathrm{F}}^2$, m^* is the effective mass, t is the interlayer transfer energy that parametrizes the warping, J_0 is the Bessel function zero-th order, and c is the lattice constant along the [001] direction.

In this case, there are two closely-spaced frequencies, the minimum, F_{min}, and the maximum, F_{max}, frequency which are given by

$$F_{min,max}(\Theta)\cos\Theta = (\hbar/2\pi e)\left[\pi k_{\mathrm{F}}^2 \pm 4\pi m^* t J_0\left(ck_{\mathrm{F}}\tan\Theta\right)\right], \tag{3.25}$$

where the first term is the average frequency $(\hbar/2\pi e)\,\pi k_{\mathrm{F}}^2 = (F_{min}^0 + F_{max}^0)/2$ and the second term $(\hbar/2\pi e)\,4\pi m^* t$ is $(F_{max}^0 - F_{min}^0)/2$ at $\Theta = 0°$.

These two frequencies produce very special beat patterns in the quantum oscillations, as is shown in Fig. 3.3. The beat pattern is strongly dependent on the angle Θ between the field and cylindrical axis. At $\Theta = 0°$ the beating is most rapid and becomes less rapid with rotation. At the Yamaji angle

$$\Theta_{\mathrm{Y}} = \arctan\frac{\xi_0}{ck_{\mathrm{F}}}, \tag{3.26}$$

when the Bessel function becomes zero (ξ_0 is the first zero), all the cross-sectional areas are equal [Fig. 3.3(c)]. Their contributions to the total magnetization interfere constructively to give the quantum oscillations signal without beats [87].

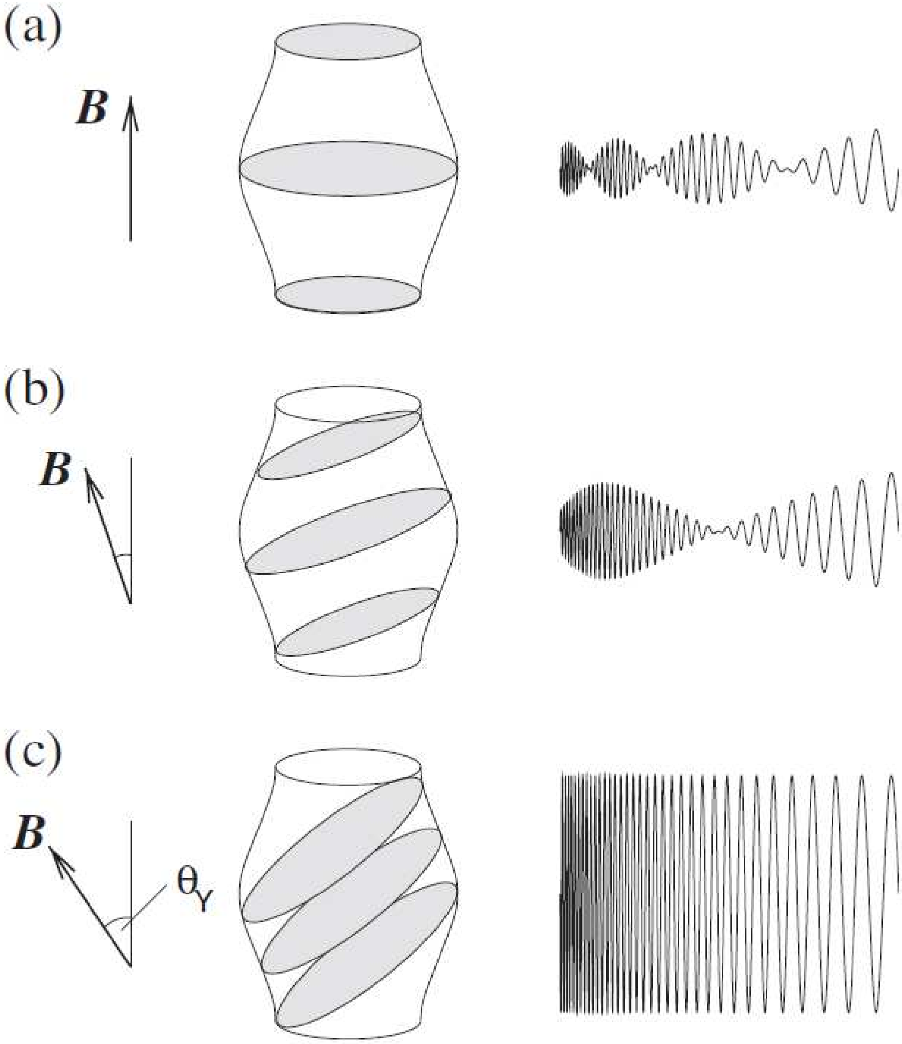

Figure 3.3.: *Schematic illustration of beat patterns in the Yamaji scenario [87]. For a simply corrugated cylindrical Fermi surface, the two different extremal orbits lead to a beat pattern in the quantum oscillations sketched on the right side of (a) and (b). The difference between the maximum and minimum cross-sections gradually changes when the magnetic field is tilted off-axis, until in (c) all Fermi surface cross sections become roughly equal at the Yamaji angle, Θ_Y. For this field direction, the oscillatory contributions from different slices of the Fermi surface all interfere constructively to give a maximum amplitude oscillating signal without beats. Beyond the Yamaji angle, the beats appear again until the second Yamaji angle is reached.*

4. Experiment

The first part of this chapter describes the essential conditions required for the successful experimental observation of such often very subtle quantum phenomena as the de Haas-vann Alphen effect. The installations that were used to reach these conditions, available at the Hochfeld-Magnetlabor Dresden and at the Laboratoire National des Champs Magnétiques Intenses Grenoble, are reviewed as well. The second part of the present chapter contains the general principle of a capacitive cantilever-torque magnetometry that was utilized for all dHvA studies considered in this thesis.

4.1. Experimental conditions

In order to observe quantum oscillations experimentally two very important conditions are necessary to realize:

- The electron wave packet has to complete at least once its orbit during the relaxation time before it is scattered: $\omega_c\tau > 2\pi$.

Taking into account that the cyclotron frequency, ω_c, is given by

$$\omega_c = \frac{eB}{m^*}, \tag{4.1}$$

this condition can be modified as

$$\tau > \frac{2\pi m^*}{eB}. \tag{4.2}$$

This implies that not only is the use of pure high-quality single crystals with small scattering rates important, but also the application of high magnetic fields are required in order to observe dHvA oscillations.

- The characteristic energy separating two neighbouring Landau tubes must be much more than the thermal energy: $\hbar\omega_c \gg k_\mathrm{B}T$.

Using Eq. (4.1), this condition can be defined by

$$\frac{B}{T} \gg \frac{m^* k_\mathrm{B}}{\hbar e}. \tag{4.3}$$

From this equation, it is obvious that high magnetic fields and low temperatures are crucial conditions to observe quantum oscillations. Moreover, in the case of heavy quasiparticles with strongly renormalized effective masses the large ratio B/T is prerequisite.

In order to satisfy both these conditions, all dHvA measurements presented in this thesis have been carried out on high-quality single crystals in high magnetic field facilities: at the Hochfeld-Magnetlabor Dresden (HLD) and at the Laboratoire National des Champs Magnétiques Intenses (LNCMI) Grenoble.

In the experiments performed at the HLD each measured sample was immersed either in the ^{3}He of a ^{3}He cryostat or in the ^{3}He/^{4}He mixture of a top-loading dilution refrigerator. The measurements in a ^{3}He cryostat were done up to 13 T at temperatures down to 0.4 K. Further measurements were made using a top-loading dilution refrigerator inside a 20-T superconducting magnet in the temperature range between 20 mK and 1.2 K. Additional high-field low-temperature dHvA investigations were realized at the LNCMI-Grenoble using a dilution refrigerator equipped with a 35-T resistive magnet.

For the temperature-dependent measurements of the dHvA signals the dilution refrigerators and ^{3}He cryostat together were able to cover the temperature range from 20 mK up to about 6 K. The sample temperature was measured using calibrated ruthenium-dioxide resistance thermometers.

The angular-resolved measurements have been carried out using a low-temperature rotation stage. Data were recorded as a function of angle with respect to the direction of the applied magnetic field over a large angular range around principle crystallographic directions.

4.2. Cantilever-torque magnetometry

The experimental dHvA data presented in this thesis have been obtained using a capacitive cantilever-torque magnetometry [88]. The magnetometer used in these measurements, as schematically shown in Fig. 4.1, consists of two rectangular plates that act as a capacitor. The upper plate is a Cu-Be flexible cantilever to which a sample is attached by a small amount of vacuum grease or Apiezone N and the lower plate is a fixed Cu ground plate. The high flexibility of the cantilever is achieved by means of two delicate cantilever beams (≈ 0.4 mm wide and ≈ 3 mm long) serving as a spring. The dimensions of the cantilever plates used in experiments are about 3×5 mm, with thickness varying between 20 and 100 μm. The thickness of the cantilever was chosen in such a way as to accommodate the background signal of the measured sample which was attached to the cantilever. The ground plate is separated from the cantilever by a thin distance plate of about 20 to 50 μm.

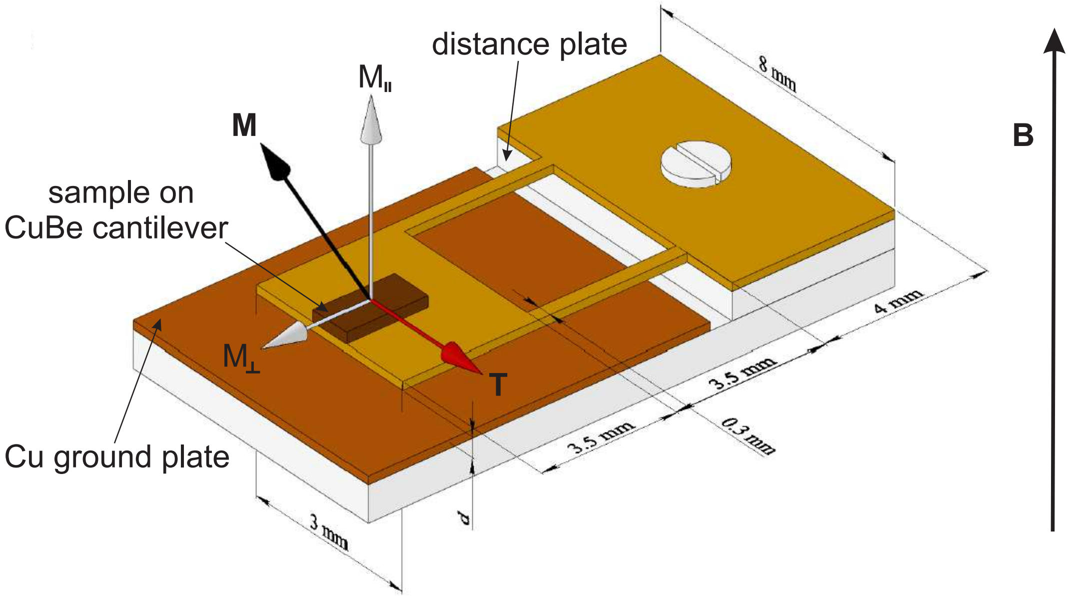

Figure 4.1.: *Schematic representation of a capacitive cantilever magnetometer. The principle of a measure is based on the torque caused by the anisotropic magnetization of a sample in a magnetic field.*

The general principle of a measurement in a cantilever magnetometry is based on the torque caused by the anisotropic magnetization of a sample in a magnetic field:

$$\mathbf{T} = \mathbf{M} \times \mathbf{B} V, \tag{4.4}$$

where **M** is the magnetization, **B** is the applied magnetic field, and V is the volume of a sample.

The torque acting on a sample bends flexible beams of a cantilever and changes slightly the distance d between the two plates of a capacitor. It causes a variation in the capacitance that for a small deflection of a cantilever is assumed to be proportional to the torque. Therefore, a measurement of the capacitance variation provide a measure of the torque. The total gap separation between the two plates of a capacitor is detected using a precision capacitance bridge Andeen Hagerling 2700A.

Since, the direction of the torque is always perpendicular to **M** and **B**, Eq. (4.4) can be described by

$$T = M_{\perp} B V, \tag{4.5}$$

where $M_{\perp}$ is the component of the magnetization perpendicular to the applied magnetic field.

Taking into account that for materials with an anisotropic Fermi surface, the oscillatory part of the magnetization, $\widetilde{M}$, has a component perpendicular to the magnetic field, given by Eq. (3.11) (see Chapter 3.2), the torque can be rewritten as follows:

$$T = -\frac{1}{F}\frac{\partial F}{\partial \Theta} \widetilde{M}_{\parallel} B V, \tag{4.6}$$

where $\widetilde{M}_{\parallel}$ is a oscillatory component of the magnetization parallel to the applied magnetic field ($\widetilde{M}_{\parallel}$ is defined by the Lifshitz-Kosevich formula Eq. (3.10)), F is the dHvA frequency and Θ is the orientation of the Fermi surface with respect to the applied filed. Therefore, it obvious that detection by the torque-cantilever technique requires an anisotropy of the Fermi surface. For orientations of the magnetic fields along the symmetry axis of the crystal, the torque will vanish since the anisotropy factor $(1/F)(\partial F/\partial \theta)$ becomes zero.

5. Yb-substituted $CeCoIn_5$

This chapter summarizes the results of systematic de Haas-van Alphen studies on different samples of Yb-substituted heavy-fermion superconductor $CeCoIn_5$ [89]. A series of $Ce_{1-x}Yb_xCoIn_5$ single crystals with varying Yb concentration have been carefully measured in magnetic fields up to 18 T using the already described capacitive cantilever-torque technique. For both end members $YbCoIn_5$ and $CeCoIn_5$, the angular-resolved dHvA frequencies can be very well described by conventional density-functional calculations.

5.1. Heavy-fermion superconductor $CeCoIn_5$

The interplay of partially filled $4f$ or $5f$ orbitals with conduction-band electrons is a key ingredient for the emergence of heavy-fermion behavior. The resulting Kondo resonances modify the electronic-excitation spectrum and the Fermi surface concomitant with heavy effective band-structure masses [90]. These correlated electrons may further lead to non-Fermi-liquid behavior and unconventional superconductivity often in conjunction with a quantum critical point, i.e., a zero-temperature phase transition tuned by some external control parameter such as pressure, magnetic field, or composition [91]. In this context, typical representatives are compounds containing the $4f$ rare earths Ce and Yb.

One example of such compounds is $CeCoIn_5$, an ambient-pressure superconductor with the highest superconducting transition temperature for Ce-based heavy-fermion compounds of $T_c = 2.3\,\mathrm{K}$ [92]. Specific-heat [93] and thermal-conductivity [94] measurements demonstrate power-law temperature dependences below T_c, pointing to an unconventional d-wave type of superconductivity [95] with line nodes in the energy gap. The nuclear quadrupole resonance (NQR) and nuclear magnetic resonance (NMR) measurements [96], Knight-shift data [97] and angle-dependent thermal-conductivity measurements [98] have identified that $\mathrm{CeCoIn_5}$ is a strong type-II superconductor. The upper critical field is anisotropic, varying between $B_{c2} = 4.95\,\mathrm{T}$ when the magnetic field is parallel to the c axis and $B_{c2} = 11.6\ \mathrm{T}$ when the field is applied in the basal (ab) plane.

5.1.1. Electronic structure

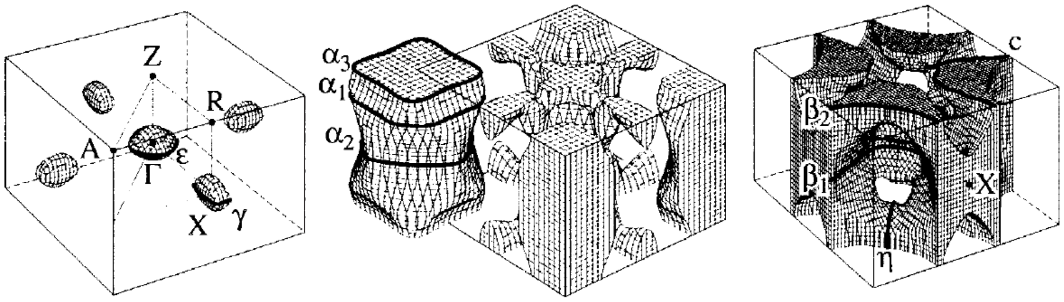

Figure 5.1.: *Fermi surface of $\mathrm{CeCoIn_5}$ is mostly composed of quasi-two-dimensional cylinders at the Brillouin zone corners and small three-dimensional ellipse at the zone center.*

The electronic properties of $\mathrm{CeCoIn_5}$ probed by de Haas-van Alphen measurements revealed a highly anisotropic nature of the Fermi surface mostly composed of quasi-two-dimensional nearly cylindrical and small three-dimensional ellipsoidal Fermi surfaces [99, 100]. Figure 5.1 shows the calculated Fermi surfaces of $\mathrm{CeCoIn_5}$ based on the itinerant $4f$ band model.

The large cyclotron effective masses up to about $100\,m_e$ for these Fermi surfaces are found to be field [100] and spin [101] dependent which is in agreement to what has been observed in other heavy-fermion systems [69].

5.1.2. Phase diagrams

At low temperatures when a magnetic field close to B_{c2} is applied in the basal plane, the phase transition from the normal to the superconducting state becomes first order [102] and a second superconducting phase appears

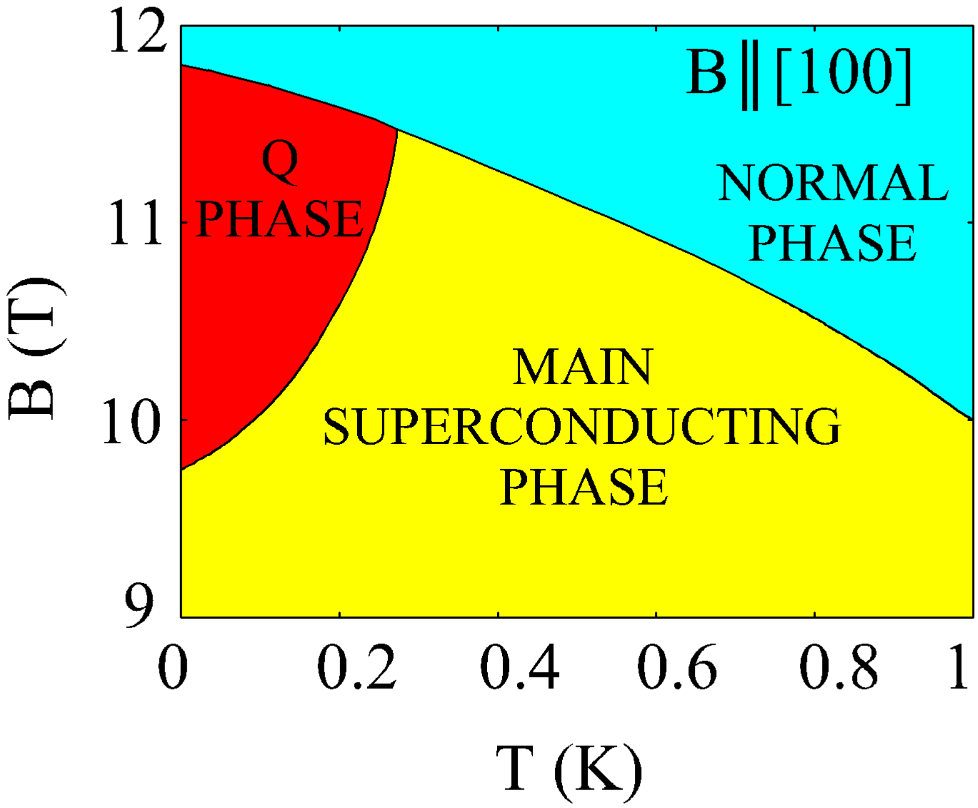

Figure 5.2.: *Schematic illustration of the low-temperature high-field part of the phase diagram of* $CeCoIn_5$ *for the field aligned along to the a axis [103].*

at high magnetic fields and low temperatures, as is shown in Fig. 5.2. With the help of the data from specific heat [56], magnetization [104], thermal conductivity [105], penetration-depth [106], NMR [107] and magnetostriction measurements [108] this second superconducting phase transition was declared as a possible realization of the inhomogeneous superconducting state, the so-called FFLLO state, proposed independently by Fulde and Ferrell [53] and Larkin and Ovchinnikov [54]. The FFLO phase is characterized by the presence of periodic regions of superconductivity separated by periodic regions of spin-polarized electron domains. In this state, the superconducting order parameter is spatially modulated and changes sign, either sinusoidally or more abruptly.

Indeed, CeCoIn$_5$ fulfills all required conditions for the presence of the FFLO state (see Chapter 2.3). It is a singlet Pauli-limited superconductor with a quasi-two-dimensional Fermi surface [99, 100] and an electron mean free path, (ℓ), which significantly exceeds the superconducting coherence length, (ξ_0) [94, 104]. Due to these facts, for many years, the high-field and low-temperature state of CeCoIn$_5$ was considered to be a first realization of a FFLO state. However, further NMR [109] results have found evidence for field-induced magnetism within this state and more recent neutron-scattering [103, 110, 111] and μSR [112] measurements revealed that in this phase antiferromagnetic order with a fixed magnetic wave vector appears which is in stark contrast to the expected FFLO state. This phase was named as a Q phase that is characterized by the simultaneous existence of superconducting and field-induced antiferromagnetic order. The antiferromagnetic order disappears sharply with increasing field as the superconductivity is destroyed at the upper critical field showing that superconductivity is necessarily for the magnetic order. This unusual and fascinating appearance of antiferromagnetism inside the superconducting phase has led to considerable theoretical and experimental efforts [113, 114].

As a unique feature CeCoIn$_5$ possess a further magnetic-field-driven antiferromagnetic quantum critical point near the upper critical field [115–118], as is shown in Fig. 5.3. Nature of the quantum critical point has been the subject of much speculations, but there are indeed indications that CeCoIn$_5$ is close to an antiferromagnetic QCP, situated just on the low-pressure side, i.e., negative pressure is needed to reach it [119].

In spite of the fact that long-range magnetic order is not present in CeCoIn$_5$ [120], the vicinity of this system to antiferromagnetic order [96] results in pronounced spin fluctuations which cause deviations from the standard Landau-Fermi-liquid theory. The non-Fermi-liquid behavior in CeCoIn$_5$ manifests itself in a number of ways: these include a logarithmic increase of the electronic specific-heat coefficient [121], enhanced and strong field dependence effective masses [100], and magnetic susceptibility that does not saturate at low temperatures [93].

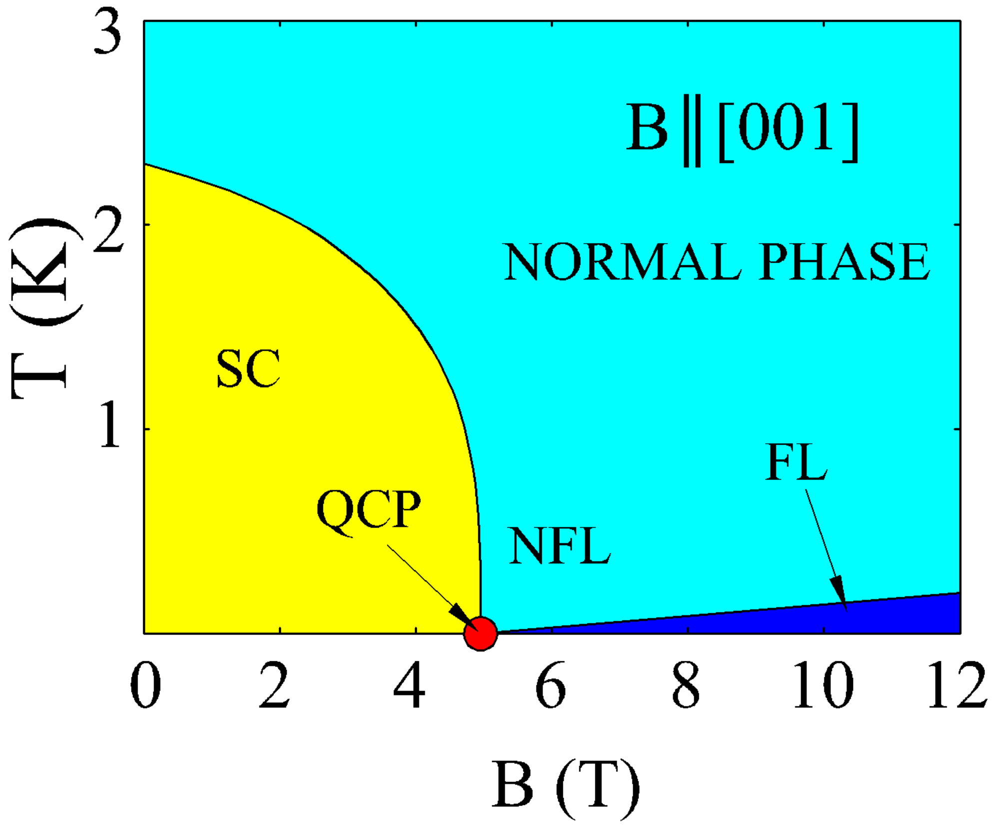

Figure 5.3.: *Schematic illustration of the phase diagram of CeCoIn$_5$ for the field aligned along to the c direction [115].*

5.1.3. Quantum critical point investigation

In order to clarify the question whether the quantum critical point is the direct result of the destruction of superconductivity, or only accidentally coincident with the upper critical field in CeCoIn$_5$, a series of experimental investigations has been performed. By applying an external control parameter such as magnetic field, hydrostatic pressure, or chemical substitution one can tune upper critical field and systematically investigate the evolution of the quantum critical behavior. In fact, tuning should either reveal antiferromagnetism or drive the system towards Fermi-liquid behavior.

Applying the magnetic field in the *ab* plane as well as along the *c* axis in CeCoIn$_5$ did not lead to evidence of an additional ordered phase, or to a Fermi-liquid behavior at the superconducting upper critical field [122]. On the other hand the pressure study revealed that the quantum critical point moves inside the superconducting dome to lower fields with increasing pressure [123]. This points to the fact that the superconductivity is not directly responsible for the non-Fermi-Liquid behavior in CeCoIn$_5$; instead, the data support an antiferromagnetic quantum critical point scenario.

Since the stoichiometry in CeCoIn$_5$ is stable and sizeable high-quality single crystals can be grown, besides pressure and magnetic field tuning, substitutional changes on the different lattice sites have also served as useful tuning parameters for the study of the quantum critical behavior [95,124–130].

Substitution on the In site in CeCoIn$_5$ via Cd has opened the possibility of tuning the ground state from superconductivity to antiferromagnetism [131]. Such quantum phase transitions are the subject of intensive investigations, both theoretically and experimentally [132]. Local-structure investigations have found that Sn, Cd, and Hg substitute preferentially for In within the Ce-In plane [133, 134], helping to explain their strong pair-breaking effect on superconductivity [131, 135]. An analysis of the entropy change between the normal and superconducting state combined with nuclear quadrupolar resonance measurements of Cd-doped CeCoIn$_5$ seems to indicate that superconductivity is destroyed locally around the dopant center [130] and that the two ground states coexist microscopically [136] for substitutions on both the indium site as well as the rare earth. Moreover, the substitution on the rare-earth site by magnetic and nonmagnetic substituents have been found to influence the Kondo-lattice coherence and Cooper pairing in a rapid and uniform way [124]. Yb substitution, however, shows a different behavior compare to other rare earth and lanthanide elements [95, 128, 129].

5.2. Ce$_{1-x}$Yb$_x$CoIn$_5$

In contrast to other heavy-fermion compounds [137], for Yb-substituted CeCoIn$_5$ the superconducting-transition temperature and the Kondo-coherence temperature do not scale and only weakly suppressed with Yb concentration [95]. It has also been reported that the non-Fermi-liquid behavior is strongly influenced by Yb atoms, and persists up to $x = 0.65$, after which a recovery of Fermi-liquid-like behavior is observed with increasing doping [129]. In its divalent state, Yb is expected to act as a non-magnetic dilution destroying the Kondo coherence and superconductivity. However, recent experiments, indicate [129] or have found evidence [128] for an intermediate valence of Yb in $\mathrm{Ce}_{1-x}\mathrm{Yb}_x\mathrm{CoIn}_5$ that might explain the observed features.

In order to better understand the electronic properties of $\mathrm{Ce}_{1-x}\mathrm{Yb}_x\mathrm{CoIn}_5$, in the course of this thesis a detailed study of the Fermi surface and effective-mass evolution as a function of Yb concentration have been investigated by de Haas-van Alphen measurements.

5.2.1. Crystal structure

A series of high-quality $\mathrm{Ce}_{1-x}\mathrm{Yb}_x\mathrm{CoIn}_5$ single crystals, that form in the HoCoGa_5-type structure by alternation of $\mathrm{Ce}_{1-x}\mathrm{Yb}_x\mathrm{In}_3$ and CoIn_2 layers along the tetragonal c axis, was synthesized from an In flux by combining stoichiometric amounts of Ce, Co, and Yb with excess In in the group of Z. Fisk at the University of California, Irvine, USA. Details of the crystal growth and characterization are described in Ref. [95]. The crystal structure of $\mathrm{Ce}_{1-x}\mathrm{Yb}_x\mathrm{CoIn}_5$ is shown in Fig. 5.4 and the corresponding lattice parameters [138, 139] are listed in Table 5.1.

The lattice parameters were determined from Rietveld refinement of powder x-ray diffraction patterns, using Si standard. The effective concentrations were determined with energy dispersive x-ray spectroscopy

Table 5.1.: Lattice parameters of the end members CeCoIn_5 and YbCoIn_5.

Parameters	CeCoIn_5	YbCoIn_5
Space group	P4/mmm	P4/mmm
Lattice parameters, Å	$a = b = 4.62$	$a = b = 4.56$
	$c = 7.56$	$c = 7.43$
V, nm^3	0.1614	0.1545

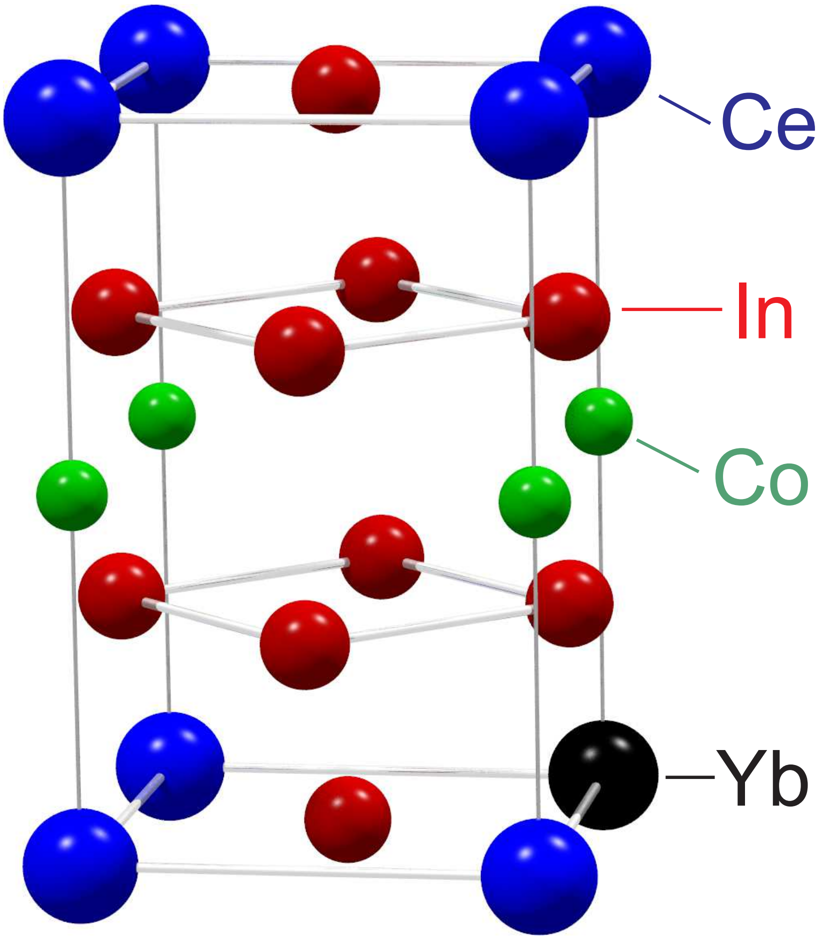

Figure 5.4.: *The crystal structure of Yb-substituted* $CeCoIn_5$.

(EDS) on the measured single crystals, as well as proton-induced x-ray emission microprobe (PIXE) on a mosaic of crystals from the same batch.

5.2.2. Magnetic and superconducting properties

The magnetic and superconducting properties of $Ce_{1-x}Yb_xCoIn_5$ have been measured in the group of Z. Fisk at the University of California, Irvine, USA by C. Capan et al. [95]. The magnetic susceptibility was studied using a vibrating-sample SQUID magnetometer in a fields of 1 T and higher applied perpendicular to the *c* axis. The heat capacity experiment was conducted

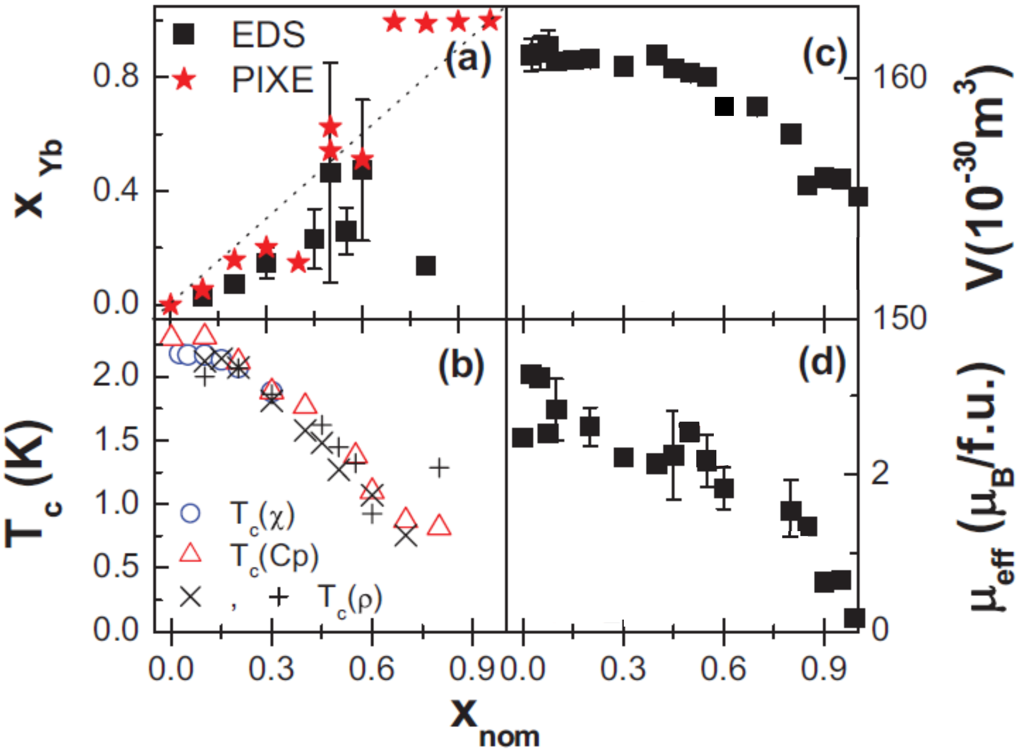

Figure 5.5.: *The doping evolution of characteristic parameters in $Ce_{1-x}Yb_xCoIn_5$ [95]. (a) Effective (x_{Yb}) versus nominal (x_{nom}) concentrations of Yb, as determined from EDS and PIXE. (b) Critical temperature T_c as a function of x_{nom}, as summarized from magnetic susceptibility (χ), specific heat (C_p), and resistivity (ρ). (c) Lattice volume versus x_{nom}, as obtained from powder X-ray diffraction. (d) Effective Curie-Weiss moment μ_{eff} (in units of Bohr magneton) as a function of x_{nom}, as determined from χ.*

using the standard adiabatic heat-pulse technique in a ^{3}He-PPMS. The resistivity (ρ) was measured using the standard four wire technique with an AC resistance bridge. Low resistance contacts were obtained by spot-welding Au wires.

The doping evolution of characteristic parameters in $Ce_{1-x}Yb_xCoIn_5$ is shown in Fig. 5.5. The effective Yb concentrations, as determined with either EDS or PIXE, are close to the nominal values for small x_{nom} but show large distribution around $x_{nom} = 0.5$, as indicated by the error bars in Fig. 5.5(a). Possible phase separation between pure $YbCoIn_5$ and $Ce_{1-x}Yb_xCoIn_5$ is likely the reason why one could not reach effectively $x_{nom} \geq 0.3$. In fact, for $x_{nom} \geq 0.7$, the batches yield essentially pure $YbCoIn_5$, with very few Yb-substituted $CeCoIn_5$ crystals. The difference between EDS and PIXE values reflects this difference between a single crystal and the average concentration of the mosaic of crystals. For simplicity, nominal concentrations will be used in the rest of this thesis. The lattice volume should decrease linearly with increasing Yb concentration according to Vegard's law. However, the lattice volume, as shown in Fig. 5.5(c), and the lattice parameters [129] remain nearly constant with x, indicating that Ce or Yb ions do not retain the valence of the end member compounds. Figure 5.5(d) shows the Curie-Weiss moment, obtained from linear fits to the inverse magnetic susceptibility. μ_{eff} (per formula unit) is suppressed below the Ce^{3+} moment (2.54 μ_B) with Yb substitution. This indicates that Yb substitutes as a non-magnetic ion. The absence of Curie-Weiss behavior in pure $YbCoIn_5$ and its small Sommerfeld coefficient shows that it is not a heavy-fermion compound [95].

5.3. Experimental details

As a main result of this thesis the torque, caused by the anisotropic magnetization, as a function of magnetic field, field angle, and temperature for samples with nominal Yb concentrations of $x = 0$, 0.1, 0.2, 0.3, 0.5, 0.55, 0.85, 0.95, and 1 have been carefully measured. For the measurements performed at the Hochfeld-Magnetlabor Dresden, capacitive cantilever torquemeters that could be rotated *insitu* around one axis have been utilized. The cantilevers were mounted either inside a ^{3}He cryostat equipped with a 15-T superconducting magnet or in the ^{3}He/^{4}He mixture of a toploading dilution refrigerator inside a 20-T superconducting magnet. In the course of this study, dHvA oscillations for the samples with $x = 0$, 0.1, 0.55, 0.85, 0.95, and 1 were resolved.

Further high-field torque measurements were performed in extension of this study at the Grenoble branch of the Laboratoire National des Champs Magnétiques Intenses. The samples with $x = 0.1$ and 0.2 were measured up to 35 T in a toploading dilution refrigerator equipped as well with a rotatable capacitive cantilever torquemeter. This extended field range and allowed to resolve magnetic quantum oscillations for $x = 0.2$ as well as additional dHvA frequencies for $x = 0.1$.

Band-structure calculations were done in the group of M. Côté at the Université de Montréal, Québec, Canada in the framework of density-functional theory (DFT) with a generalized gradient approximation for the exchange-correlation energy functional [140] using the ABINIT code in the projector augmented wave formalism [141]. The wave functions were expressed with a plane-wave basis up to an energy cutoff of 40 Ha (1088 eV). The Brillouin zone was sampled with a $16 \times 16 \times 16$ k-points grid. The crystal structures were fully relaxed. The calculated unit-cell parameters are found to be 1.1% and 1.5% smaller than experimental data in $YbCoIn_5$ and $CeCoIn_5$, respectively [139].

To obtain a more detailed description of the electronic structure in the Brillouin zone, maximally localized Wannier functions [142] were constructed which allowed to interpolate the Fermi surface on a very fine k-points grid and, hence, calculate the area of cross sections of the Fermi surface efficiently and precisely. Typically, a grid of 800×800 was used to determine the area of a Fermi surface. The interpolated k grid for the calculation of the cross-section area of the Fermi surface is refined up to an accuracy of 10^{-4} Å^{-2} which corresponds to 10 T on the dHvA frequency.

The occupation of the Yb-4f states was evaluated by M. Richter from the Leibniz-Institut für Festkörper- und Werkstoffforschung (IFW), Dresden, Germany with the full-potential local-orbital (FPLO) code [143, 144] version 9.01, using the same parametrization of the exchange-correlation functional as in the ABINIT calculations and experimental structure parameters [139]. The FPLO valence basis set comprised the following states: Yb-4f, 5s, 5p, 5d, 5f, 6s, 6p, 6d, 7s; Co-3s, 3p, 3d, 4s, 4p, 4d, 5s; In-4s, 4p, 4d, 5s, 5p, 5d, 6s, 6p. A linear tetrahedron method with Blöchl corrections with a k mesh of $33 \times 33 \times 20$ points in the full Brillouin zone was used for the k-space integrations. Spin-orbit coupling was included by employing a full relativistic four-component mode.

5.4. Results and discussion

5.4.1. de Haas-van Alphen study of Ce$_{1-x}$Yb$_x$CoIn$_5$

The field-dependent magnetic torque has been measured for nine different Yb concentrations and quantum oscillations in the magnetization have been observed in seven of them.

The obtained torque signals as a function of magnetic field between 0 and 18 T for all Yb concentrations (except $x = 0.85$ for which data were taken only in the field range between 8.5 and 18 T) are shown in Fig. 5.6. The magnetic field was aligned along (or slightly off) the c axes. For the samples with $x \leq 0.55$, clear anomalies appear in the torque at the upper critical fields. As was found already earlier [95, 129], the superconducting transition temperature and the upper critical field are only weakly suppressed with x. This is in

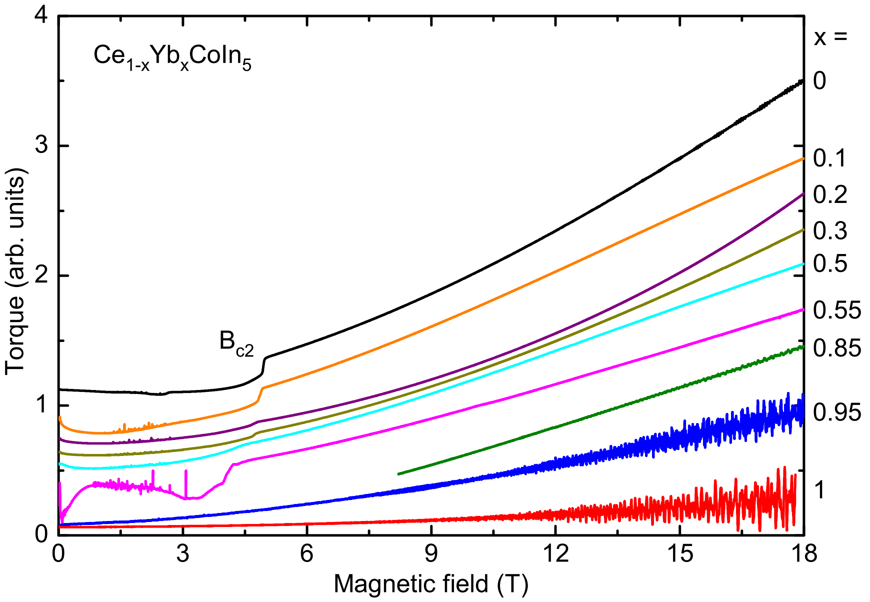

Figure 5.6.: *Magnetic-field dependence of the torque signals for* Ce$_{1-x}$Yb$_x$CoIn$_5$ *samples with various* x. *For Yb concentrations* $x \leq 0.55$ *the upper critical fields are clearly visible as step-like features. The magnetic field was aligned along the* c *axes (except for the sample with* $x = 0.55$ *where the field was tilted by* $\Theta_{010} = 2°$.

contradiction to other rare-earth substitutions of Ce in $CeCoIn_5$ [124]. For $x = 0.85$ and above, no signs of superconductivity are visible anymore.

In the normal state, the torque signals show approximately a B^2 dependence, that is expected for paramagnetic materials where $M \propto B$. On top of this raw data, oscillating dHvA signals can be resolved for the pure samples ($x = 0$ and 1) as well as for the samples with Yb concentrations of $x = 0.1$, 0.55, 0.85, and 0.95. This becomes clearer after background subtraction (using fourth-order polynomials) in Fig. 5.7. The oscillations were observable down to about 7 T depending on the orientation of the samples with respect to the field direction (except for $x = 0.1$ and 0.2 where oscillations were measured only down to about 15 T). The observation of dHvA signals proves the high quality of the samples.

The spectral richness of the oscillating signals can be realized in the Fourier spectra shown in Figs. 5.8 and 5.9. For the Fourier transformations over the high-field range between 15 and 18 T shown in Fig. 5.8, dHvA frequencies can be resolved for six concentrations.

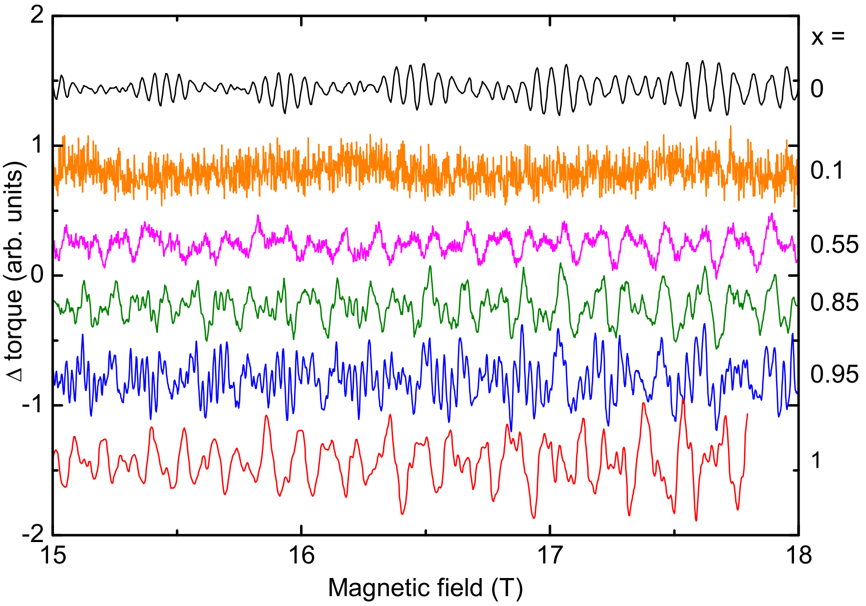

Figure 5.7.: *dHvA oscillations after subtracting smooth backgrounds from the raw data. The torque signals were measured at different temperatures between 25 and 75 mK.*

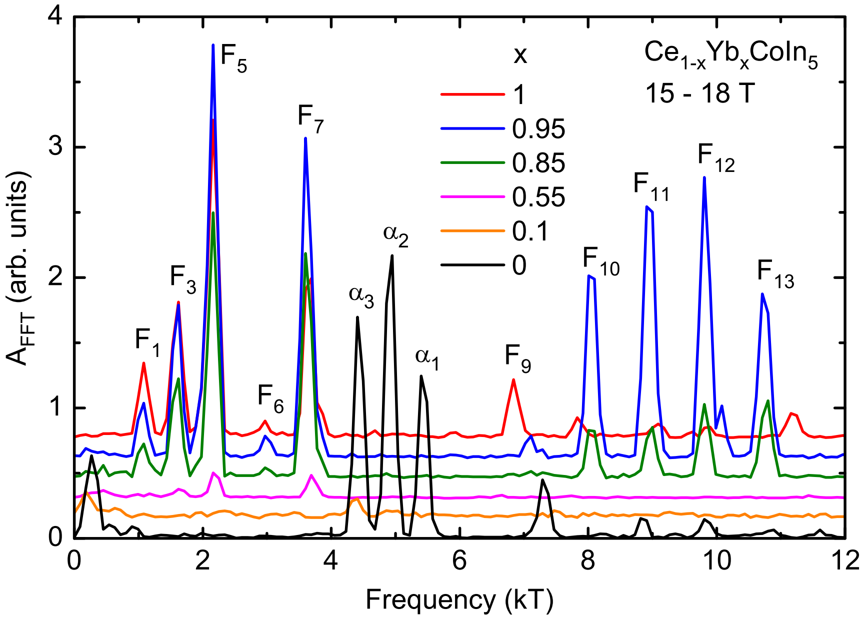

Figure 5.8.: *Fourier spectra of the background-subtracted torque data shown in Fig. 5.7 taken between 15 and 18 T.*

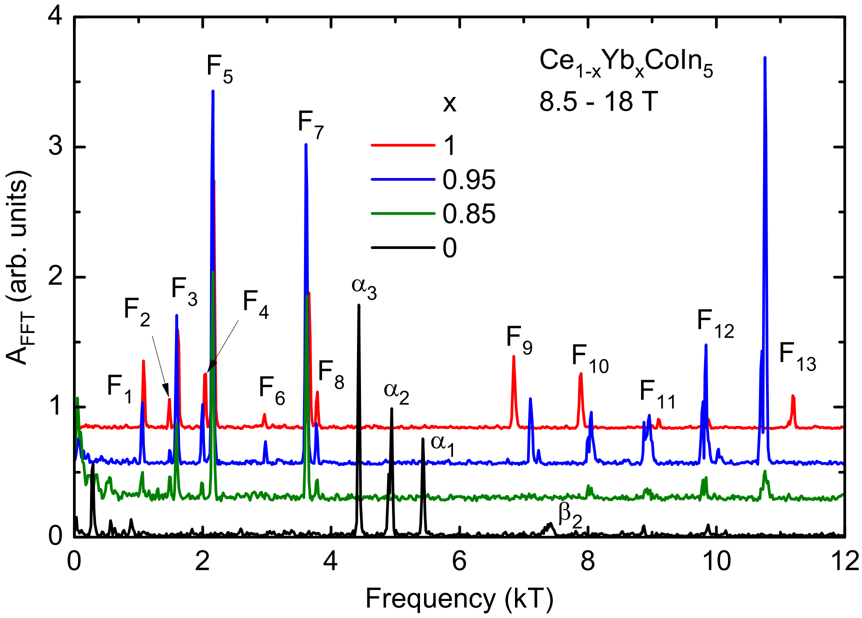

Figure 5.9.: *Fourier spectra of the background-subtracted torque data shown in Fig. 5.7 taken between 8.5 and 18 T.*

The compounds with x between 1 and 0.55 show a very similar spectral composition of their dHvA oscillations. However, for the materials with $x = 0.1$ and pure CeCoIn$_5$, the spectra are clearly different. This proves distinctly different Fermi-surface topologies for these two Yb-concentration ranges.

When extending the field range for the Fourier transformations down to 8.5 T, as is shown in Fig. 5.9, the increased spectral resolution allows to disentangle about thirteen fundamental dHvA frequencies for the Yb-rich concentrations [labeled F_1 to F_{13}] and about seven fundamental frequencies for CeCoIn$_5$. For the latter, the strongest spectral peaks are labeled α_1 to α_3 and β_1 to β_2 according to the assignment of earlier studies to which very good agreement both in the dHvA frequencies as well as in the heavy effective masses [100, 101] has been found.

In measurements up to 18 T performed at the HLD the dHvA signals for Ce$_{0.9}$Yb$_{0.1}$CoIn$_5$ [Figs. 5.7 and 5.8] could be just barely resolved and no oscillations were seen for the samples with Yb concentrations of $x = 0.2$, 0.3, and 0.5. For that reason the magnetic-field range was extended up to 35 T in a one-week experiment at the Laboratoire National des Champs Magnétiques Intenses. This made it possible to detect dHvA oscillations for the sample with $x = 0.2$ and a number of additional dHvA frequencies for $x = 0.1$.

The oscillating torque signals for these two samples for magnetic fields applied 6 and 5° off the c direction are shown in the insets of Figs. 5.10 and 5.11. The Fourier transformations [main panels of Figs. 5.10 and 5.11] allowed to disentangle at least six dHvA frequencies for each compound. The spectral distribution of these frequencies is, however, clearly different for the two concentrations. Whereas for $x = 0.1$ the spectrum is almost identical to that of the pure CeCoIn$_5$ sample, the dHvA spectrum for $x = 0.2$ has obviously changed. For the latter, the α orbits between 4 and 6 kT are absent and new orbits between 2 and 4 kT appear. They are labeled F_5 and F_7 in Fig. 5.11. On the other hand, the dHvA frequencies below 1 kT are only seen for Ce-rich samples. Consequently, for $x = 0.2$ the dHvA frequency spectrum reflects a mixture of CeCoIn$_5$ and YbCoIn$_5$ band structures.

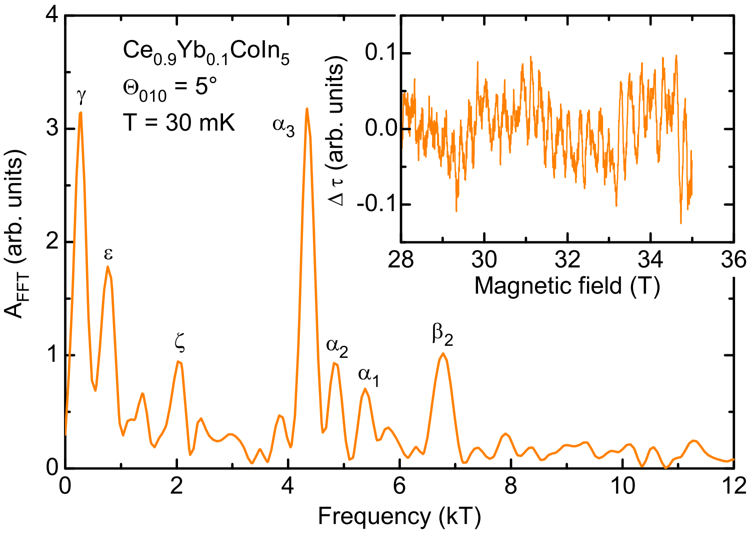

Figure 5.10.: *Fourier spectrum of the background-subtracted high-field torque signal shown in the inset for* $Ce_{0.9}Yb_{0.1}CoIn_5$*. Data were obtained at* 5° *off the c axis at temperature about 30 mK at the LNCMI-Grenoble.*

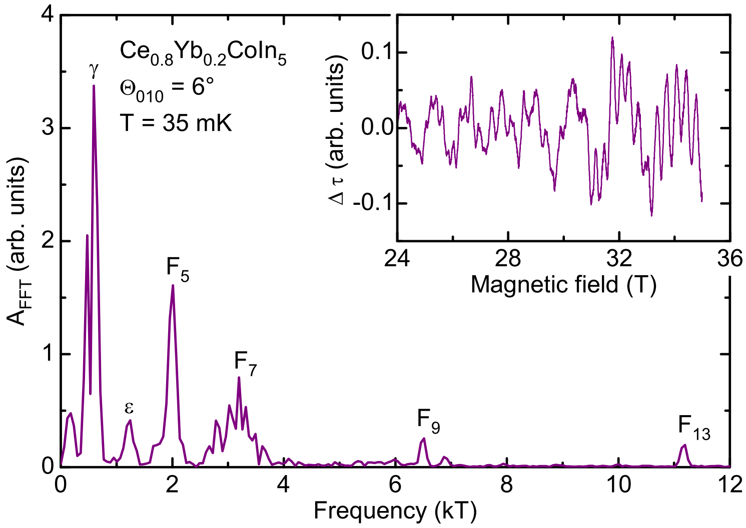

Figure 5.11.: *Quantum oscillations after background subtraction in* $Ce_{0.8}Yb_{0.2}CoIn_5$ *taken at the* $\Theta_{010} = 6°$ *at temperature of about 35 mK at the LNCMI-Grenoble are shown in the inset. The main panel contains the Fourier spectrum of these data.*

Rotating the samples, the angular dependences of the dHvA frequencies have been carefully measured. Figures 5.12, 5.13 and 5.14 show the evolution of the dHvA frequencies in $Ce_{1-x}Yb_xCoIn_5$ as the magnetic field is rotated from $B \parallel c$ axis ($\Theta = 0°$) towards $B \parallel a$ ($\Theta = 90°$) as a function of Yb substitution. The data for in-plane rotations around the c axis are only shown for $x = 1$. For the other concentrations very similar, almost angular independent dHvA frequencies were observed. For rotations from [001] to [110] the angular dependences of the dHvA signals are very similar to the Θ_{010} rotations (data not shown). From the angular dependences of the dHvA frequencies, some principal features of the Fermi-surface topologies have been extracted.

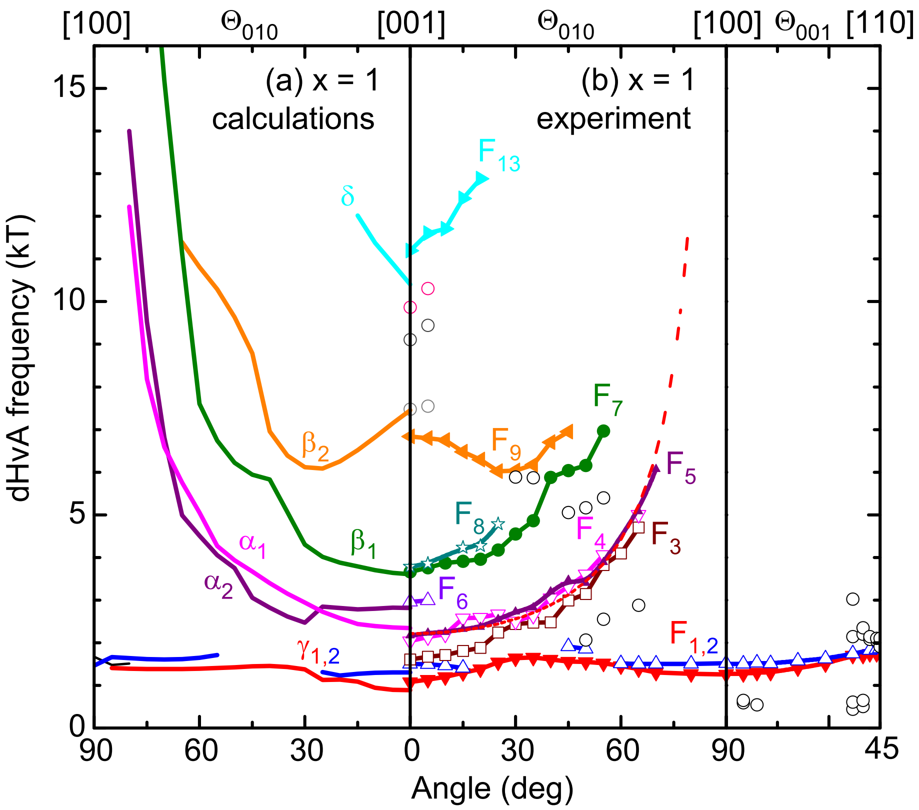

Figure 5.12.: *(a) Angular dependence of the predicted orbits from $B \parallel [001]$ ($\Theta = 0°$) to $B \parallel [100]$ ($\Theta = 90°$) for $x = 1$ ($YbCoIn_5$) and (b) angular dependence of the dHvA frequencies observed experimentally. The dashed line corresponds to $F(\Theta = 0) / \cos\Theta$ dependence.*

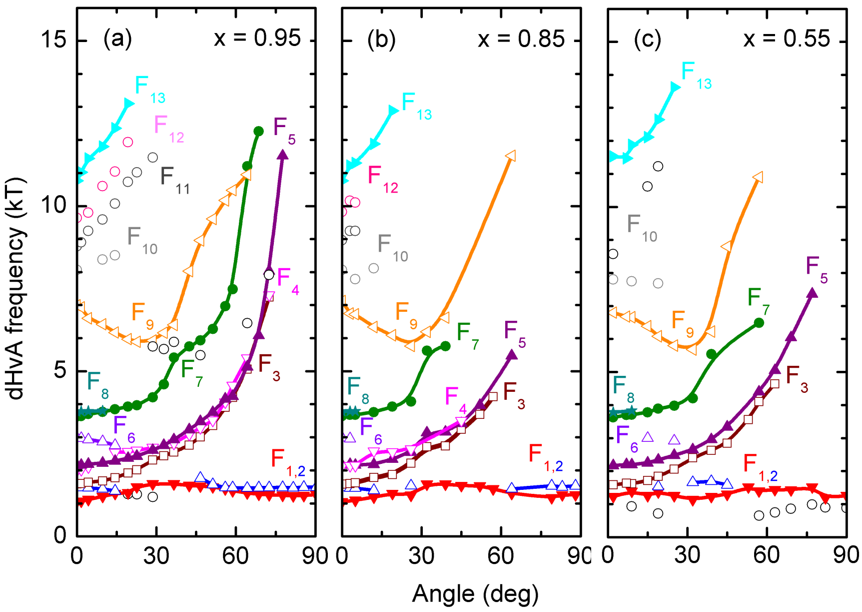

Figure 5.13.: *Angular dependences of the observed dHvA frequencies for the Yb-rich concentrations (a) $x = 0.95$, (b) $x = 0.85$, and (c) $x = 0.55$. The solid lines are guides to the eye.*

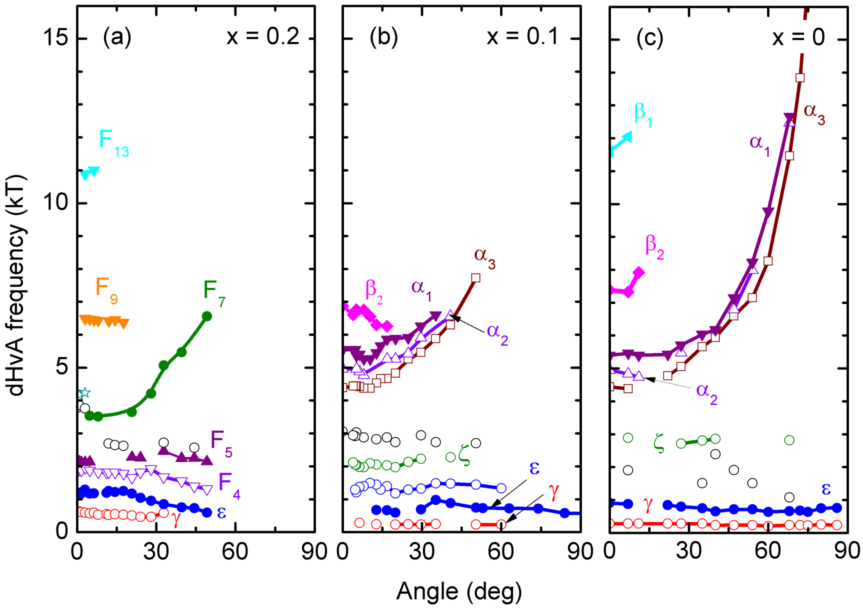

Figure 5.14.: *Angular dependences of the observed dHvA frequencies for the Ce-rich samples (a) $x = 0.2$, (b) $x = 0.1$, and (c) $x = 0$ (CeCoIn$_5$). The solid lines are guides to the eye.*

The observed angular changes can be categorized as follows. The low-frequency dHvA signals F_1 and F_2 in the Yb-rich samples are observable for almost all field orientations with nearly constant frequencies, i.e., for rotations around the b direction, Θ_{010}, as well as around the c axis, Θ_{001}. The same statement can be made for the ε and γ orbits in $CeCoIn_5$ and in the samples with $x = 0.1$ and 0.2. This correlates with one strongly corrugated or two small closed three-dimensional Fermi surfaces. Other dHvA frequencies (F_3 to F_9) can be traced over an extended angular range and follow roughly a $1/\cos\Theta$ dependence, where Θ here is the angle with respect to the c axis. The red dashed line in Fig. 5.12(b) visualizes this dependence. Such kind of behavior (similar for α_1 to α_3 in $CeCoIn_5$ and $Ce_{0.9}Yb_{0.1}CoIn_5$) is evidence for quasi-two-dimensional Fermi-surface sheets. The other dHvA frequencies disappear quickly when rotating away from the c axis. Since the amplitudes of these dHvA signals are quite large, this indicates complicated, probably multi-connected Fermi-surface sheets.

With decreasing Yb concentration, only small changes of the dHvA frequencies in the samples with $x = 0.95$, 0.85, and 0.55, as shown in Fig. 5.13(a) - (c), have been observed. The low-frequency dHvA spectra remain almost unchanged, whereas the higher frequencies belonging to the β and multiconnected Fermi-surface sheets move slightly [Figs. 5.8 and 5.9]. The clear observation of these changes, especially of the different shifts of the low- and high-frequency dHvA spectra, reflects the true substitution of Yb by Ce and renders a phase separation in the samples unlikely.

A clearly different Fermi-surface topology is apparent for the Ce-rich samples with $x = 0.1$ and 0, shown in Fig. 5.14(b) and (c). There appear two low-frequency dHvA signals, γ and ε, that probably arise from two small ellipsoidal Fermi surfaces around the Γ and X points [Fig. 5.15(b)]. The α orbits showing a quasi-two-dimensional angular dependence can be explained by a corrugated cylindrical Fermi surface that has approximately twice the area compared to the α sheet in $YbCoIn_5$. The β_1 and β_2 frequencies can be assigned to orbits of a complicated multiconnected Fermi surface with strongly renormalized heavy masses [100]. The sample with $x = 0.2$ reveals dHvA frequencies composed of both kinds of Fermi-surface topologies, as is shown in Fig. 5.14(a).

The Fermi surfaces shown in Fig. 5.15 with some highlighted extremal orbits from *ab initio* density-functional theory calculations account for the measured dHvA signals in YbCoIn$_5$ and CeCoIn$_5$. The Fermi surface topology found for YbCoIn$_5$ is very similar to calculated topologies of other 115 compounds without $4f$ contributions to the band structure [145]. The calculated angular dependence of the corresponding dHvA frequencies are shown as the solid lines in Fig. 5.12(a). Obviously, the frequencies F_1 and F_2 originate from the orbits γ_1 and γ_2 of the closed, highly deformed Fermi-surface sheet centered around Γ. A corrugated cylindrical Fermi surface at the corner of the Brillouin zone gives rise to the frequencies F_3 to F_6. Two of the extremal orbits are sketched as α_1 and α_2 in Fig. 5.15(a). Another highly corrugated Fermi surface surrounding the former warped cylinder could be ascribed to the orbits β_1 and β_2, the frequencies F_7 [and probably as well the satellite F_8] and F_9. The final calculated multiconnected Fermi surface could be accounted for by the δ orbit for the dHvA frequency F_{13}. This Fermi surface may be responsible as well for some other experimentally observed dHvA frequencies. The complicated topology of this Fermi surface, however, leaves a definite assignment ambiguous.

Recent x-ray absorption spectroscopy experiments provided evidence for an intermediate-valence state of Yb$^{2.3}$ in YbCoIn$_5$ [128]. As known, Yb^2 corresponds to a closed $4f$ shell, whereas Yb^3 corresponds to a $4f^{13}$ configuration. In order to check the compatibility of this finding with the present data and calculations, the occupation of the Yb-$4f$ states, n_{4f}, has been evaluated by M. Richter at the IFW Dresden, Germany, using the full-potential local-orbital [143, 144]. The occupation number obtained in these calculations is 13.7. Thus, the occupation number found in the present ordinary density-functional calculations using the generalized gradient correction is in accordance with the previously measured intermediate valence state [128].

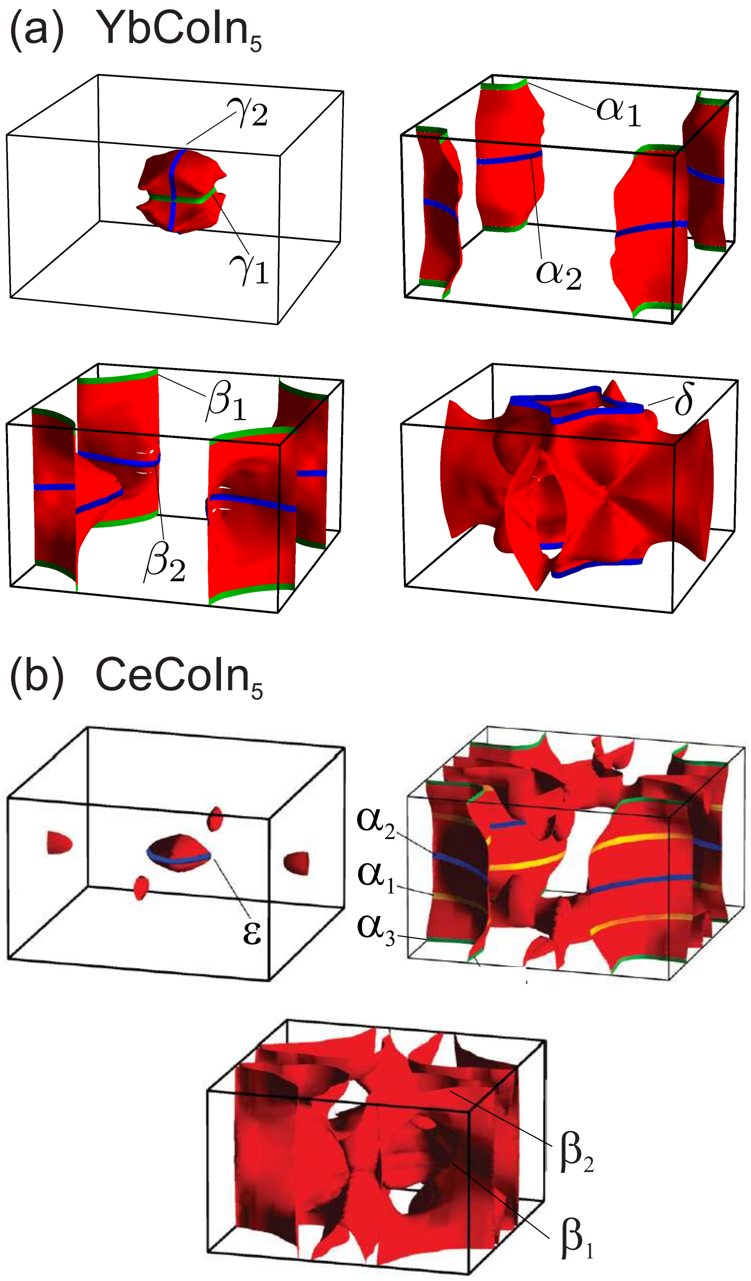

Figure 5.15.: *Fermi surfaces of the end members, (a) YbCoIn$_5$ and (b) CeCoIn$_5$ obtained from DFT calculations. The depicted orbits of extremal areas of the Fermi surface of YbCoIn$_5$ shown as blue and green lines correspond to the calculated dHvA frequencies in Fig. 5.12(a).*

5.4.2. Effective masses of Ce$_{1-x}$Yb$_x$CoIn$_5$

The effective cyclotron masses, m^*, have been extracted from the temperature dependences of the quantum oscillation amplitudes for different cyclotron orbits at various angles. For the determination of each effective mass a series of at least five measurements in the temperature ranges between 0.03 and 1.2 K when using dilution refrigerators have been realized. In addition, due to the observation of the small effective masses for the extreme orbits of the Yb-rich ($x \geq 0.55$) compounds, some effective masses have been obtained from data measured in the temperature range between 0.4 and 6 K in the ^{3}He cryostat. As an example Fig. 5.16 shows the analysis of the thermal evolution of the dHvA oscillations taken on YbCoIn$_5$ at $B \parallel [001]$ at ten different temperatures.

Figure 5.16(a) presents the raw data for several temperatures between 0.6 and 6 K. The corresponding background subtracted data taken over a field range 11 - 13 T are shown in the inset of Fig. 5.16(b). From this data set, Fourier transforms, shown in the main panel of Fig. 5.16(b), were carried out. Quantum oscillations amplitudes reduce with respect to the temperature. The obtained temperature-dependent amplitudes of the Fourier peaks are shown as symbols in Fig. 5.16(c). The red solid lines are fits according to the Lifshitz-Kosevich formula (see Chapter 3.2), yielding the noted effective masses in units of the free-electron mass.

For the Yb-rich samples, the effective masses for all observed bands in these materials are small [Table 5.2] and lie between 0.7 m_e and 2.6 m_e allowing to observe the dHvA signals up to high temperatures. This observation clearly shows that heavy-fermion physics is not an issue here.

For the Ce-rich samples, however, it is immediately evident from Fig. 5.18 that the dHvA signals diminish very quickly with temperature corresponding to large effective masses [Table 5.3] of roughly ten times the free-electron mass. This reflects the strong renormalization of the masses due to many-body interactions. It should be mentioned that a considerable field, spin, and angular dependence of the effective masses in CeCoIn$_5$ was found [100,101]. This reflects that Kondo physics is relevant and that possibly also quantum critical fluctuations play a role.

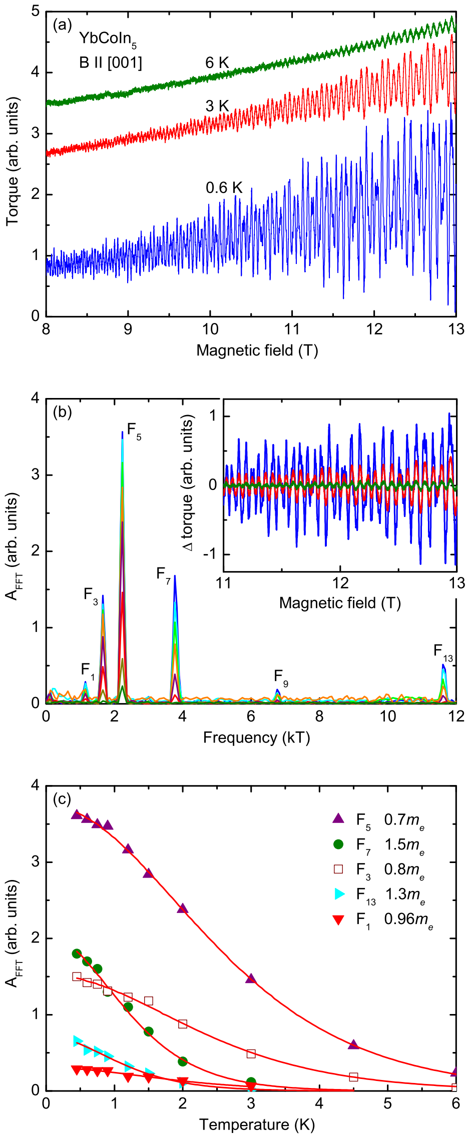

Figure 5.16.: *Temperature dependence of dHvA oscillations for YbCoIn$_5$ obtained with the magnetic field directed along the c axis at ten different temperatures from 0.6 to 6 K. (a) Raw torque signals shown for three different temperatures. (b) Inset: dHvA signals obtained by performing a background subtraction from (a). Main panel: Fourier transforms of the quantum oscillations shown in the inset performed over the field window between 11 and 13 T, at all measured temperatures. (c) Temperature-dependent oscillation amplitudes together with two parameter LK fits, in solid lines. The obtained results in the units of free electron masses are shown in the legend.*

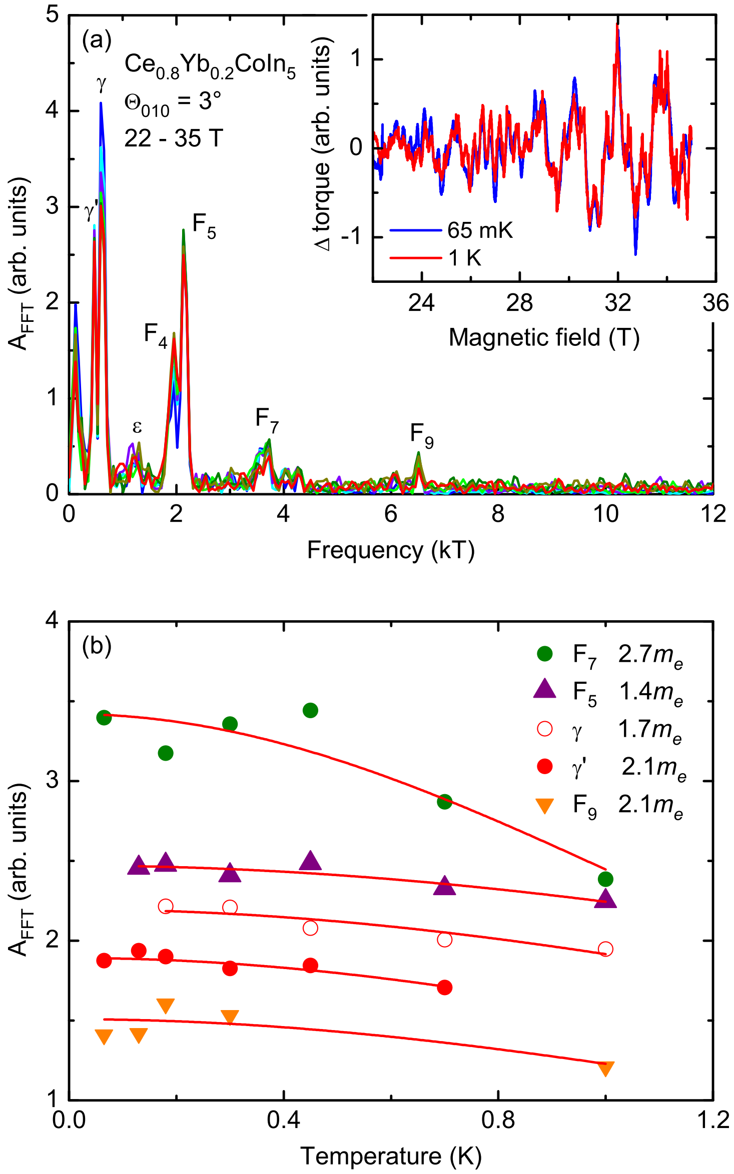

Figure 5.17.: *Temperature dependence of dHvA oscillations for $Ce_{0.8}Yb_{0.2}CoIn_5$ obtained with the magnetic field tilted 3° off the c axis at temperatures in the range from 0.065 to 1 K. (a) Inset: dHvA signals obtained on performing a background subtraction of raw torque data. Main panel: Fourier transforms of the oscillating torque signals shown in the inset performed over the field window between 22 and 35 T. (b) Temperature-dependent oscillation amplitudes together with two parameter LK fits, in red solid lines. The obtained results in the units of free electron masses are shown in the legend.*

For some dHvA frequencies due to their low amplitude in the Fourier spectrum and, hence, poor signal-to-noise ratio the determination of the corresponding effective masses were challenging. As one of such examples, Fig. 5.17 shows the temperature dependence of the dHvA frequencies for the sample with $x = 0.2$. For this Yb concentration as well as for Yb rich samples only relatively light effective masses in the range of $1.4\,m_e$ to $2.7\,m_e$ for the orbits observed at 27 T have been found. However, the limited temperature range below 1 K did not allow to determine the effective masses with high accuracy. Anyway, the very small amplitude reduction of the dHvA signal proves that all orbits in the sample with $x = 0.2$ have light effective masses.

Figure 5.18 accommodates the data collected for other concentrations of frequencies α (for $x = 0$, 0.1, and 0.2) and F_7 (for $x = 0.55$, 0,95 and 1) in $\mathrm{Ce}_{1-x}\mathrm{Yb}_x\mathrm{CoIn}_5$ together with the fit lines according to the Lifshitz-Kosevich theory and the corresponding effective masses.

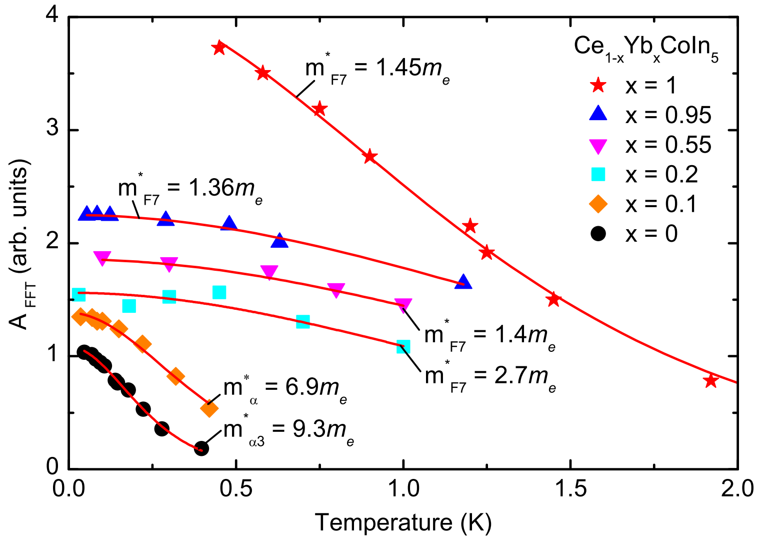

Figure 5.18.: *Temperature dependence of the dHvA amplitudes for selected orbits and Yb concentrations. The solid lines are fits using the Lifshitz-Kosevich formula yielding the noted effective masses in units of the free-electron mass. The data were obtained at the following angles, Θ_{010}, and average magnetic fields: at 0° and 11.9 T for $x = 1$; 0° and 15.8 T ($x = 0.95$); 15° and 16.4 T ($x = 0.55$); 3° and 27 T ($x = 0.2$); 5° and 31.7 T ($x = 0.1$); 7° and 12.9 T ($x = 0$).*

Table 5.2.: dHvA frequencies and effective masses for various extremal orbits in $Ce_{1-x}Yb_xCoIn_5$ with x between 1 and 0.55 for magnetic fields close to the [001] direction obtained from experiment. Effective masses are given in units of the free electron mass.

x	1		0.95		0.85		0.55	
$\bar{B}$ (T)	11.9		15.8		11.9		16.4	
Θ_{010}	0°		0°		6°		15°	
Frequency (orbit)	F_{exp} (kT)	m^*_{exp} (m_e)	F_{exp} (kT)	m^*_{exp} (m_e)	F_{exp} (kT)	m^*_{exp} (m_e)	F_{exp} (kT)	m^*_{exp} (m_e)
$F_1(\gamma_1)$	1.08	0.96	1.06	1.1	1.1	1.0	1.26	–
$F_2(\gamma_2)$	1.48	–	1.49	–	1.47	1.09	–	–
F_3	1.61	0.8	1.59	0.86	1.63	0.79	1.71	1.02
$F_4(\alpha_1)$	2.04	0.7	1.99	–	2.15	–	–	
$F_5(\alpha_2)$	2.17	0.7	2.15	0.76	2.16	0.75	2.25	0.65
F_6	2.96	–	2.96	2.4	–	–	–	–
$F_7(\beta_1)$	3.66	1.45	3.61	1.36	3.68	1.4	3.78	1.4
F_8	3.78	–	3.77	1.66	3.79	–	–	–
$F_9(\beta_2)$	6.84	1.2	7.0	1.42	6.73	–	6.39	1.97
F_{10}	7.48	–	8.05	1.57	7.79	–	7.8	–
F_{11}	9.11	–	8.92	1.51	9.25	–	10.62	–
F_{12}	9.87	–	9.84	1.41	10.11	–	–	–
$F_{13}(\delta)$	11.2	1.3	10.77	1.28	11.31	1.27	12.11	2.6

Table 5.3.: dHvA frequencies and effective masses for various extremal orbits in $Ce_{1-x}Yb_xCoIn_5$ with x between 0 and 0.2 for magnetic fields close to the [001] direction obtained from experiment. The effective masses of the parent compound $CeCoIn_5$ ($x = 0$) published in [100] are also given for comparison.

x	0 [100]		0		0.1		x	0.2	
$\bar{B}$ (T)	16		12.9		31.7		$\bar{B}$ (T)	27	
Θ_{010}	0°		7°		5°		Θ_{010}	3°	
Orbit	F_{exp} (kT)	m^*_{exp} (m_e)	F_{exp} (kT)	m^*_{exp} (m_e)	F_{exp} (kT)	m^*_{exp} (m_e)	Orbit	F_{exp} (kT)	m^*_{exp} (m_e)
γ	0.23	4.3	0.28	–	0.46	6.0	γ'	0.47	2.1
ε	0.67	12.0	0.91	–	0.82	–	γ	0.59	1.7
–	–	–	–	–	1.18	–	ε	1.3	2.3
–	–	–	–	–	1.41	4.0		1.48	–
–	–	–	–	–	2.0	3.0	F_4	1.96	–
–	–	–	–	–	3.05	9.1	F_5	2.13	1.4
α_3	4.24	8.4	4.37	9.3	4.35	6.9	F_7	3.73	2.7
α_2	4.53	18.0	4.87	11.4	4.82	8.6		4.09	–
α_1	5.56	15.0	5.46	14.5	5.43	9.0		4.32	–
β_2	7.5	49.0	7.39	52.4	6.73	28.2	F_9	6.52	2.1
β_1	12.0	48.0	12.0	53.2	–	–	F_{13}	10.83	–

From the density-functional-theory calculations, the effective masses for a magnetic field along the c direction have been derived. These are calculated using

$$m^* = \frac{\hbar^2}{2\pi}\left(\frac{\partial A_\mathrm{F}}{\partial \varepsilon_F}\right), \tag{5.1}$$

where A_F is the area of the Fermi surface cross-section.

For YbCoIn$_5$, the calculated masses are found to be near $1\,m_e$ as reported in Table 5.4. The experimental values are only slightly larger, most probably due to many-body interactions.

The band structure depicted in Fig. 5.19(a) shows that the Yb-4f density of states peaks at 0.5 eV below the Fermi energy. It is almost zero at the Fermi level where the most significant contribution is from Co-d orbitals. Including spin-orbit coupling does not change the band structure near the Fermi level despite the proximity of the f electrons.

As also evident in Table 5.4 in CeCoIn$_5$, the calculated frequencies are 5.6, 4.7, and 3.9 kT for the α_1, α_2, and α_3 orbits, respectively, for fields along

Table 5.4.: dHvA frequencies and effective masses for various extremal orbits in YbCoIn$_5$ and CeCoIn$_5$ for a magnetic field in the [001] direction from experiment and calculations.

		F (kT)		$\|m^*\|$ (m_e)	
Sample	Orbit	Exp.	Cal.	Exp.	Cal.
YbCoIn$_5$	γ_1	1.08	0.96	0.96	0.5
	γ_2	1.48	1.3	1.0	0.8
	α_1	2.04	2.3	0.7	0.5
	α_2	2.17	2.8	0.7	0.8
	β_1	3.66	3.6	1.5	1.0
	β_2	6.84	7.4	1.2	1.0
CeCoIn$_5$	α_1	5.46	5.6	14.5	1.5
	α_2	4.87	4.7	11.4	1.2
	α_3	4.37	3.9	9.3	1.3

the *c* direction. These values are in good agreement with the experimental data. Similar to $YbCoIn_5$, where spin-orbit coupling does not affect much the Fermi surface. The associated effective masses are much lower than the experimental data.

The partially filled Ce-f orbitals [Fig. 5.19(b)] are expected to be strongly correlated, therefore not correctly described by presented calculations. This explains the correct Fermi surface but lower effective masses. Adding a Hubbard term on localized orbitals such as it is done in DFT+U, is known to improve the agreement between theory and experimental data for compounds with f electrons [146]. More sophisticated approaches, such

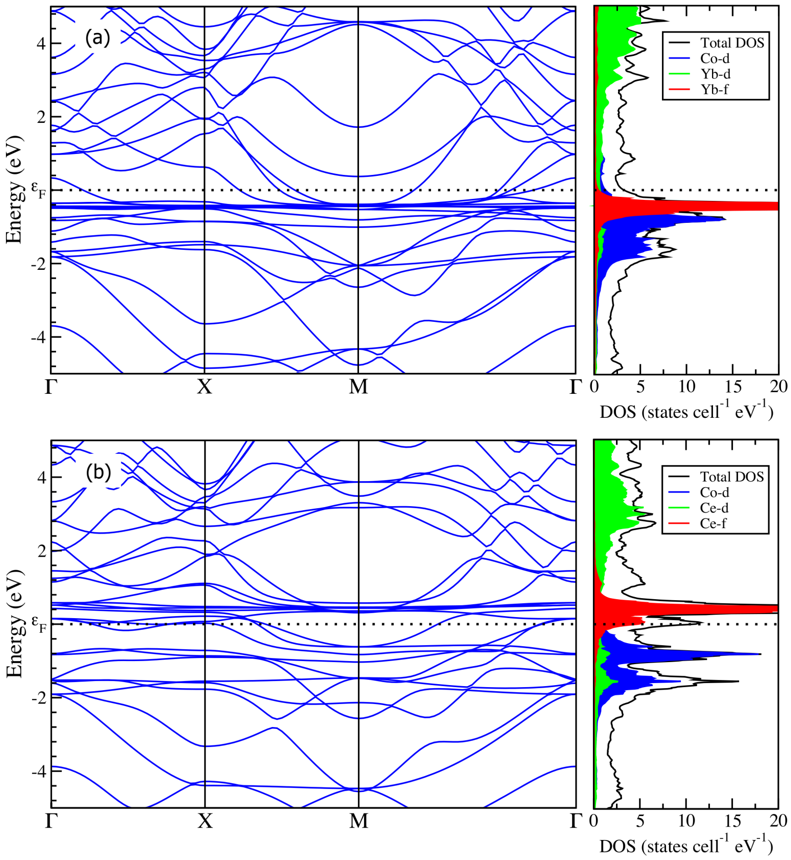

Figure 5.19.: *Band structure and density of states (DOS) for (a) $YbCoIn_5$ and (b) $CeCoIn_5$. Only the decomposed DOS for Yb(Ce)-f, Yb(Ce)-d, and Co-d are shown. Only the total DOS is correctly normalized.*

as DFT+DMFT (dynamical mean field theory), could also improve current results. It remains to be seen if such methods could improve the agreement of the effective masses for CeCoIn$_5$, but this falls outside of the scope of the present study.

The Yb-concentration dependence of the measured effective masses contradicts the specific-heat results reported in [95, 129] where up to $x = 0.55$ almost no change of the Sommerfeld coefficient and for higher concentrations up to $x = 0.8$ only a moderate reduction of the electronic specific heat is observed. This indicates that heavy itinerant quasiparticles still evolve up to such high Yb concentrations and that they even form the superconducting condensate. The latter is evidenced by the observed large anomalies in the specific heat at T_c [95, 129]. In the presented dHvA study, however, heavy quasiparticle for $x \geq 0.2$ have not been resolved. A possible reason for that might be a disorder-induced strong scattering making the observation of quantum oscillations in some presumably still existing heavy-electron $4f$ bands impossible. In order to check this statement the Dingle temperatures and the scattering rates in all samples subjected to dHvA investigation have been evaluated.

5.4.3. Scattering rates of Ce$_{1-x}$Yb$_x$CoIn$_5$

The Dingle temperatures that are directly proportional to the scattering rates of the studied samples have been estimated from the magnetic-field dependence of the dHvA signal amplitudes. According to the Lifshitz-Kosevich formula, the data plotted as $\ln[A_0 \sinh(\alpha m^* T/B) T^{-1}/\bar{B}^{-1/2}]$ versus $1/B$ should lie on a straight line, whose slope $a = -\alpha m^* T_\mathrm{D}$ yields the Dingle temperature $T_\mathrm{D} = \hbar/(2\pi k_\mathrm{B} \tau)$ and is a measure of the scattering rate τ^{-1} (see Chapter 3.2).

Figure 5.20 shows the field dependence of the dHvA oscillation amplitudes in Ce$_{1-x}$Yb$_x$CoIn$_5$. Fitting the data according to the Lifshitz-Kosevich formula gives the Dingle temperatures, shown in the legend, for different Yb concentrations. T_D increases from 0.3 K for CeCoIn$_5$, over 1.0 K for $x = 0.1$ to values of about 5.6 K for $x = 0.2$ and 3.8 K for $x = 0.55$.

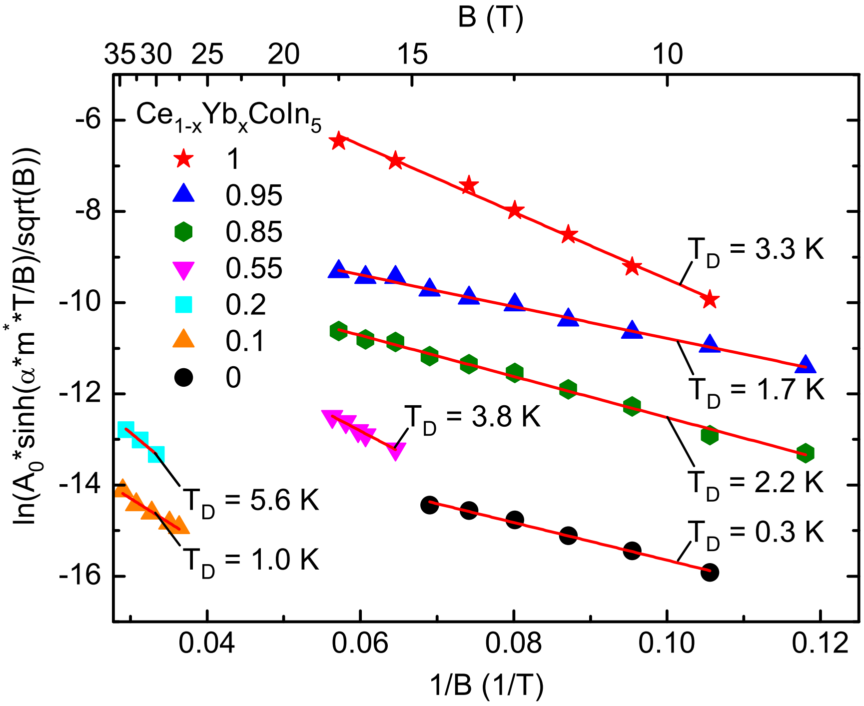

Figure 5.20.: *Dingle plot of* $Ce_{1-x}Yb_xCoIn_5$. *Symbols represent the experimental data. Solid lines are fits according to the Lifshitz-Kosevich formula.*

Since the Dingle temperatures and effective masses are known, the electronic mean free path, ℓ, and Fermi velocity for each particular orbit in $Ce_{1-x}Yb_xCoIn_5$ can easily be calculated. The mean free path is given by equation

$$\ell = v_F \tau, \tag{5.2}$$

where Fermi velocity is defined as

$$v_F = \frac{\hbar k_F}{m^*}. \tag{5.3}$$

Taking into account, that a circular extremal cross-sectional area of a cylindrical or spherical Fermi surface is expressed by

$$A_F = \pi k_F^2,$$

Eq. (5.2) could be rewritten as

$$\ell = \frac{\hbar^2}{2\pi k_B m^* T_D}\sqrt{\frac{2eF}{\hbar}}. \tag{5.4}$$

Table 5.5.: Dingle temperature, T_D, effective mass, m^*_{exp}, scattering rate, τ, mean free path, ℓ, and electron velocity v_F in $\mathrm{Ce}_{1-x}\mathrm{Yb}_x\mathrm{CoIn}_5$.

x	Orbit	m^* (m_e)	T_D (K)	τ (10^{-12} s)	ℓ (nm)	v_F ($10^5 \frac{m}{s}$)
0	α_3	9.3	0.3	4.1	185	0.46
0.1	α_3	6.9	1.0	1.2	73	0.6
0.2	γ	1.7	5.6	0.2	20	0.91
0.55	F_7	1.6	3.8	0.3	78	2.45
0.85	F_7	1.4	2.2	0.6	150	2.74
0.95	F_7	1.4	1.7	0.7	196	2.74
1	F_7	1.5	3.3	0.4	95	2.57

The Dingle temperatures, scattering rates, and Fermi velocities determined in this thesis with this procedure for samples with different Yb concentration are summarized in Table 5.5.

Assuming that the scattering rates are similar for all orbits within one sample, the observed high Dingle temperatures, would not allow for a detection of heavy-mass orbits (such as the β orbits in CeCoIn_5) for $x = 0.2$ and $x = 0.55$.

Anyway the persistence of the Kondo coherence with even high Yb dilution and the emergence of superconductivity out of presumed heavy-mass bands with strong disorder is highly unusual. Some first ideas on possible cluster formations of strongly correlated Yb impurities have been suggested in order to explain the robust Kondo state and the different evolution of the physical properties of Yb doping versus La doping in CeCoIn_5 [130, 147]. These seem to suggest that the Kondo holes around Yb dopants do not lead to strong additional scattering, which for example is the case for La doping [148]. Such an ansatz would allow to reconcile with the low effective masses and well-resolved dHvA signals in the Yb-rich materials proving their well-ordered crystalline structure.

5.5. Conclusions

In conclusion, the Fermi surface evolution with Yb substitution in $Ce_{1-x}Yb_xCoIn_5$ was systematically studied via the analysis of de Haas-van Alphen oscillations and the comparison to results of band-structure calculations done in the group of M. Côté. dHvA investigation presented in this thesis studied a transition from the heavy-fermion limit $CeCoIn_5$ to the mixed-valence limit in $YbCoIn_5$ with an Yb valence of +2.3. The valence of +2.3 resulting from full-potential local-orbital calculations is in agreement with previous experimental results of extended x-ray absorption fine structure (EXAFS) and x-ray absorption near-edge structure (XANES) measurements. The Fermi-surface topology change what was observed experimentally is consistent with what is expected from the band structure. For a small Yb concentration, $x = 0.1$, the band-structure topology and the effective masses remain nearly unchanged compared to $CeCoIn_5$. However, with increasing Yb concentration, the effective masses are reduced considerably. This observation cannot explain the heavy-fermion physics observed in specific-heat and resistivity data even for high Yb concentrations. High Dingle temperatures resolved in this study points to the fact that a possible disorder-induced strong scattering prevents the observation of heavy quasiparticles with short mean free paths in some presumably still existing heavy-electron $4f$ bands. However, the mechanism by which superconductivity can emerge from these charge carriers remains elusive. For the pure $YbCoIn_5$ ($x = 1$), the observed Fermi-surface topology is very similar to the calculated Fermi surfaces of other 115 compounds without $4f$ contributions to the band structure.

6. Iron-based ternary phosphides $LaFe_2P_2$ and $CeFe_2P_2$

In this chapter the results of comprehensive de Haas-van Alphen studies on the iron-based ternary phospides $LaFe_2P_2$ and $CeFe_2P_2$ will be presented. The angular-dependent observation of dHvA signals allowed to construct the extremal Fermi-surface areas which show good agreement with density-functional-theory calculations for $LaFe_2P_2$. Contrary, the band-structure calculations realized for $CeFe_2P_2$ cannot correctly describe the experimentally obtained dHvA results.

6.1. Iron-based superconductors

Historically, using magnetic elements, especially ferromagnets, as potential component for new superconducting materials was not supposed to be appropriated. Elemental iron is strongly magnetic, its locally polarized spins, all pointing in the same direction, create a magnetic field that would destroy any Cooper pair that tried to form. That is why the discovery of a non-Cu oxide with a relatively high superconducting transition temperature in the presence of a magnetic iron content was surprising and absolutely unexpected. This new family of iron-based superconductors has stimulated enormous research activities, raising hopes of setting a new T_c record and of explaining the role of magnetism in high-T_c superconductivity [149].

Within a short period of competitive search, the general family of these materials has exceed more than fifty different compounds approaching a superconducting transition temperature of 55 K.

This value, in the same way as in copper oxides, does not fit to the standard BCS theory that has difficulties describing such high transition temperatures. At the same time, the discovery of Fe-based superconductors points to the fact, that unconventional high-T_c superconductivity is not unique and not limited to the copper oxides [150].

Experiments and theory agree that Fe-based superconductors most probably possess unconventional superconductivity and the superconducting electrons flow within the FeAs layer. As can be seen in Fig. 6.1(a), the iron-containing layer is not flat, the pnictogen/chalogen atoms are arranged above and below the plane. Due to their bigger size compared to Fe atoms, they form into edged tetrahedra. The conducting FeAs layers are either stacked together, as in the 11 family, or are separated by blocking layers using alkali (111), alkaline-earth (122) or rare-earth and oxygen/fluorine (1111) or even more complicated perovskite-type combinations (32522 and 42622).

Due to the fact, that the basic behavior of several families of iron-based superconductors is found to be similar [149, 151, 152], this thesis will concentrate on the 122 type. Among all series of iron-based compounds,

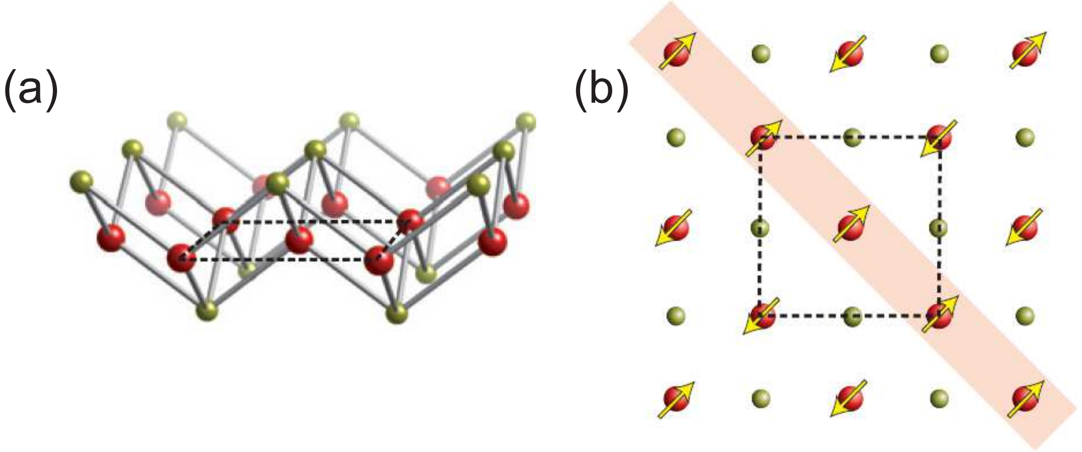

Figure 6.1.: *(a) Fe-based layer common to all superconductors of this family, with iron atoms shown in red and pnictogen/chalogen atoms in yellow. The dashed line indicates the size of the FeAs unit cell with two iron atoms owing to the staggered pnictogen positions. (b) The ordered spin arrangement in these materials is indicated by arrows [149].*

this class with the parent compounds AFe_2As_2 (A = Ba, Sr, Ca), so far is one of the most investigated.

6.1.1. Phase diagram

Figure 6.2 shows the phase diagram for the 122 type of iron-based pnictides. The diagram can be generated by manipulating the chemical or structural properties. At room temperature at ambient pressure in their undoped state iron pnictides are poor Pauli-paramagnetic metals. Below a certain temperature, for example, of about 140 K in the case of $BaFe_2As_2$ [153] the

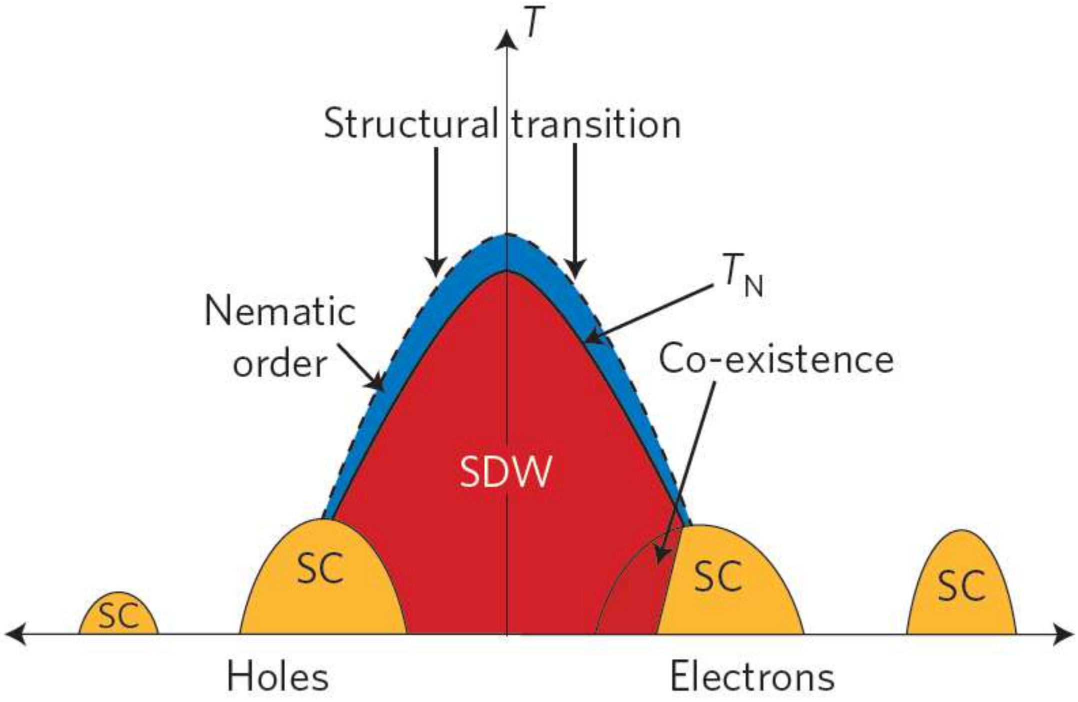

Figure 6.2.: *Schematic phase diagram of iron pnictides on hole or electron doping [150]. At relatively small dopings, superconductivity and antiferromagnetism co-exist. Superconductivity can be initiated not only by doping but also by applying pressure and/or replacing one isovalent pnictide element by another. The nematic phase in pnictides at $T > T_N$ is a subject of much debate. Superconductors at large doping are KFe_2As_2 for hole doping and AFe_2As_2 (A = K, Rb, Cs) for electron doping. Whether superconductivity in pnictides exists at all intermediate dopings is not yet clear.*

Fe sublattice undergoes a tetragonal-to-orthorhombic structural transition and a antiferromagnetic transition. It was predicted before the experiments [34], that antiferromagnetic order in all Fe-based superconductors has to have a wave vector oriented along $[\pi, \pi]$ in the tetragonal cell, where the spins are arranged as shown in Fig. 6.1(b), ferromagnetically along one direction of the iron sublattice and antiferromagnetically along the other. The antiferromagnetic ordering in iron arsenides most probably has an itinerant spin-density wave nature [154–156].

The superconducting state arises after the suppression of magnetism by applying pressure [157–162] or chemical substitution [29, 30, 163–166] or a combination of both [167]. In $BaFe_2As_2$, superconductivity emerges with systematic substitution of the (1) alkaline-earth Ba atoms with K [29] atoms, resulting in hole doping of the parent compound; (2) transition-metal Fe atoms with Co [30, 163] or Ni [164] atoms, thereby doping with electrons, or (3) pnictogen As atoms with P [166] atoms, i.e., isovalent doping to suppress magnetism without changing the carrier concentration.

As can be seen in Fig. 6.2, the phase diagram is nearly symmetric in both electron- and hole-doped regimes. Upon increase of the doping concentration, the magnetic ground state of the parent compound is suppressed. Then, a superconducting dome appears inside even the antiferromagnetic region. An overlap, which exists between antiferromagnetic and superconducting regions is still highly debated. Some scientists believe in coexistence of magnetism and superconductivity [168–170] in this region, whereas others claim that the magnetically ordered phase and the superconducting state are microscopically separated [171, 172].

6.1.2. Electronic structure

Since the discovery of high-T_c iron-based superconductors many theoretical studies [34, 35, 173–175] have been trying to shed light on the origin of their superconductivity. Because electrons close to the Fermi level are primarily responsible for this phenomenon, these theories proposed that the unique Fermi-surface topology plays a major role for the mechanism of superconductivity.

The band structure of all superconducting materials of this family [176–179] has been calculated using density functional theory. As a main result it was identified, that the Fermi surface, shown in Fig. 6.3(a), is mostly composed of five small sheets (i.e., five bands formed mostly by d-states of Fe are crossing the Fermi level), four of them being almost two-dimensional corrugated cylindrical tubes running parallel to the c axis: two at the centre of the Brillouin zone near the Γ point are hole-like and those at the zone corner near the M point are electron-like; the fifth sheet consists of a distorted sphere centered at the Z high-symmetry point. The presence of this spherical sheet, which due to its small contribution to the electronic density of states is usually neglected when analyzing the electronic properties of the superconducting state, may be very sensitive to structural details [180]. The basic topology through all investigated types of iron-based superconductors was reported to be similar except the hole-like Fermi surface at the Z point, which is flattened

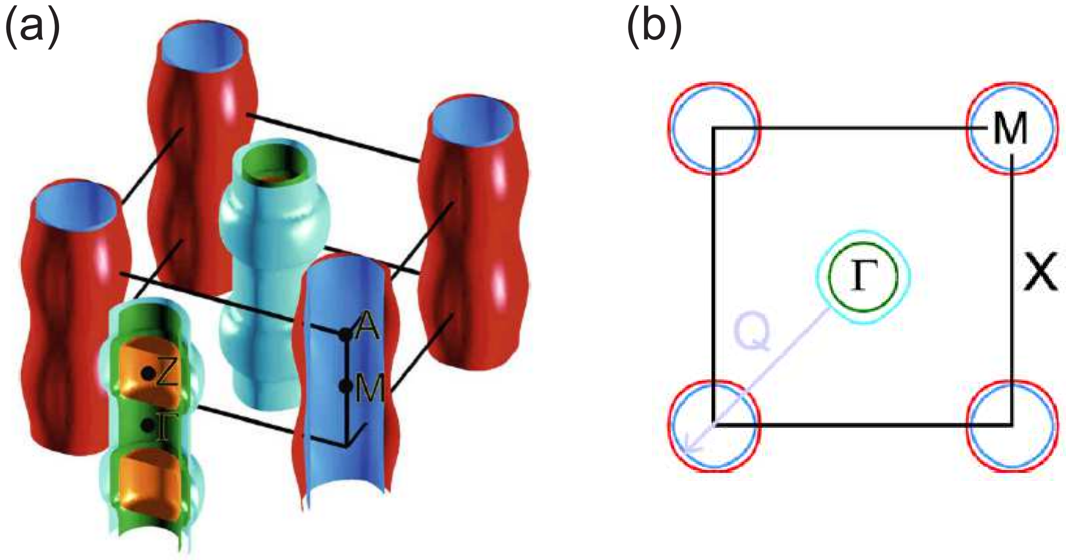

Figure 6.3.: *(a) The Fermi surface of LaFePO [181] and (b) its projection onto the momentum* $k_x - k_y$ *plane [182]. The momentum connecting two sets of Fermi surfaces, Q, is shown by the arrow.*

out for the 122 materials, suggesting a more three-dimensional character compared to the 1111 and 111 structures.

To confirm the predictions of the band-structure calculations, many experimental investigations, performed by angle-resolved photoemission spectroscopy (ARPES) and quantum-oscillation measurements, have been realized. The basic Fermi-surface topologies determined in ARPES studies on several 1111 materials such as LaFePO [183] and $NdFeAs_{0.9}F_{0.1}$ [184], as well as the 122 compounds $Ba_{1-x}K_xFe_2As_2$ [185–187], and $BaFe_2(As_{1-x}P_x)_2$ [188] are in excellent agreement with band-structure calculations.

Quantum oscillations measured in the antiferromagnetic state of the parent compounds $BaFe_2As_2$ [189, 190], $SrFe_2As_2$ [191], and $CaFe_2As_2$ [192] reveal that the Fermi surface is composed of one hole and two electron pockets, all of them are three dimensional and closed. These results are consistent with band-structure calculations if the Brillouin-zone reconstruction due to antiferromagnetic ordering is taken into account. One way to investigate the Fermi-surface properties of the iron arsenides in their normal state is to study the analogous nonmagnetic materials. Isovalent substitution of P for As or Ru for Fe allows to suppress magnetism without change in the number of electrons or holes. Band-structure calculations show that these materials have almost identical Fermi surfaces to the arsenides in their nonmagnetic state but they are either nonsuperconducting or have a low T_c. Quantum-oscillation experiments carried out on several paramagnetic members of the 1111 family, namely of LaFePO [181, 182, 193] and LaRuPO [194] and the 122 compounds $BaFe_2As_{1-x}P_x$ [195–197], $SrFe_2P_2$ [198] and $LaRu_2P_2$ [199] reveal an unreconstructed Fermi surface consisting of hole pockets at the Brillouin-zone centre and electron pockets at the zone corners.

As an important feature of the Fermi surfaces in these compounds, the electron and hole sheets are nearly nested. Geometrical nesting, as shown in Fig. 6.3(b), in iron-based pnictides originates from the shape of the Fermi surface and causes an enhancement of the quasiparticle scattering along the wave vector $Q \approx [\pi, \pi]$ in momentum space in the Brillouin zone. In many models [34–36, 173, 200] this nesting is supposed to lead to enhanced spin fluctuations that could stabilize both superconductivity and magnetism.

The effect of hole or electron doping on the electronic structure of iron-based pnictides is well understood by a rigid-band model. The basic Fermi-surface topology preserves its original shape, but the size of the Fermi-surface pockets was found to change either with hole doping as in $Ba_{1-x}K_xFe_2As_2$ [186] or electron doping as in $Ba(Fe_{1-x}Co_x)_2As_2$ [201,202]. It is important to emphasize that density-functional-theory calculations [178, 203] suggest that the main effect of charge doping on iron-based compounds is not on the density of states, but rather on the disruption of nesting and the relative size of electron and hole pockets.

6.2. Properties of $LaFe_2P_2$ and $CeFe_2P_2$

In the course of this thesis, a detailed studies of the Fermi-surface topology on two ternary iron-based phosphides $LaFe_2P_2$ and $CeFe_2P_2$ have been performed. These materials are isostructural to the high-temperature iron-based superconductor $Ba_{1-x}K_xFe_2As_2$. Both compounds crystallize in the tetragonal $ThCr_2Si_2$-type structure (space group $I4/mmm$) and belong to the 122 class of the iron-based pnictides. Their crystal structure is shown in Fig. 6.4. The corresponding lattice parameters [204] and magnetic properties [205] are listed in Table 6.1.

According to earlier magnetic-susceptibility measurements [205], $LaFe_2P_2$ is a Pauli-paramagnetic material with trivalent rare-earth La atoms, which do not carry magnetic moments. It was also found that $CeFe_2P_2$ has a temperature-independent susceptibility at temperatures above 75 K [204]. Thus, if the cerium atoms in $CeFe_2P_2$ were trivalent, one could expect Curie-Weiss behavior; on the other hand, one should anticipate Pauli paramagnetism for tetravalent cerium. Thereby the behavior observed for $CeFe_2P_2$ is typical for a compound with mixed (intermediate, fluctuating) valence.

Both materials had been checked for superconductivity, with negative results above 1.8 K [204, 205]. However, measurements presented here reveal possible evidence for traces of superconductivity in $CeFe_2P_2$ below 0.65 K.

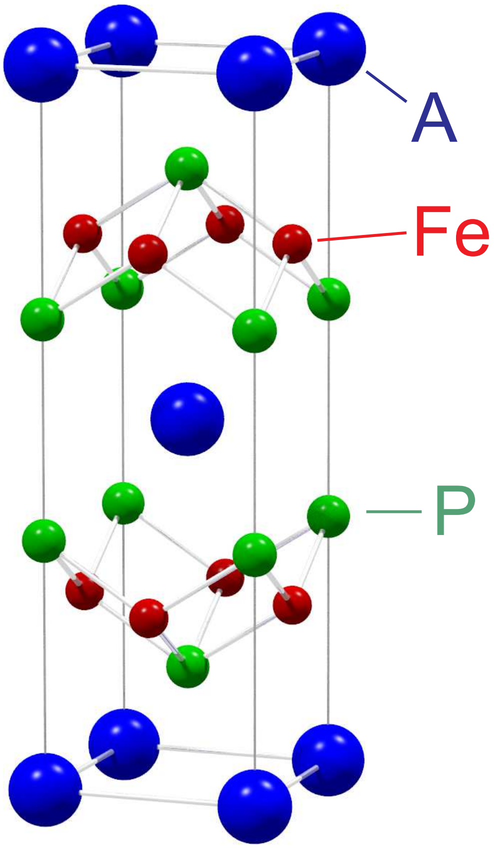

Figure 6.4.: *Tetragonal crystal structure of iron-based pnictide AFe_2P_2 (A = La, Ce).*

Table 6.1.: Crystallographic and magnetic parameters of the iron-based pnictides $LaFe_2P_2$ and $CeFe_2P_2$.

Parameters	$LaFe_2P_2$	$CeFe_2P_2$
Space group	$I4/mmm$	$I4/mmm$
Unite-cell parameter, Å	$a = b = 3.838$	$a = b = 3.852$
	$c = 11.006$	10.314
V, nm^3	0.1621	0.1530
P - P distance	3.176	2.864
Magnetic properties	Pauli paramagnetic	Intermediate valence
A^+	La^{3+}	$Ce^{3+/4+}$

6.3. Results and discussion

6.3.1. Fermi-surface investigation of $LaFe_2P_2$

In this thesis, the investigation of the Fermi-surface topology by use of the de Haas-van Alphen effect has been realized by means of a capacitive cantilever-torque technique. The sample used for this investigation was a non-superconducting $LaFe_2P_2$ single crystal with dimensions of about $0.15 \times 0.1 \times 0.05\,\mathrm{mm}^3$, grown using a tin-flux method as described in [204, 206] by

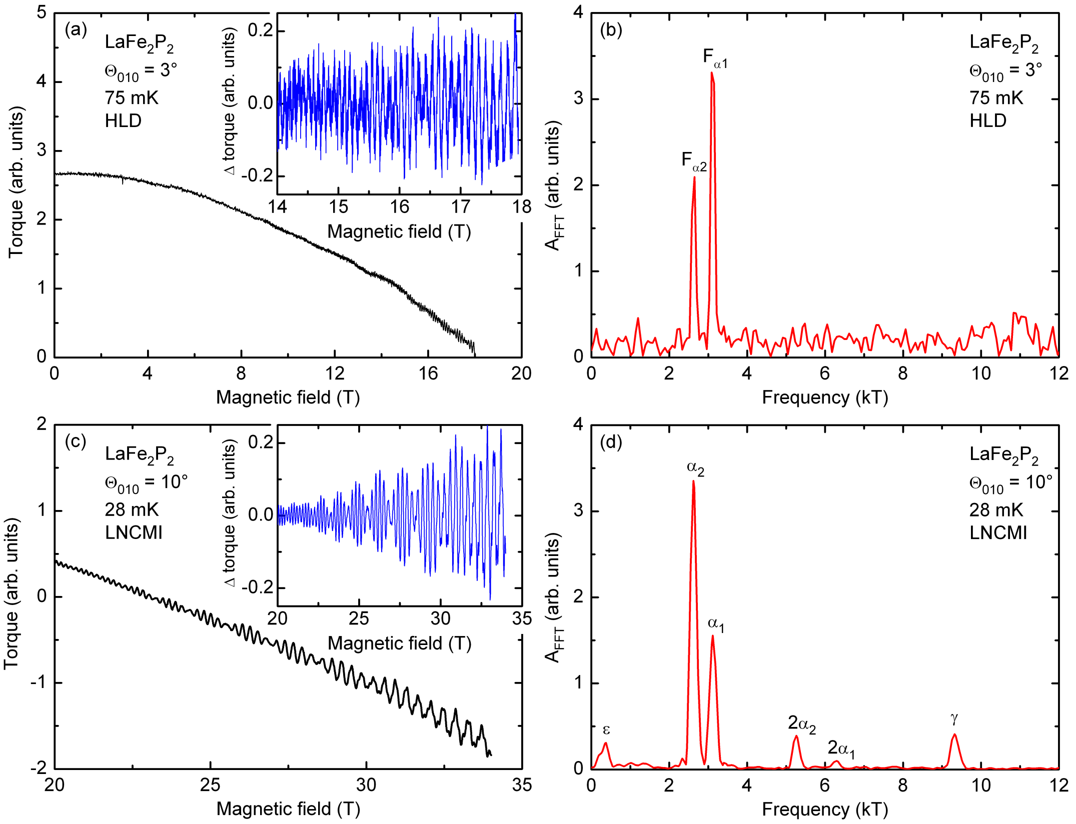

Figure 6.5.: *Typical torque signals of $LaFe_2P_2$ measured (a) with the magnetic field tilted by 3° off the c axis at $T = 75\,mK$ and (c) with the magnetic field angle $\Theta_{010} = 10°$ at $T = 28\,mK$. The insets show the oscillating dHvA signals after subtracting smooth backgrounds from the torque data. Corresponding Fourier spectra of the background-subtracted signals transformed in the field window between (b) 14 and 18 T and (d) 20 and 34 T.*

the group of Z. Fisk at the University of California, Irvine, USA. Two dHvA experiments were performed both at lowest temperatures down to 25 mK in a dilution refrigerator. One at the Hochfeld-Magnetlabor Dresden up to 18 T in a superconducting magnet and another one at the Laboratoire National des Champs Magnétiques Intenses, Grenoble, France in fields up to 34 T produced by a resistive magnet.

Figure 6.5(a) shows the raw torque signal, taken in Dresden at a temperature around 75 mK, versus applied magnetic field tilted by 3° off the c axis. The oscillatory torque signal after subtraction of the weak paramagnetic background (using a smooth polynomial of fourth order) is shown in the inset. As a result of the Fourier transformation of this signal in $1/B$ two main frequency components F_{α_1} and F_{α_2}, as is shown in Fig. 6.5(b), have been identified. Complementary to measurements realized in Dresden we have performed high-field dHvA studies in Grenoble. The raw torque signal taken in a magnetic field up to 34 T with tilted angle $\Theta_{010} = 10^\circ$ at a temperature around 28 mK is shown in Fig. 6.5(c). Fourier transformation of the background-subtracted data shown in the inset of Fig. 6.5(c) has revealed the spectrum with two new fundamental frequencies labeled as F_ε, F_γ and two harmonics $2F_{\alpha_1}$ and $2F_{\alpha_2}$, as evident in Fig. 6.5(d).

Rotating the field away from the [001] ($\Theta_{010} = 0^\circ$) axis towards [100] ($\Theta_{010} = 90^\circ$) even richer Fourier spectra were obtained. One of such examples is shown in Fig. 6.6(a) where the dHvA spectrum contains six distinct frequencies and two harmonics. Further rotation in this plane close to $B \parallel [100]$ [Fig. 6.6(b)] allowed to resolve only one strong peak, F_σ.

The full three-dimensional topology of the Fermi surface can be followed by mapping the evolution of the dHvA frequencies and their amplitudes versus angle. A three dimensional plot of the angle-dependent Fourier spectra of the dHvA frequencies and the intensity of their amplitudes in $LaFe_2P_2$ is shown in Fig. 6.7. These measurements have been realized at the HLD at temperatures around 75 mK, as the magnetic field is rotated around the [010] axis, Θ_{010}. The Fourier transformations have been performed in the field window between 14 and 18 T. In this particular experiment three intense features labeled as F_{α_1}, F_{α_2}, and F_σ can be recognized.

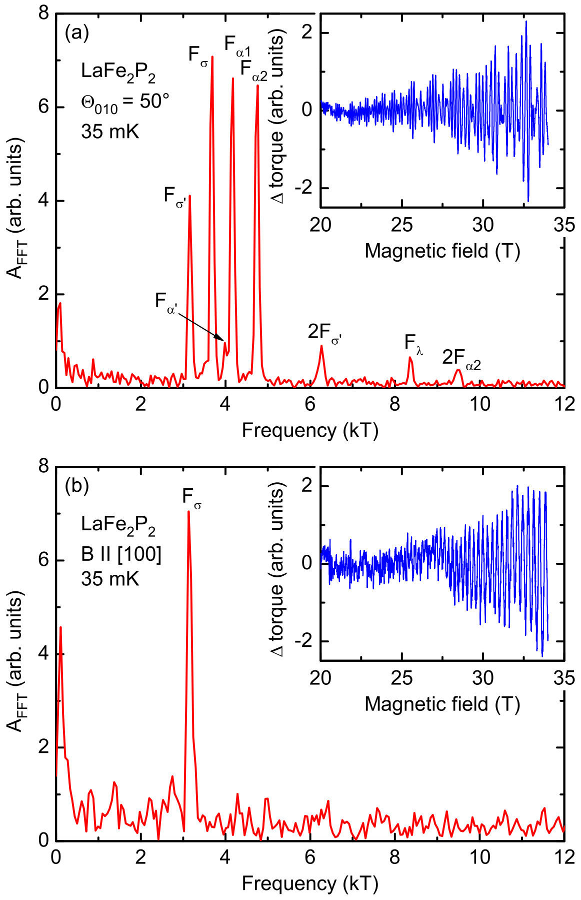

Figure 6.6.: *Fourier spectra of the background-subtracted torque signals shown in the insets when the magnetic field is aligned along (a)* $\Theta_{010} = 50^\circ$ *and (b)* [100] *axis.*

Generally, the data observed in this thesis are consistent with those recently reported in Ref. [194] up to 17 T, however our measurements allowed to resolve the following difference:

- the low-field data below 18 T uncovered at higher angles two additional peaks $F_{\alpha_1'}$ and $F_{\sigma'}$ (which probably originate from the same Fermi-surface sheets as branches F_{α_1} and F_{σ}),
- the high-field data above 18 T revealed at small angels the low-lying component F_{ε} and at higher angles two new distinct dHvA frequencies F_{γ} and F_{λ}.

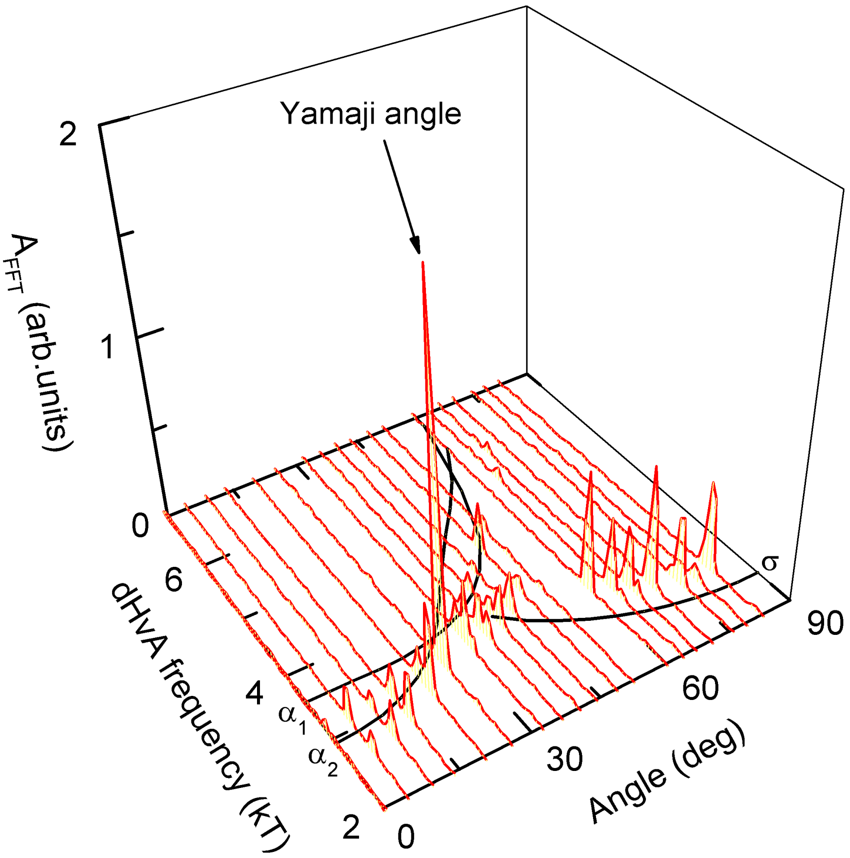

Figure 6.7.: *3D plot of the angle-dependent Fourier spectra for torque data in the field window between 14 and 18 T taken on $LaFe_2P_2$ at $T = 75$ mK rotating the field around the b axis. The extremal cross-sectional areas of the α_1, and α_2 orbits approach and finally match each other at the Yamaji angle, of $\Theta_{010} \approx 30°$, enhancing the amplitude of the oscillations.*

The angular dependence of all dHvA frequencies observed for $LaFe_2P_2$ for the magnetic field rotations around [010], Θ_{010}, and [110], Θ_{110}, as well as around the [001] axis, Θ_{001}, in measurements at the HLD (filled symbols) and for the field rotation around [010] collected at the LNCMI (open symbols) is shown in Fig. 6.8.

As can be seen in Fig. 6.8 for Θ_{110} rotation the angular dependence of the dHvA signals are very similar to the Θ_{010} rotation. However, the data for rotation in the basal plane resolves only one almost angular-independent dHvA frequency F_σ.

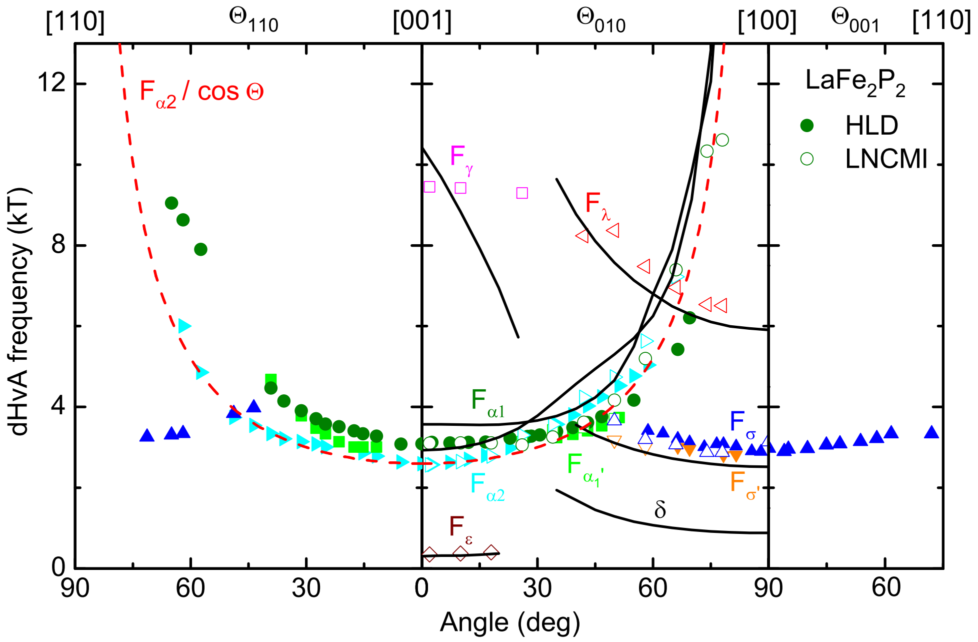

Figure 6.8.: *Angular dependence of the observed dHvA frequencies of* $LaFe_2P_2$ *upon rotation around all principal directions. Different symbols correspond to experimental data obtained at HLD (filled symbols) and at LNCMI (open symbols). The red dashed line depicts a* $F_{\alpha_2}/\cos\Theta$ *dependence expected for a cylindrical Fermi surface and the black solid lines are predictions from DFT calculations.*

From Figs. 6.7 and 6.8 it is evident that the branches F_{α_1} and F_{α_2} roughly follow a behavior according to $F \propto 1/\cos\Theta$ that is expected for a two-dimensional cylindrical Fermi surface. However, by plotting $F\cos\Theta$ as a function of a field angle, Θ, the deviation from an exact two-dimensional Fermi surface becomes clear [Fig. 6.9].

The simplest deviation from this exact behavior two dimensionality is a cosinusoidal corrugation of the Fermi cylinder along the c axis that can be described analytically in terms of Yamaji analysis [86] (see Chapter 3.4)

$$F_{min,max}(\Theta)\cos\Theta = \frac{F^0_{max} + F^0_{min}}{2} \pm \frac{F^0_{max} - F^0_{min}}{2} J_0(ck_\mathrm{F}\tan\Theta). \tag{6.1}$$

In the context of this analysis, two closely-spaced dHvA frequencies F_{min} and F_{max} arise from the two extremal cross-sections of the corrugated quasi-two-dimensional Fermi surface, that have opposite curvature. The

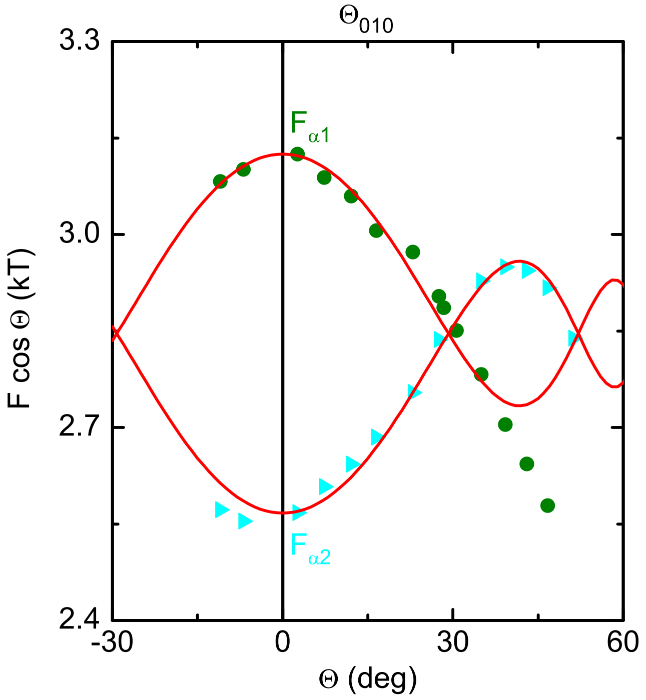

Figure 6.9.: *Angular dependence of the dHvA frequencies, F_{α_1} and F_{α_2} plotted in terms of $F\cos\Theta$. The branches cross at $\Theta_{010} \approx 30°$. The red solid lines are calculations for a simple cosinusoidally corrugated cylinder yielding the Yamaji angle.*

lower frequency F_{min} originates from the minimal extremal cross-sectional area of the Fermi surface and the upper frequency F_{max} from the maximal area of the same Fermi-surface sheet. The values of these frequencies can be taken directly from the experimental data at $\Theta = 0°$, so this equation has only k_F as a free parameter.

For $LaFe_2P_2$, $F_{min} = F_{\alpha_2} = 2567\,\mathrm{T}$ and $F_{max} = F_{\alpha_1} = 3125\,\mathrm{T}$. When using $k_F = 3.91\,\mathrm{nm}^{-1}$, Eq. (6.1) results in the red solid lines shown in Fig. 6.9. For a circular Fermi surface cylinder $k_F = 2.94\,\mathrm{nm}^{-1}$ would result. Obviously, the Fermi surface cylinder has an ellipsoidal cross-section. Indeed the band-structure calculations predict the correct Yamaji angle (see Fig. 6.8).

At this angle the Bessel function becomes zero, all the cross-sectional extremal areas are equal and their contributions to the total magnetization interfere constructively to give a large increase of the oscillatory amplitude.

In $LaFe_2P_2$, such a Yamaji angle is observed at $\Theta_{010} \approx 30^\circ$ as seen in Figs. 6.8 and 6.9 and is also evidenced by the strong enhancement of the dHvA amplitude at this angle in Fig. 6.7.

The band structure of $LaFe_2P_2$ has been calculated in the framework of density-functional theory in the group of M. Côté at the Université de Montréal, Québec, Canada. A plot of the calculated electron energies versus momentum along the principal directions is presented in Fig. 6.10(a). Before starting the discussion, it is useful to review the conventional nomenclature of the symmetry points in the Brillouin zone. The inset of Fig. 6.10(a) shows the Brillouin zone with the important symmetry points: $\Gamma\,(0, 0, 0)$, $Z\,(0, 0, 2\pi/c)$, $X\,(\pi/a, \pi/a, 0)$, $M\,(0, 2\pi/a, 0)$, and $P\,(\pi/a, \pi/a, \pi/c)$.

The calculated Fermi surface of $LaFe_2P_2$ is anisotropic three dimensional and it consists of: (1) a large hole sheet in the form of a doughnut at the Z point of the Brillouin zone [Fig. 6.10(b)], (2) an electron sheet in the form of a warped quasi-two-dimensional cylinder around the X point [Fig. 6.10(d)], and (3) one complicated three-dimensional hole sheet centred at Γ [Fig. 6.10(c)]. Despite some differences to the Fermi surface reported for $LaFe_2P_2$ earlier in Ref. [194], the topology obtained in this thesis is very similar to one recently reported in Ref. [199] for $LaFe_2P_2$ and $LaRu_2P_2$ ($T_c = 4\,\mathrm{K}$), and in Ref. [207] for $CaFe_2P_2$ in its collapsed tetragonal phase.

Contrary to most other 1111 and 122 iron-based pnictides, the calculated Fermi-surface topology for $LaFe_2P_2$ is clearly different. The hole Fermi surface shown in Fig. 6.10(b) has changed from two quasi-two-dimensional cylinders to a single flat doughnut. The electron sheets have also become more warped but still keep their cylindrical shape. In addition, unlike known from other iron-based pnictides, a new complicated hole Fermi surface centred at Γ has been identified in $LaFe_2P_2$ [Fig. 6.10(c)].

The extremal cross-sectional areas for the various angles have been calculated from these Fermi-surface geometries and depicted as the solid black lines in Fig. 6.8. The dHvA frequencies experimentally obtained during this thesis for $LaFe_2P_2$ at various magnetic-field angles are collected in Table 6.2 and compared to the results of band-structure calculations.

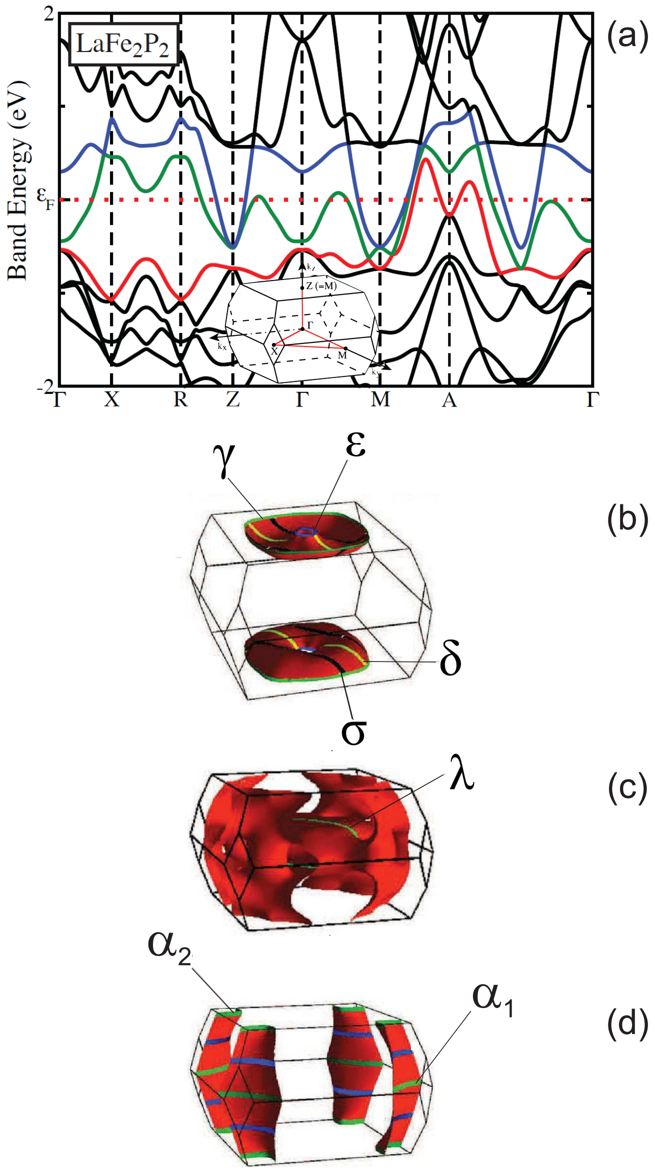

Figure 6.10.: *The electronic structure and Fermi surface of $LaFe_2P_2$ from DFT calculation. (a) The calculated electronic energy dispersion of $LaFe_2P_2$ along principal symmetry directions. The Fermi energy is denoted by ε_F. The blue, green, and red bands, which consist of Fe-3d and P-2p components, cross the Fermi energy. The inset shows the Brillouin zone with the symmetry points for the body-centered-tetragonal lattice. (b), (c) and (d) The Fermi surfaces of $LaFe_2P_2$ with their highlighted extremal orbits shown in black, green, blue, and yellow derived from density-functional-theory calculations and labeled according to the measured dHvA frequencies.*

Well agreement between calculations and experiment makes it possible to identify the observed dHvA frequencies with the following extremal orbits of the Fermi surface:

- the lowest dHvA frequency F_ε corresponds to the small hole pocket of the doughnut Fermi surface [6.10(b)],
- the dHvA branch F_σ for rotation in the Θ_{010} plane exist only in the angular range between 40 and 90° as well as its satellite $F_{\sigma'}$ and denotes the extremal cross-sectional area of the hole-like sheet in the form of a doughnut [6.10(b)]. For rotation in conducting basal plane F_σ can be followed in the entire angular range with roughly constant frequency.
- The dHvA branches F_{α_1} and F_{α_2} can be ascribed to the maximum and minimum cross sections of the warped cylindrical electron-like Fermi surface situated around X [6.10(d)]. The cylinders originate from the hybridization between the transition-metal d and the pnictogen p states near the Fermi level into plane bonds. Their existence is a common feature for 122 iron-based materials such as $CaFe_2P_2$ [207], $SrFe_2P_2$ [198], $BaFe_2P_2$ [197] as well as for non-Fe-based ternary phosphides such as $BaNi_2P_2$ [208] and $LaRu_2P_2$ [199]. Rotation of the field away from the c axis leads to a decrease of the frequency difference between F_{α_1} and F_{α_2} until they are finally match at the Yamaji angle of $\Theta_{010} \approx 30°$ [marked in Figs. 6.7 and 6.9] which agrees well with the value of 30° derived from the band-structure calculations.
- The dHvA frequency F_λ originates from the complicated strongly-folded three-dimensional multi-connected Fermi-surface sheet [6.10(b)].
- Unlike the other orbits obtained in measurements up to 34 T, the branch F_γ does not fit to the density-functional theory calculations. The experimentally obtained result seems to be much flatter then theoretically predicted.
- One remaining orbit δ has not been detected in presented measurements with magnetic field up to 34 T.

6.3.2. Effective masses of $LaFe_2P_2$

By measuring the temperature dependence of the quantum-oscillation amplitudes of $LaFe_2P_2$ the band-selective effective masses, m^*, have been evaluated at various magnetic-field orientations in the conventional manner using the Lifshitz-Kosevich formalism (Chapter 3.2). Figure 6.11 shows the data for two different measurements which were analysed in this thesis.

The background-subtracted signals measured at the Hochfeld-Magnetlabor Dresden in magnetic fields up to 18 T at different temperatures ranging

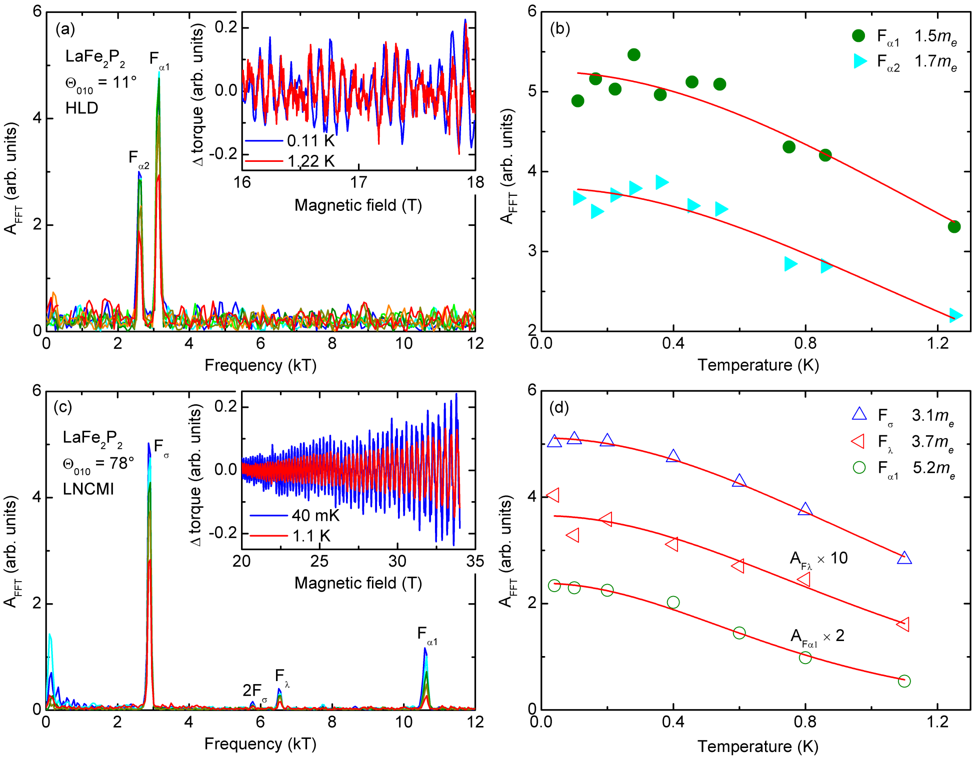

Figure 6.11.: *Thermal evolution of the dHvA spectra after fast Fourier transformations obtained on $LaFe_2P_2$ (a) at the HLD for the applied magnetic field oriented 11° off the c axis and (c) at the LNCMI-Grenoble for the tilt angle $\Theta_{010} = 78°$. The insets show the corresponding background-subtracted torque data recorded at various temperatures between 0.04 and 1.22 K. Temperature dependences of the oscillation amplitudes of (b) the frequencies F_{α_1} and F_{α_2} of the cylindrical Fermi surface and of (d) the branches F_σ, F_λ and F_{α_2} of $LaFe_2P_2$.*

between 0.11 and 1.22 K are shown in the inset of Fig. 6.11(a). For these measurements, the magnetic field angle Θ_{010} was tilted 11° off the c axis. The resulting Fourier transformations from these data are shown in the main panel of Fig. 6.11(a). The two fundamental frequencies F_{α_1} and F_{α_2} have been observed at all temperatures. These orbits belong to the electron quasi-two-dimensional cylindrical Fermi surface shown in Fig. 6.10(d). Figure 6.11(b) shows the temperature dependence of the Fourier amplitudes. The fit to the Lifshitz-Kosevich expression (red solid lines) allowed the determination of the effective cyclotron mass for each orbit. The values obtained for $m^*_{\alpha_1}$ and $m^*_{\alpha_2}$ are $1.5\,m_e$ and $1.7\,m_e$, respectively. According to the $m^*/\cos\Theta$, expected for the angular dependence of the effective masses on a cylindrical Fermi surface, it is possible to estimate the effective masses at $B \parallel [001]$ ($\Theta_{010} = 0°$). The determined values $1.47\,m_e$ and $1.67\,m_e$ are close to,

Table 6.2.: The measured dHvA frequencies and effective masses for various extremal orbits of $LaFe_2P_2$ at different magnetic field directions in comparison with the values obtained from band-structure calculations.

		F (kT)		m^* (m_e)		λ^*	m^* (m_e) [194]
Direction	Orbit	Exp.	Cal.	Exp.	Cal.	$\frac{m^*_{Exp.}}{m_{Cal.}} - 1$	Exp.
$B \parallel [001]$	α_2	2.57	2.93	1.47	0.73	1.01	2.0
	α_1	3.13	3.57	1.67	0.76	1.2	2.7
$\Theta_{010} = 11°$	α_2	2.62	3.0	1.5	–	–	–
	α_1	3.14	3.56	1.7	–	–	–
$\Theta_{010} = 55°$	α_2	4.77	5.7	2.3	–	–	–
	α_1	4.17	5.5	2.9	–	–	–
$\Theta_{010} = 78°$	σ	2.88	2.59	3.1	–	–	–
	λ	6.51	6.11	3.7	–	–	–
	α_1	10.61	12.05	5.2	–	–	–
$B \parallel [100]$	σ	2.91	2.52	4.0	–	–	–

but smaller, than the values of 2.0 m_e and 2.7 m_e previously reported for these branches in Ref. [194].

The temperature-dependent dHvA data for the high-field range have been collected at the Grenoble Laboratoire National des Champs Magnétiques Intenses in magnetic fields up to 34 T at temperatures between 40 mK and 1.1 K with the magnetic field rotated 78° away from the [001] direction. After Fourier transformation of the data in the field window between 20 and 34 T three distinct dHvA frequencies F_{α_2}, F_σ and F_λ have been identified. The temperature-dependent dHvA amplitudes are shown in Fig. 6.11(d) together with the Lifshitz-Kosevich fits and the obtained effective masses ranging between 3.1 and 5.2 m_e.

The DFT calculations have found effective masses at $B \parallel [001]$ to be $m^*_{\alpha_2} = 0.73\, m_e$ and $m^*_{\alpha_1} = 0.76\, m_e$. Hence, the many-body mass-enhancement factors $\lambda^* = m^*_{Exp.}/m_{Cal.} - 1$, have been calculated yielding the values of $\lambda^*_{\alpha_2} = 1.01$ and $\lambda^*_{\alpha_1} = 1.2$, as reported in Table 6.2. This can be compared to the mass enhancement calculated from the electronic specific-heat coefficient, $\lambda^\gamma = \gamma_{Exp.}/\gamma_{Cal.} - 1$, giving the value of $\lambda^\gamma = 0.8$ [199].

Similar mass enhancements with $\lambda \approx 1$ have been identified in several other iron-based pnictides such as LaFePO ($\lambda^* = 1$) [182], $BaFe_2As_2$ ($\lambda^* = 0.7 - 1$) [190], $SrFe_2As_2$ ($\lambda^* = 0.85$) [191], $CaFe_2P_2$ ($\lambda^* = 0.45 - 0.51$) [207] as well as in the non-Fe-based phosphides LaRuPO ($\lambda^\gamma = 0.95$) [194], and $LaRu_2P_2$ ($\lambda^* = 0.8$) [199].

6.3.3. Fermi-surface investigation of $CeFe_2P_2$

The high-quality single crystals of $CeFe_2P_2$ for this investigation have been grown from In flux by two different scientific groups. Samples A and B have been prepared in the group of Z. Fisk at the University of California, Irvine, USA and sample C has been synthesized in the group of C. Geibel at the Max Planck Institute for Chemical Physics of Solids, Dresden, Germany.

Torque-magnetometry measurements have been performed by using capacitive cantilevers in a 20-T superconducting magnet on samples A and C at the Hochfeld-Magnetlabor Dresden and in a 35-T Bitter magnet on sample

B at the Laboratoire National des Champs Magnétiques Intenses, Grenoble, France. Both experimental setups were equipped with ^{3}He/^{4}He dilution refrigerator which covers the temperature range between 25 mK and 1.2 K.

Figure 6.12(a) shows a typical torque signal taken on sample B in high magnetic fields up to 34 T and at low temperature (about 30 mK) for the tilt angle $\Theta_{010} = 40^\circ$ between the magnetic field and the crystallographic c axis. The background torque signal varies approximately quadratically with applied magnetic field as expected for paramagnetic materials. Quantum oscillations, which are superimposed onto this background, can be resolved

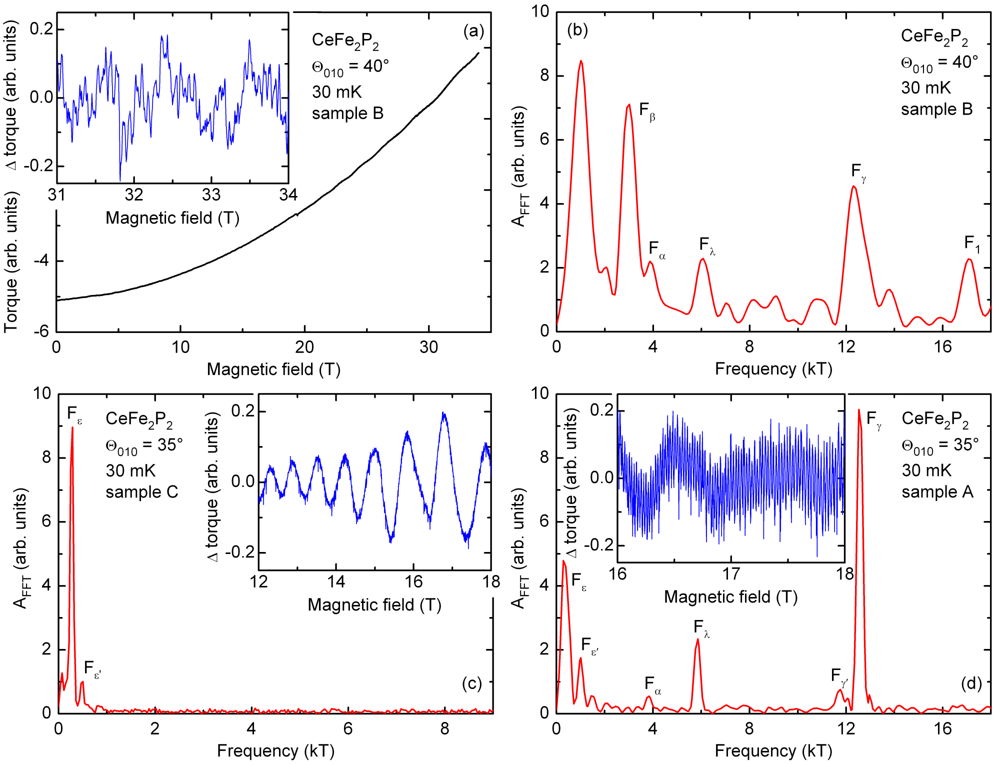

Figure 6.12.: *(a) Typical torque signal of* CeFe$_2$P$_2$ *(sample B) measured at* $T = 30$ *mK in magnetic fields up to 34 T for the magnetic-field angle* $\Theta_{010} = 40^\circ$*. In the inset, data after background subtraction are shown. (b) Fourier spectrum of the oscillating signal taken in the field range between 31 and 34 T. (c) and (d) Fourier spectra of the background subtracted torque signals shown in the insets and measured at* $T = 30$ *mK up to 18 T for the magnetic field angle* $\Theta_{010} = 35^\circ$ *(c) for sample C and (d) for sample A, respectively.*

only in high magnetic fields. By subtracting a smooth background from the torque data by using a forth-order polynomial, the quantum oscillations become visible and can be clearly seen in the inset of Fig. 6.12(a).

By performing a Fourier transformation on the oscillating signal from Fig. 6.12(a) with respect to the inverse magnetic field, the spectral richness of the signal can be realized in the corresponding Fourier spectrum, as is shown in Fig. 6.12(b). The dHvA oscillations for samples A and C, collected at 30 mK in magnetic fields up to 18 T at the angle $\Theta_{010} = 35°$ are shown in the insets of Fig. 6.12(c) and Fig. 6.12(d), respectively. The Fourier transforms of these measurements are shown in the main panels. The spectral distribution of the obtained dHvA frequencies is clearly different for these two samples. While for sample A the dHvA spectrum is identical to that of sample B, the spectrum for sample C reveals only one dominant frequency component F_ε and the satellite $F_{\varepsilon'}$ nearby.

As a further example for measurements taken, Fig. 6.13 represents the background-subtracted torque signals measured up to 18 T at temperatures of about 30 mK together with their Fourier transforms performed in the field window between 16 and 18 T for the magnetic fields applied along the [001] [Fig. 6.13(a)] and along the [100] [Fig. 6.13(b)] axis. At small angles close to $B \parallel [001]$ the strongest amplitude peak is low-lying F_ε. Fourier spectra of all investigated $CeFe_2P_2$ single crystals are dominated by this frequency. Rotating away from the [001] towards the [100] at higher angles close to $\Theta_{010} = 35°$ the amplitude of the dHvA frequency F_γ becomes significant. Further rotation towards $B \parallel [100]$ reveals the Fourier spectrum with the strongest frequency component F_λ and its satellite $F_{\lambda'}$.

In total for $CeFe_2P_2$ seven dHvA frequencies have been recognized and labeled as F_α, F_β, F_γ, F_ε, F_λ, and F_1. Each of these frequencies is directly related to an extremal cross-sectional Fermi-surface area, A_F, perpendicular to the applied magnetic field via the Onsager's relation (Eq. (3.7)). From their evolution as the field is rotated from being along the crystallographic [001] axis [Fig. 6.13(a)] towards the [100] axis [Fig. 6.13(b)], a more detailed three-dimensional picture of the shape and size of the Fermi-surface sheets can be gained.

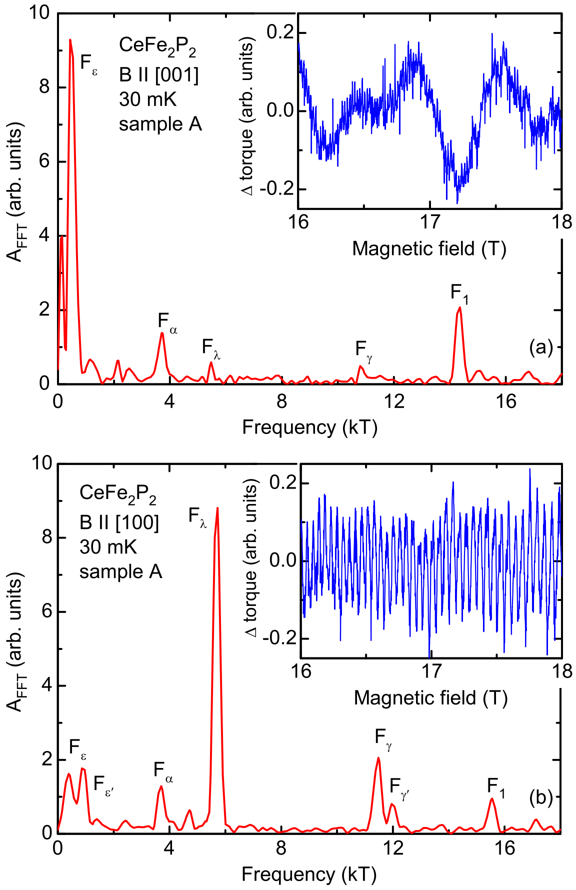

Figure 6.13.: *The background-subtracted torque signals measured on sample A of* $CeFe_2P_2$ *recorded at 30 mK with magnetic field directions aligned along the (a)* [001] *and (b)* [100] *axis together with the corresponding Fourier-transformed spectra.*

The angular dependence of the observed oscillation frequencies for $CeFe_2P_2$ single crystals is shown in Fig. 6.14. Different symbols correspond to samples C (half-filled symbols) and A (filled symbols) measured within the *ac* plane (a plane which is perpendicular to the conducting FeP layers), and sample B (open symbols) rotated around the [010] as well as around the [001] axis.

The dHvA frequencies observed on samples A and B agree well in the entire range of measured orientations. However, sample C shows only one distinct low frequency F_ε and its satellite $F_{\varepsilon'}$.

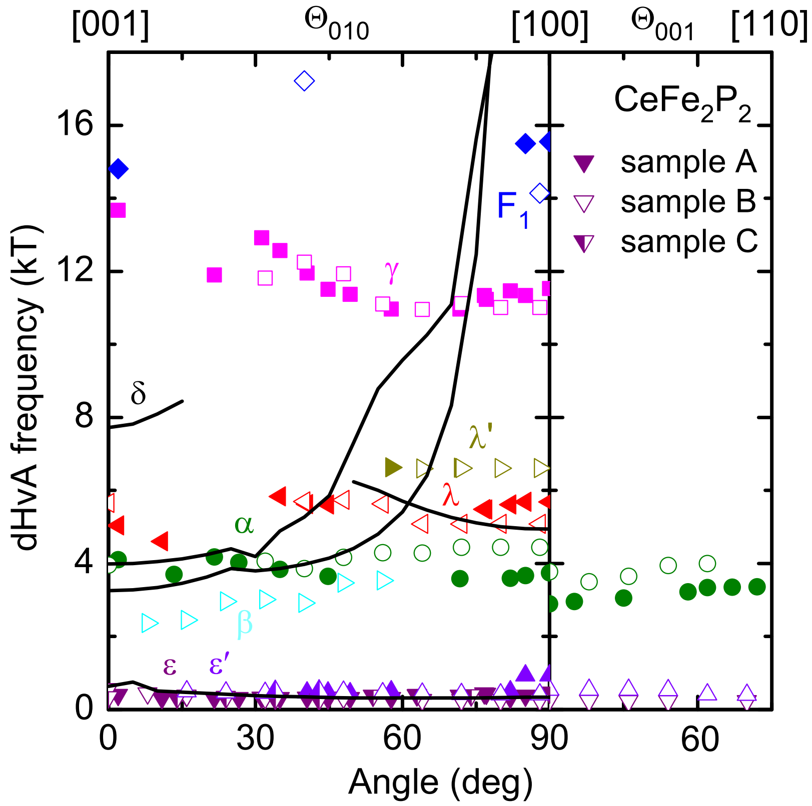

Figure 6.14.: *Angular dependence of the experimentally obtained dHvA frequencies in the two symmetry planes Θ_{010} and Θ_{001} in comparison with density-functional theory calculations. Different symbols correspond to sample A (filled symbols), B (open symbols), and sample C (half-filled symbols). The calculated data are shown by the black solid lines.*

In order to better understand the Fermi-surface properties of $CeFe_2P_2$ density-functional-theory calculations were performed in the group of M. Côté at the Université de Montréal, Québec, Canada. The resulting band structure for all principal directions is shown in Fig. 6.15(a). As suggested by these calculations, two bands, shown in blue and green are crossing the Fermi energy, giving rise to two different Fermi-surface sheets. Figures 6.15(b) and 6.15(c) visualize the calculated Fermi surface, which is composed of a large branched hole-like sheet centered at the top of the Brillouin zone and a warped quasi-two-dimensional electron-like sheet situated at the zone edge.

Table 6.3.: The measured dHvA frequencies of $CeFe_2P_2$ single crystals at magnetic field aligned along the c and a axes in comparison with the values obtained from the band-structure calculations.

Direction	Orbit	$F_{Cal.}$ (kT)	$F_{sampleA}$ (kT)	$F_{sampleB}$ (kT)	$F_{sampleC}$ (kT)
$B \parallel [001]$	ε	0.64	0.41	0.56	0.34
	β	3.26	–	–	–
	α	3.99	4.1	3.64	–
	λ	–	5.04	5.65	–
	δ	7.72	–	–	–
	γ	–	13.67	–	–
	F_1	–	14.81	–	–
$B \parallel [100]$	ε	0.34	0.47	0.26	–
	ε'	–	0.94	0.41	–
	α	–	3.74	4.44	–
	λ	4.94	5.69	5.08	–
	λ'	–	–	6.61	–
	γ	–	11.53	11.01	–
	F_1	–	15.55	14.14	–

For comparison with the experimentally obtained angular-resolved dHvA data the calculated extremal orbits of each Fermi-surface sheet have been plotted in Fig. 6.14 (black solid lines) as a function of magnetic field angle as the field is rotated from c towards the a axis. For these two principal orientations the numerical values are given in Table 6.3.

When comparing experiments and predictions it becomes obvious that simple density-functional calculations cannot correctly describe the complicated Fermi-surface properties of $CeFe_2P_2$. However, from dHvA measurements we can make several statements regarding the most probable Fermi-surface topology.

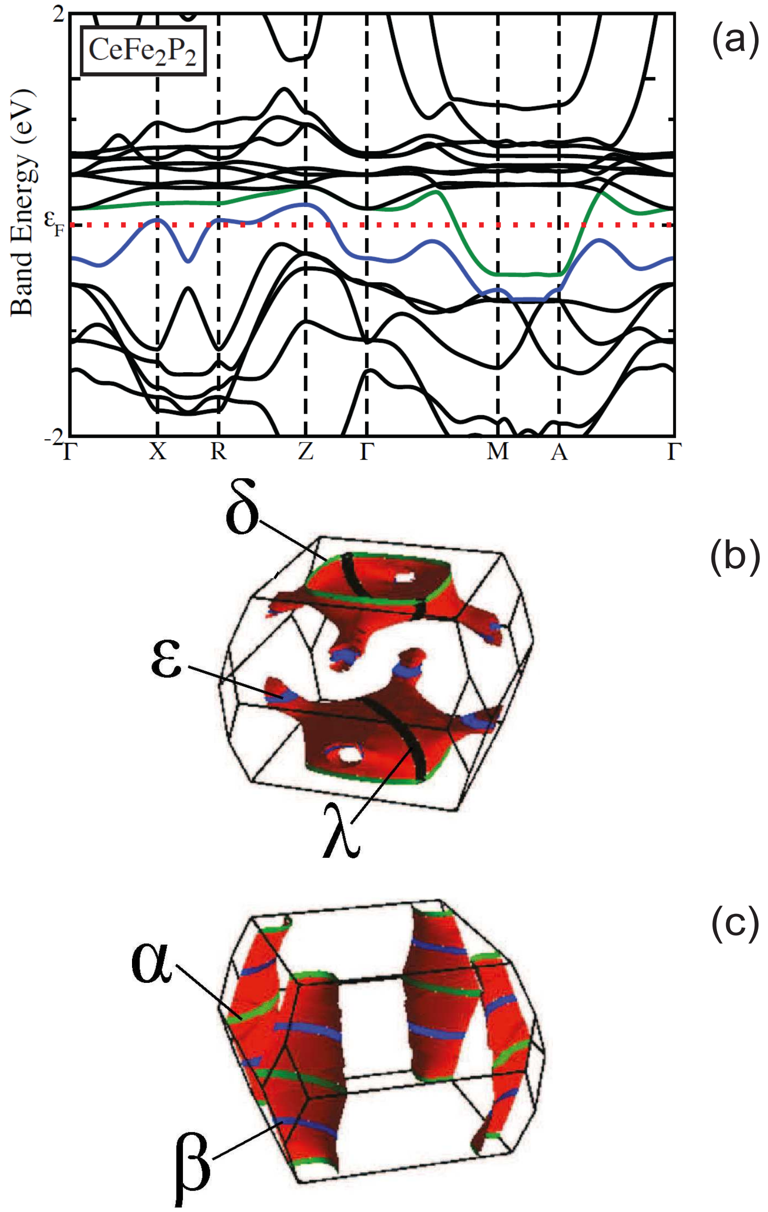

Figure 6.15.: *(a) The calculated electronic band structure of $CeFe_2P_2$ along the principal symmetry directions. The Fermi energy is indicated by ε_F. The blue and green bands cross the Fermi level. (b) and (c) The computed Fermi surfaces of $CeFe_2P_2$ from the density-functional theory calculations. The black, blue, and green lines depict orbits of extremal area.*

- The low-frequency dHvA branch F_ε, which corresponds to the smallest extremal cross-sectional area of the Fermi surface, has been observed in the entire range of measured orientations with nearly constant frequency in all investigated $\mathrm{CeFe_2P_2}$ single crystals. This frequency correlates with one small closed three-dimensional pocket.
- The branch F_λ and its satellite $F_{\lambda'}$ have been observed in sample A and B for rotation in the plane Θ_{010} in the angular range between 50 and 90°. This frequency is in good agreement with the λ orbit derived from calculations and could be ascribed to the extremal cross-sectional area of the large hole-like branched Fermi surface shown in Fig. 6.15(b).
- The warped quasi-two-dimensional electron-like cylinders shown in Fig. 6.15(c) are situated at the Brillouin zone edges and according to the band-structure predictions may be associated with the dHvA frequencies F_α and F_β. These frequencies should follow a $F \propto 1/\cos\Theta$ behavior, which is known for quasi-two-dimensional cylindrical Fermi surfaces (see the dHvA branches F_{α_1} and F_{α_2} in $\mathrm{LaFe_2P_2}$, Fig. 6.8). However, from the measured dHvA data it is clear that these branches show only a small angular dependence and follow nearly a closed spherical shape of the corresponding Fermi surface.
- The dHvA frequency F_γ was experimentally observed as well only for the samples A and B. This branch could be followed in the Θ_{010} angular range between 30 and 90°. At several angles, the dHvA spectrum was dominated by this frequency.
- The high-frequency F_δ (predicted by theory only within 15° off the crystallographic [001] direction) has not been observed in these measurements up to 34 T. This branch is derived from the approximately square-like cross section centered at the top of the Brillouin zone giving rise to the large hole-like sheet [Fig. 6.15(c)].
- The remaining frequency F_1 has been found in samples A and B only at very few angles close to the crystallographic [001] and [100] axis. The band-structure calculations give no hint to such a high-frequency orbit.

In fact, the experimental data largely disagree with the theoretical predictions. A possible reason for that might be a strong influence of the Ce $4f$ electrons on the Fermi surface of $CeFe_2P_2$.

6.3.4. Effective masses of $CeFe_2P_2$

The temperature-dependent oscillating torque signals after background subtraction measured on sample B of $CeFe_2P_2$ at the Grenoble Laboratoire National des Champs Magnétiques Intenses in magnetic fields between 20 and 34 T at temperatures between 65 mK and 1 K with $B \parallel [100]$ axis are shown in the inset of Fig. 6.16(a).

The main panel of Fig. 6.16(a) illustrates the Fourier spectra of the data yielding three pronounced peaks denoted as F_ε, $F_{\varepsilon'}$, and F_α. The quantum-oscillation amplitudes were suppressed only slightly in the available temperature range of the dilution refrigerator. Correspondingly, the dHvA amplitudes as a function of temperature show a large scattering [Fig. 6.16(b)]. The fits by use of the temperature-dependent factor of the Lifshitz-Kosevich formula are shown in Fig. 6.16(b) giving values ranging from 2.2 to 2.9 m_e as reported in Table 6.4. The effective masses extracted from DFT calculations at $B \parallel [001]$ axis are in the range from 1.53 to 1.61 m_e and collected in Table 6.4 as well.

Table 6.4.: The effective masses of $CeFe_2P_2$ measured at $B \parallel [100]$ axis as well as the extracted from band-structure calculations at $B \parallel [001]$ axis.

		m^* (m_e)	
Direction	Orbit	Exp.	Cal.
$B \parallel [001]$	β	–	1.61
	α	–	1.53
$B \parallel [100]$	ε	2.2	–
	ε'	2.9	–
	α	2.2	–

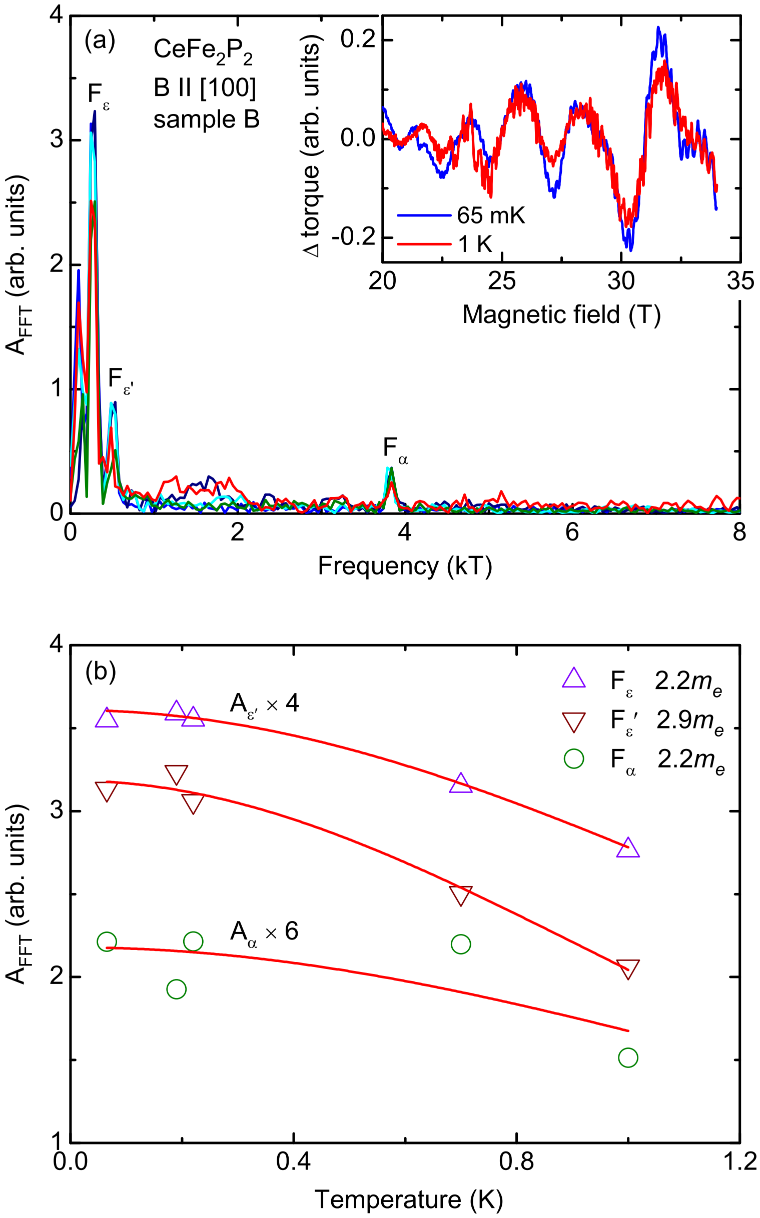

Figure 6.16.: *(a) Thermal evolution of the dHvA spectrum after fast Fourier transformation of the torque data obtained on sample B of* $CeFe_2P_2$ *with the magnetic field parallel to the* [100] *axis. In the inset the background-subtracted torque signals recorded at 0.065 and 1 K are shown. (b) Temperature dependence of the dHvA amplitudes shown for the frequencies* F_ε, $F_{\varepsilon'}$, *and* F_α. *The solid lines are fits of the Lifshitz-Kosevich formula to the experimental data points.*

6.3.5. Evidence for superconductivity in $CeFe_2P_2$

Routine torque measurements conducted on $CeFe_2P_2$ revealed a clear hysteresis loop between the up and down sweeps performed at low magnetic fields. This feature, typical for superconductors has been observed with different magnitudes for the entire range of magnetic field angles in all investigated single crystals. This observation stimulated further investigations searching for possible superconductivity in $CeFe_2P_2$.

Figure 6.17(a) shows the low-field torque signal measured at 27 mK when the field aligned along [100] was swept in positive and negative directions. Due to a remanent field trapped in the magnet solenoid, the symmetry point is shifted into positive direction by 30 mT which is expected for superconducting magnets consisting of type-II superconductor.

In the course of preparing this thesis further evidence for superconductivity has been identified in low-temperature electrical-transport measurements, which have been realized by the four-probe technique, using gold wires and silver-paste contacts painted onto the sample. The experiments have been performed by utilizing a Lake Shore 700 resistance bridge.

Figure 6.17(b) shows resistance-versus-temperature data of $CeFe_2P_2$. A clear sign of superconductivity can be found in the low-temperature resistance data. On zero-field cooling, a clear drop of the sample resistance to zero has been observed. The onset of superconductivity appears at about 0.95 K and zero resistance (within resolution) is observed at about 0.65 K. This broad transition hints at some possible inhomogeneities. The magnetic-field dependence of the sample resistance at a temperature around 48 mK is shown in Fig. 6.17(c). As becomes clearly visible for the magnetic field directed along the [100] axis the normal state starts to be restored above about 0.1 T.

The next investigation supporting bulk superconductivity in $CeFe_2P_2$ has been probed by low-temperature heat-capacity measurements. Specific-heat data have been obtained by R. Beyer using a continuous relaxation-time technique at the Hochfeld-Magnetlabor Dresden. This experiment has been conducted on a Quantum Design Physical Property Measurement System.

The zero-field temperature-dependent specific heat, measured on cooling, is shown in Fig. 6.17(d). At low temperature, a clear but broad specific-heat jump of $\Delta C/T_c = 5\,\mathrm{mJ/(mol\ K^2)}$ has been observed at $T_c \approx 0.65\,K$. That makes, the bulk T_c coincident with the zero-resistance temperature.

The electronic specific heat of the normal-conducting state was estimated from a fit of the equation $C(T) = \gamma T + \beta T^3$ to the experimental result by plotting the data as $C(T)/T = \gamma + \beta T^2$, by which the data should follow a straight line with intercept γ at $T = 0$. The data between 1 and 1.7 K gave a Sommerfeld coefficient of $\gamma = 22\,\mathrm{mJ/(mol\ K^2)}$. This value is found to be close to those of other high-T_c iron-based pnictide superconductors. As an example, $\gamma = 23\,\mathrm{mJ/(mol\ K^2)}$ for $(Ba,K)Fe_2As_2$ [209] and $\gamma = 19.3\,\mathrm{mJ/(mol\ K^2)}$ for $LaFe_2P_2$ reported recently [199]. Compared to other 122 ternary phosphides

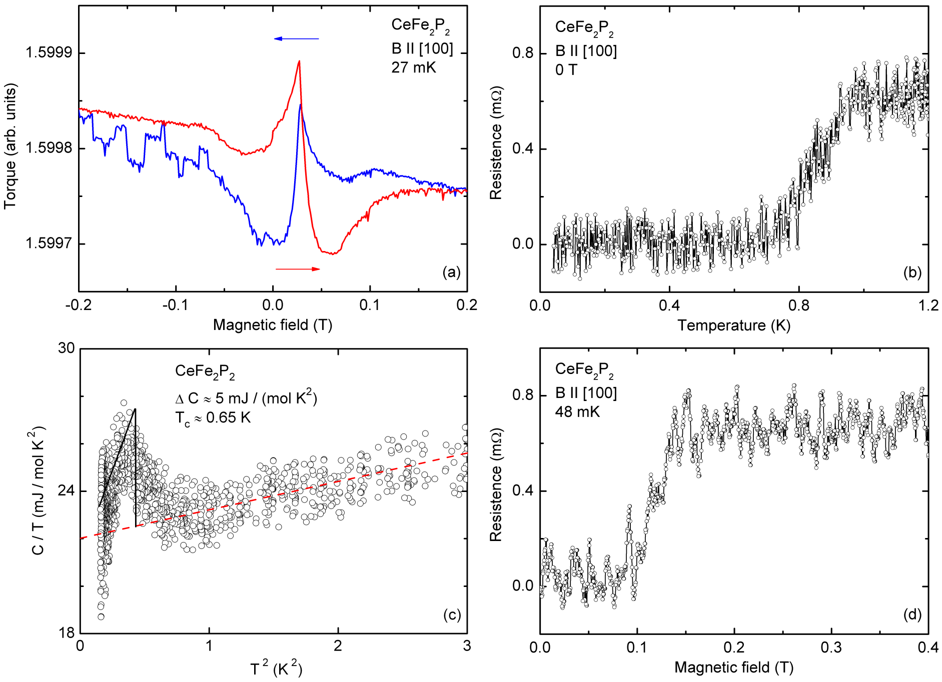

Figure 6.17.: *(a) Low-field dependence of the torque signal taken at 27 mK with the magnetic field applied parallel to the [100] axis, yielding a hysteresis loop between the up and down sweeps. The arrows indicate the field-sweep directions. (b) Temperature- and (c) magnetic-field dependence of the sample resistance for the magnetic field applied parallel to the crystallographic [100] axis. (d) Specific heat, $C(T)$, divided by temperature as a function of T^2 in zero applied field. The dashed line represents a fit to $C(T)/T = \gamma + \beta T^2$. The specific heat jump at T_c has been estimated as indicated by the black solid lines. This analysis gives the value $\Delta C/\gamma T_c = 0.23$. Experiment conducted by R. Beyer, HLD.*

($LaRu_2P_2$ with $\gamma = 11.5\,\mathrm{mJ/(mol\,K^2)}$ [199], $CaFe_2P_2$ with $\gamma = 6.5\,\mathrm{mJ/(mol\,K^2)}$ [210], $BaIr_2P_2$ with $\gamma = 9.3\,\mathrm{mJ/(mol\,K^2)}$, and $BaRh_2P_2$ with $\gamma = 9.2\,\mathrm{mJ/(mol\,K^2)}$ [211]), the γ coefficient obtained in our study is substantially larger. The γ value results in a normalized specific-heat jump at T_c of $\Delta C/\gamma T_c = 0.23$ which is significantly smaller than the BCS weak-coupling value of 1.43. This result hints at an incomplete superconducting phase.

However, the results obtained for different crystals in torque, resistance, and specific-heat experiments are consistence and point to the presence of superconductivity below 0.65 K.

6.4. Conclusions

In conclusion, comprehensive dHvA measurements of the iron-based ternary phosphides $LaFe_2P_2$ and $CeFe_2P_2$ have been performed. The results of these measurements were compared to band-structure calculations done by M. Côté and coworkers at the Université de Montréal. The Fermi-surface topology of $LaFe_2P_2$ and $CeFe_2P_2$ is clearly different in comparison to other 122 iron-based pnictides. It is well known that the Fermi surface of most 122 compounds is composed of small two-dimensional electron-like circular cylinders running along the c axis at the Brillouin zone edges, and two hole-like cylinders situated at the center of the zone [212].

Here, for $LaFe_2P_2$ and $CeFe_2P_2$ however, the hole-like Fermi surface are predicted to be either flat doughnut-like ($LaFe_2P_2$) or a large branched three-dimensional sheet at the top of the Brillouin zone ($CeFe_2P_2$). Also the electron-like sheets are predicted to be much more corrugated. In fact, this Fermi-surface topology of the investigated compounds is more three than two dimensional.

Most dHvA frequencies predicted by the band structure of $LaFe_2P_2$ slightly deviate from experimental data. However, tiny shifts of the bands assuming slightly changed electron densities can reconcile these results. Anyway, good agreement between the calculated and measured dHvA frequencies is found only for $LaFe_2P_2$. This proves the predicted Fermi-surface topology for this material to be correct. Only for one orbit some discrepancies to the predictions are found. For $CeFe_2P_2$, however, strong disagreement between calculation and experiment is found. Moreover, there are also different results for different $CeFe_2P_2$ single crystals. In two samples A and B of the first batch produced in the group of Z. Fisk at the University of California, Irvine data show no indication of a two-dimensional Fermi surface. In $CeFe_2P_2$ samples from the second batch grown in the group of C. Geibel at the Max Planck Institute for Chemical Physics of Solids, Dresden only one low frequency F_ε has been observed. This dHvA branch is common for all investigated samples and corresponds to one three-dimensional ellipsoidal Fermi surface.

The effective masses at various magnetic-field directions for both $LaFe_2P_2$ and $CeFe_2P_2$ have been extracted using the Lifshitz-Kosevich formalism. The effective masses determined for $LaFe_2P_2$ are rather small with values between 1.5 and $5.2\,m_e$. Those measured close to the [001] axis are considerably smaller than reported before. The mass-enhancement parameters have been calculated for the α_1 and α_2 orbits yielding values close to one. The effective masses determined for $CeFe_2P_2$ are ranging from 2.2 to $2.9\,m_e$.

Torque, resistance, and specific-heat measurements conducted on $CeFe_2P_2$ single crystals evidence the existence of superconductivity below $T = 0.65\,\mathrm{K}$. Above $B = 0.1\,\mathrm{T}$ aligned along the [100] direction, superconductivity is destroyed. The existence of superconductivity at ambient pressure in undoped 122 Fe-based phosphide is unique. Up to date, no report on this field has been published to our knowledge.

7. Summary

In the present work, the electronic properties of two different kinds of materials belonging to the family of strongly correlated electron systems have been investigated by employing de Haas-van Alphen measurements. For these measurements, conducted both at the HLD in Dresden using a 20-T superconducting magnet and at the LNCMI in Grenoble by use of a 35-T resistive magnet, capacitive cantilever torquemeters that could be rotated *in situ* around one axis were utilized. The obtained results were compared to band-structure calculations done in the framework of density-functional theory using the ABINIT code by M. Côté and coworkers at the Université de Montréal.

In $Ce_{1-x}Yb_xCoIn_5$, the evolution of the Fermi surface, effective masses, and quasiparticle scattering rates was systematically studied as a function of Yb substitution. The purpose of this study was to examine the transition from the heavy-fermion superconductor $CeCoIn_5$ to the Pauli paramagnet $YbCoIn_5$. For that, a set of high-quality single crystals with different Yb concentrations was investigated by de Haas-van Alphen measurements. For $x = 0.1$, the well-known Fermi surfaces of $CeCoIn_5$ ($x = 0$) that consist of nearly cylindrical Fermi surfaces and small ellipsoidal sheets change only slightly. The Fermi-surface topology starts to change drastically at $x = 0.2$ becoming more obvious for $x = 0.55$ and above. For $YbCoIn_5$ ($x = 1$), the Fermi-surface topology extracted experimentally is very similar to the calculated Fermi surfaces of other 115 compounds without $4f$ contributions to the band structure. For both $CeCoIn_5$ and $YbCoIn_5$, the angular-resolved dHvA frequencies can be very well described by conventional density-functional-theory calculations. Projection of the Bloch states onto atomic Yb-$4f$ orbitals yields a $4f$ occupation of 13.7 electrons. This is in agreement with previous experimental results indicating an intermediate Yb valence of +2.3. The heavy electron masses of $CeCoIn_5$ for $x = 0.1$ are reduced only weakly. With increasing Yb concentration, the effective masses are reduced considerably to values between 0.7 and 2.6 m_e. This observation contradicts the specific-heat results where up to $x = 0.55$ almost no change of the Sommerfeld coefficient and for higher concentrations up to $x = 0.8$ only a moderate reduction of the electronic specific heat was observed. In the presented dHvA study, however, no heavy quasiparticles for $x \geq 0.2$ have been resolved. The Dingle temperatures, which are directly proportional to the quasiparticle scattering rates, have been estimated for the samples with different x. They increase from 0.3 K for $CeCoIn_5$ over 0.7 K for $x = 0.1$ up to about 5.6 K for $x = 0.2$ and 3.8 K for $x = 0.55$. The latter high Dingle temperatures would not allow for a detection of heavy-mass orbits for $x = 0.2$ and $x = 0.55$. Finally, it can be assumed that a disorder-induced strong scattering prevents the observation of heavy quasiparticles with short mean free paths in some presumably still existing heavy-electron $4f$ bands.

As the second material class, the iron-based ternary phosphides $LaFe_2P_2$ and $CeFe_2P_2$ have been investigated by comprehensive de Haas-van Alphen measurements. The results of these measurements were compared to band-structure calculations done as well in the group of M. Côté, predicting Fermi-surface topologies that are composed of a three-dimensional hole-like part at the top of the Brillouin zone and a strongly corrugated two-dimensional electron-like cylinder at the zone edge. Good agreement between the calculated and measured dHvA frequencies was found only for $LaFe_2P_2$. However, for $CeFe_2P_2$ strong disagreement between calculation and experiment has been observed. Moreover, different $CeFe_2P_2$ single crystals reveal different experimental results. For the samples A and B from one batch, seven dHvA frequencies have been resolved, but with no indication of a two-dimensional Fermi surface. For the sample C from another batch, only one low-frequency branch with little anisotropy was identified. This dHvA branch was observed in all investigated $CeFe_2P_2$ samples. In order to reconcile the results of the dHvA measurements and density-functional-theory calculations for $CeFe_2P_2$ more work is necessary.

Definitely, this issue will be resolved in the future as larger, higher purity samples and more sophisticated calculations become available. The effective masses for both $LaFe_2P_2$ and $CeFe_2P_2$ have been extracted using the Lifshitz-Kosevich formalism. The effective masses obtained for $LaFe_2P_2$ are small with values between 1.5 and $5.2\,m_e$. The mass enhancement parameters calculated for two orbits of the electron-like cylindrical Fermi surface yield values of $\lambda \approx 1$. The effective masses determined for $CeFe_2P_2$ are ranging from 2.2 to $2.9\,m_e$. Torque, resistance, and specific-heat measurements conducted on $CeFe_2P_2$ single crystals have revealed the possible existence of superconductivity below $T = 0.65\,\mathrm{K}$. Above $B = 0.1\,\mathrm{T}$ aligned along the [100] direction, superconductivity is destroyed. Superconductivity at ambient pressure in undoped 122 Fe-based phosphide is unusual.

A. Filled skutterudite $PrPt_4Ge_{12}$

Skutterudite is the name of a $CoAs_3$-based mineral that was first extensively mined as a source of cobalt and nickel in the region of Skutterud, Norway. Compounds with the same cubic crystal structure have since been known as “skutterudites” [213]. An example of a well-formed natural skutterudite mineral is shown in Fig. A.1(a).

Binary skutterudites TX_3 are formed by a transition metal T = (Co, Rh, Ir) with pnictogens X = (P, As, Sb). For electronic reasons no binary compounds with iron, ruthenium, and osmium could be synthesized under equilibrium conditions. To stabilize the skutterudite structure with elements of the iron group or other metals it is necessary to “fill” it with electropositive elements as a third component leading to the formula MT_4X_{12} [214]. The stabilizing atoms M (can be an alkali, alkaline-earth, rare-earth or actinide metal) are situated in large isocahedral cages formed by TX_6 octahedra [Fig. A.1(b)].

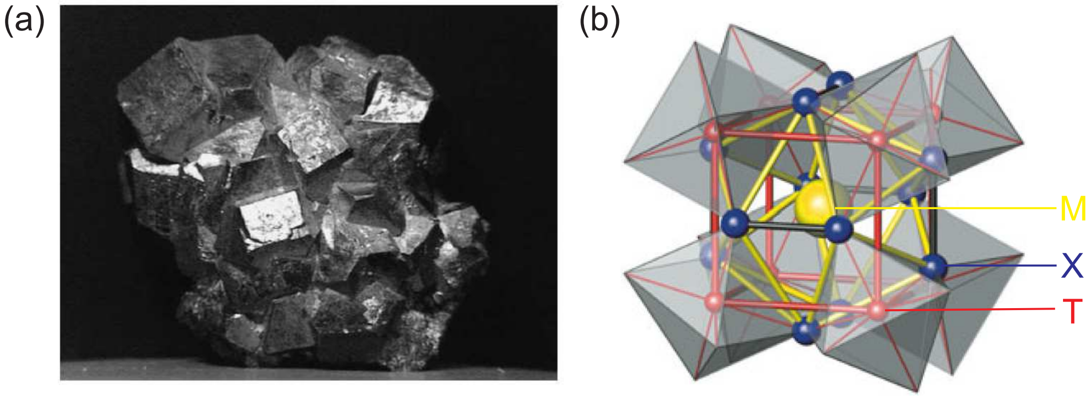

Figure A.1.: *(a) Photograph of a natural skutterudite mineral [213]. (b) Section of the crystal structure of filled skutterudites with the general formula MT_4X_{12}. The TX_6 octahedral units are shown in gray, the icosahedral void is outlined in yellow [215].*

The filled skutterutide family has attracted much attention within the past several years not only due to the fascinating variety of strongly correlated electron phenomena this class compounds can exhibit [213, 216–218], but also owing to their large potential for next generation thermoelectric materials [219–221]. The case of Pr-based filled skutterudites has generated particular interest, since it is thought that most of the peculiar features depend on the ground state and the low-lying exited state of the Pr^{3+} ion in the crystalline electric field together with the strong hybridization of the Pr $4f$ shell with the conduction electrons of the surrounding ionic cage [217, 222–224].

Very recently it has been shown[1] that the transition metal in the filled skutterutide crystal structure is not strictly limited to the elements of the iron or cobalt groups. The interest in Ge-based clathrates and the promising applications of these structures in semiconductor technologies resulted in the discovery of the new skutterutide-like class MPt_4Ge_{12} (M = Sr, Ba, La, Ce, Pr Nd, Eu) composed of germanium and, for electronic-balance reasons, platinum as a transition metal [225]. The compounds with Sr and Ba [226], Th [227, 228], and with La and Pr [225] are superconductors. These latter two have the highest T_c among the Pt-Ge framework of 8.3 and 7.9 K, respectively.

For $PrPt_4Ge_{12}$, measurements of muon-spin rotation (μSR) and specific heat have indicated that this compound is a strong-coupling superconductor characterized by the superconducting energy gap with point nodes [229]. In addition, zero- and longitudinal-field μSR experiments have shown a spontaneous magnetization with a temperature variation resembling that of the superfluid density below T_c, implying time-reversal symmetry breaking [230]. Contrary to these studies suggesting unconventional superconductivity in $PrPt_4Ge_{12}$, ^{73}Ge-nuclear quadrupole resonance (NQR) has revealed a coherence peak just below T_c, indicating that the superconductivity is accounted for in terms of conventional BCS type [231]. From the NQR data it was claimed that the results suggest not only an isotropic s-wave gap but also an anisotropic s-wave gap with point nodes. It was supposed that the high T_c of $PrPt_4Ge_{12}$ may be attributed to the large density of states at the Fermi level. To clarify the superconducting gap structure

---

[1] at the Max-Planck-Institut für Chemische Physik fester Stoffe (MPI-CPfS), Dresden

of $PrPt_4Ge_{12}$, high-resolution photoemission spectroscopy has recently been performed indicating that the two-gap model is more suitable for describing the superconducting-state spectrum than the single-isotropic or single-anisotropic-gap model [232]. This result suggests that multiband effects may possibly induce the anomalous superconducting properties of $PrPt_4Ge_{12}$. So, since electrons in the vicinity of the Fermi level are primarily responsible for superconductivity, the knowledge of the Fermi-surface properties is essential for a better understanding.

The electronic structure of $PrPt_4Ge_{12}$, grown by standard techniques [225] at the MPI-CPfS, Dresden, was examined in a combined theoretical and experimental approach. The dHvA study was realized at the HLD in magnetic fields up to 18 T employing a torque magnetometer.

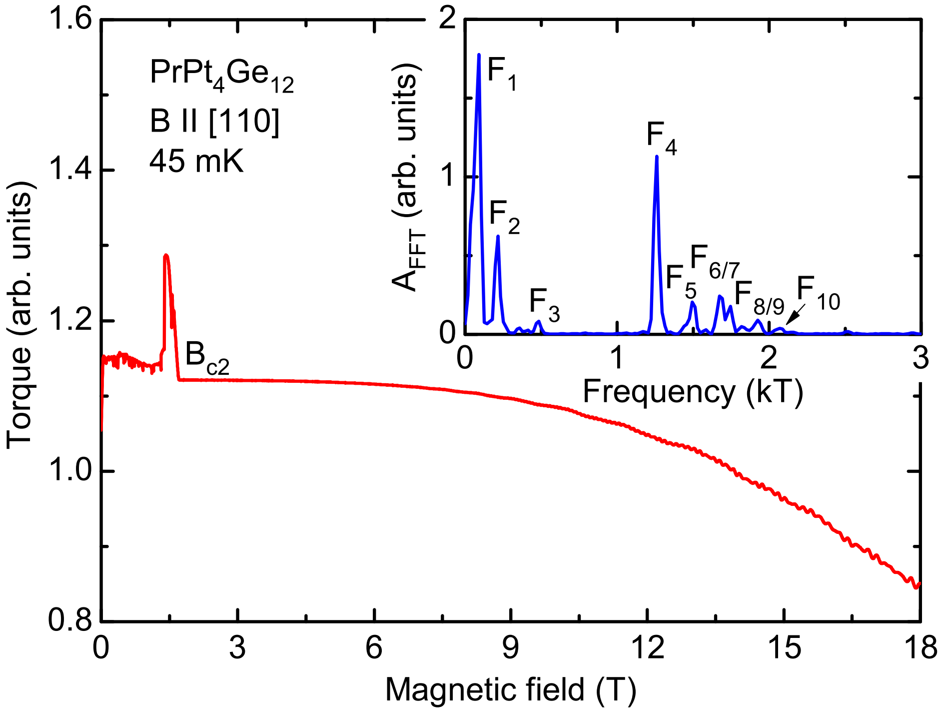

Figure A.2.: *Magnetic-torque signal of* $PrPt_4Ge_{12}$ *measured at* $B \parallel [110]$ *and* $T = 45\,mK$. *Below* B_{c2} *a clear "peak effect" [233] is observed for fields between 1 and 2 T. The inset shows the Fourier transform of the torque data between 9 and 18 T after background subtraction.*

Torque measured as a function of magnetic field, $B \parallel [110]$, up to 18 T at a temperature of about 45 mK is shown in the main panel of Fig. A.2. For fields below the upper critical field, B_{c2}, a clear "peak effect" [233] in the field range between 1 and 2 T has been observed. This low-field behavior is typical of a bulk anisotropic type-II superconductors in the vortex state, has been observed for $PrPt_4Ge_{12}$ with different magnitudes for all angles.

For magnetic fields higher than B_{c2} the background torque signal varies quadratically with B as expected for paramagnet. At magnetic fields above 7 T, in the torque signal magnetic quantum oscillations arising from the de Haas-van Alphen effect become visible. The inset of Fig. A.2 shows the Fourier spectrum obtained via fast Fourier transformation of the background-subtracted torque signal taken on the field range between 9 and 18 T. At this field angle ten characteristic frequencies [labeled as $F_1 - F_{10}$] belonging to the extremal orbits of the Fermi surface can be distinguished, as the peaks in the Fourier spectrum.

From the temperature dependence of the dHvA oscillations cyclotron effective masses for various Fermi-surface orbits of $PrPt_4Ge_{12}$ were derived. Fig. A.3(a) shows torque signals measured up to 18 T when the magnetic field was aligned along the c axis. In the superconducting state below about 1.8 T a clear hysteresis appears between the up and down sweeps

Table A.1.: dHvA frequencies and effective masses of $PrPt_4Ge_{12}$ obtained from experiment for the magnetic field in the [001] and [010] directions.

Label	F_1	F_2	F_3	F_4	F_5	F_6	F_7	F_8	F_9	F_{10}
$B \parallel [001]$										
F (kT)	0.09	0.2	0.27	1.13	1.39	1.44	1.7	1.74	1.92	3.11
m^* (m_e)	–	1.1	1.0	0.5	0.6	0.7	0.7	0.9	–	–
$B \parallel [010]$										
F (kT)	0.09	0.16	0.22	1.13	1.22	1.39	1.64	1.77	2.06	2.16
m^* (m_e)	0.7	1.4	1.1	0.7	0.8	1.05	1.2	1.3	1.5	–

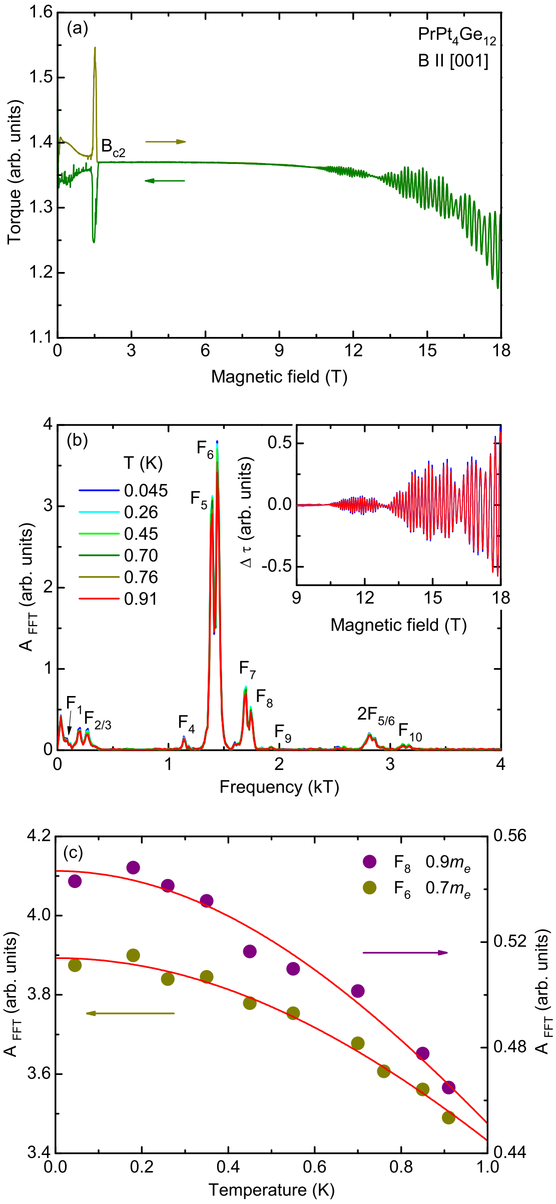

Figure A.3.: *(a) Field dependence of the torque signals recorded at* $B \parallel [001]$. *(b) Inset: oscillating signals obtained after performing a background subtraction from the torque data taken at 45 mK and 0.91 K. Main panel: thermal evolution of the dHvA spectrum after fast Fourier transformations. (c) Temperature dependence of the oscillation amplitudes shown for the frequencies* F_6 *and* F_8. *The solid lines are fits of the Lifshitz-Kosevich formula to the experimental data. Fit results in the units of free electron masses are given in the legend as well as in Table A.1.*

indicated by arrows. The quantum oscillations shown after background subtraction in the inset of Fig. A.3(b) have a node at 13 T caused by two closely-spaced dHvA frequencies. Similar beating in the quantum-oscillatory magnetizations has been observed in the paramagnetic-metal phase of the antiferromagnetic filled skutterudite $PrOs_4As_{12}$ [234], ferromagnetic filled skutterudite $NdFe_4P_{12}$ [235] and other lanthanides [236]. In these compounds beating has been attributed to the splitting of the Fermi surface into spin-up and spin-down components caused by direct exchange interactions. However, in the case of $PrPt_4Ge_{12}$ the origin of beats most probably is different. Effective masses for each dHvA frequency were evaluated independently, using a wide Fourier window for analysis to ensure that two separate frequency components are resolved.

As is evident in Table A.1, all effective masses determined in this study for $PrPt_4Ge_{12}$ are well below 1.5 m_e which clearly confirms that this compound is not a heavy-fermion superconductor.

Figure A.4 shows the angular dependence of all observed dHvA frequencies of $PrPt_4Ge_{12}$ for rotations of the sample in the Θ_{1-10} and Θ_{010} planes. In order to achieve better visibility the low-frequency range (below 0.9 kT) and the high-frequency range (above 0.9 kT) are shown separately. Electronic band-structure calculations performed in the group of H. Rosner at the MPI-CPfS, Dresden within the local-density approximation of the density-functional theory were employed using the full-potential local-orbital code FPLO version 5.00-19.19 [144]. In the full-relativistic calculations, the exchange and correlation potential of Perdew and Wang was used [140].

As is evident in Fig. A.5, $PrPt_4Ge_{12}$ has a very elaborated electronic band structure with several Fermi surfaces built by six different bands. The Fermi surface is clearly three-dimensional with very little anisotropy. From these Fermi surfaces extremal cross-sections have been calculated and plotted in Fig.A.4 with solid lines. However, so far it is difficult to assign the results of density-functional-theory calculations to the experimentally determined dHvA frequency branches. Further experimental and theoretical efforts are required in order to better understand the challenging electronic properties of this compound.

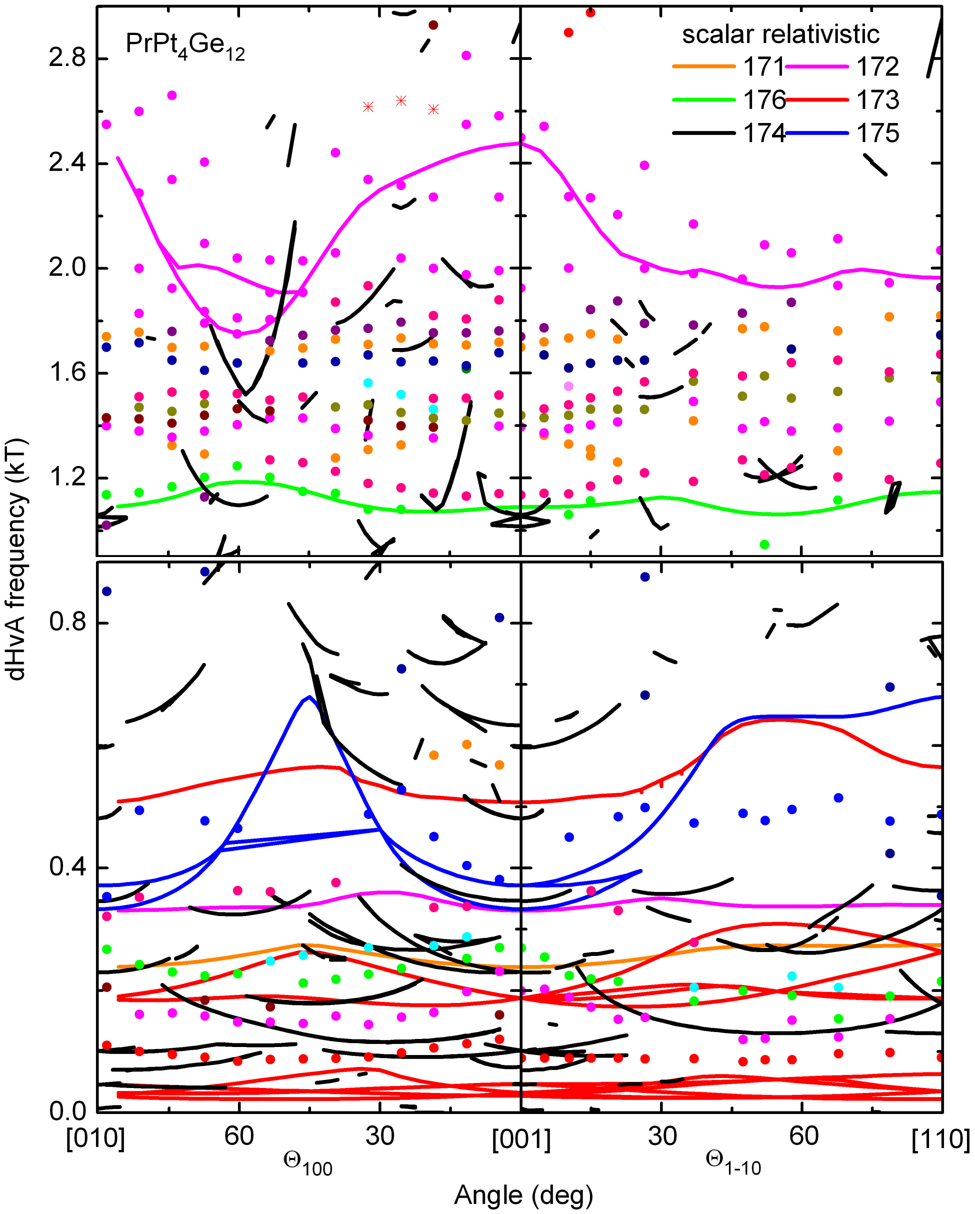

Figure A.4.: *Angular dependence of the dHvA frequencies of PrPt$_4$Ge$_{12}$. In the upper panel the high-frequency range (above 0.9 kT) and in the lower panel the low-frequency range (below 0.9 kT) is shown. The dots display the experimental data and the solid lines represent the calculated frequencies.*

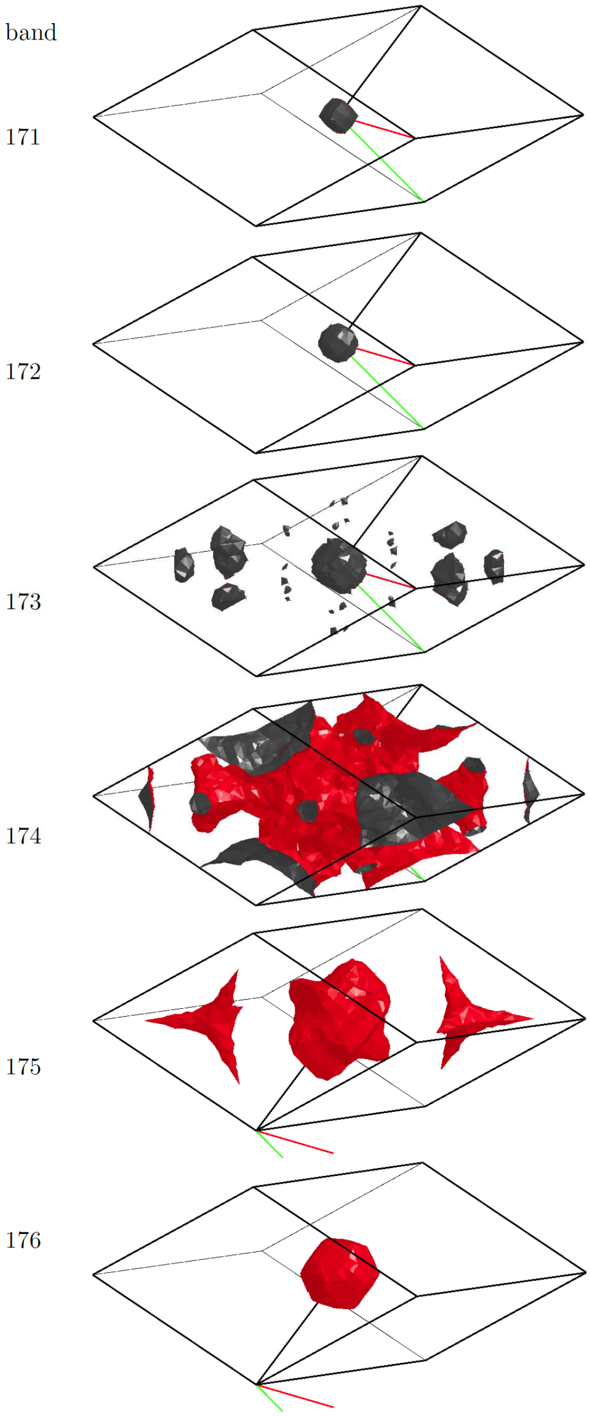

Figure A.5.: *Fermi surfaces of $PrPt_4Ge_{12}$ calculated using the FPLO code.*

Bibliography

[1] S.S Saxena and P.B. Littlewood. Strongly correlated electron systems. J. Phys.: Condens. Matter, **24** 290301, 2012.

[2] S. Watanabe and K. Miyake. New universality class of quantum criticality in Ce- and Yb-based heavy fermions. J. Phys.: Condens. Matter, **24** 294208, 2012.

[3] H. Kamerlingh Onnes. Further experiments with liquid helium. C. On the change of electric resistance of pure metals at very low temperatures, etc. IV. The resistance of pure mercury at helium temperatures. Commun. Phys. Lab. Univ. Leiden, 120b, 122b, 124c, 1911.

[4] L.N. Cooper. Bound Electron Pairs in a Degenerate Fermi Gas. Phys. Rev., **104** 1189, 1956.

[5] J. Bardeen, L.N. Cooper, J.R. Schrieffer. Theory of superconductivity. Phys. Rev. B, **108** 1175, 1957.

[6] F. Steglich, J. Aarts, C.D. Bredl, W. Lieke, D. Meschede, W. Franz and H. Schäfer. Superconductivity in the Presence of Strong Pauli Paramagnetism: $CeCu_2Si_2$. Phys. Rev. Lett., **43** 1892, 1979.

[7] I.I. Mazin. Superconductivity gets an iron boost. Nature, **464** 183-186, 2010.

[8] M. Tinkham, M.R. Beasley, D.C. Larbalestier, A.F. Clark, D.K. Finnemore: Workshop on Problems in Superconductivity, Copper Mountain, Colorado, August 1983, p. 12.

[9] J.G. Bednorz and K.A. Müller. Possible High T_c Superconductivity in the Ba - La - Cu - 0 System. Z. Phys. B - Condensed Matter, **64** 189, (1986).

[10] K. Takada, H. Sakurai, E. Takayama-Muromachi, F. Izumi, R.A. Dilanian, T. Sasaki. Superconductivity in two-dimensional CuO_2 layers. Nature, **53** 422, 2003.

[11] G.P. Meisner. Superconductivity and magnetic order in ternary rare earth metal phosphides. Physics B, **108** 763, 1981.

[12] Y. Maeno, H. Hashimoto, K. Yoshida, S. Nishizaki, T. Fujita, J.G. Bednorz, and F. Lichtenberg. Superconductivity in a layered perovskite without copper. Nature, **372** 532, 1994.

[13] K. Ishida, H. Mukuda, Y. Kitaoka, K. Asayama, Z.Q. Mao, Y. Mori, and Y. Maeno. Spin-triplet superconductivity in Sr_2RuO_4 identified by ^{17}O Knight shift. Nature, **396** 658, 1998.

[14] Y. Kamihara, H. Hiramatsu, M. Hirano, R. Kawamura, H. Yanagi, T. Kamiya, and H. Hosono. Iron-Based Layered Superconductor: LaOFeP. J. Am. Chem. Soc., **128** 10012, 2006.

[15] Y. Kamihara, T. Watanabe, M. Hirano,and H. Hosono. Iron-Based Layered Superconductor La[$O_{1-x}F_x$]FeAs (x = 0.05-0.12) with $T_c = 26\,K$. J. Am. Chem. Soc., **130** 3296, 2008.

[16] H. Takahashi, K. Igawa, K. Arii, Y. Kamihara, M. Hirano, and H. Hosono. Superconductivity at 43 K in an iron-based layered compound $LaO_{1-x}F_xFeAs$. Nature, **453** 376, 2008.

[17] G.F. Chen, Z. Li, D. Wu, G. Li, W.Z. Hu, J. Dong, P. Zheng, J.L. Luo, and N.L. Wang. Superconductivity at 41 K and Its Competition with Spin-Density-Wave Instability in Layered $CeO_{1-x}F_xFeAs$. Phys. Rev. Lett., **100** 247002, 2008.

[18] H.H. Wen, G. Mu, L. Fang, H. Yang, X.Y. Zhu. Superconductivity at 25 K in hole-doped ($La_{1-x}Sr_x$)OFeAs. Euro. Phys. Lett., **82** 17009, 2008.

[19] X.H. Chen, T. Wu, G. Wu, R.H. Liu, H. Chen, D.F. Fang. Superconductivity at 43 K in $SmFeAsO_{1-x}F_x$. Nature, **453** 761, 2008.

[20] Z.-A. Ren, J. Yang, W. Lu, W. Yi, X.-L. Shen, Z.-G. Li, G.-C. Che, X.-L. Dong, L.-L. Sun, F. Zhou, Z.-X. Zhao. Superconductivity in iron-based F-doped layered quaternary compound Nd[$O_{1-x}F_x$]FeAs. Europhys. Lett., **82** 57002, 2008.

[21] Z.-A. Ren, J. Yang, W. Lu, W. Yi, X.-L. Shen, Z.-G. Li, G.-C. Che, X.-L. Dong, L.-L. Sun, F. Zhou, Z.-X. Zhao. Superconductivity at 52 K in iron-based F-doped layered quaternary compound Pr[$O_{1-x}F_x$]FeAs. arXiv:0803.4283.

[22] P. Cheng, L. Fang, H. Yang, X. Zhu, G. Mu, H. Luo, Z. Wang, H.-H. Wen. Superconductivity at 36 K in Gadolinium-arsenide Oxides $GdO_{1-x}F_xFeAs$. arXiv:0804.0835.

[23] G.F. Chen, Z. Li, D. Wu, J. Dong, G. Li, W.Z. Hu, P. Zheng, J.L. Luo, N.L. Wang. Element substitution effect in transition metal oxypnictide $Re(O_{1-x}F_x)T$As (Re = rare earth, T = transition metal). arXiv:0803.4384v1.

[24] F.C. Hsu, J.Y. Luo, K.W. Yeh, T.K. Chen, T.W. Huang, P.M. Wu, Y.C. Lee, Y.L. Huang, Y. Y. Chu, D.C. Yan, and M.K. Wu. Superconductivity in the PbO-type structure α-FeSe. Proc. Natl. Acad. Sci., **105** 14262, 2008.

[25] M.H. Fang, H.M. Pham, B. Qian, T.J. Liu, E.K. Vehstedt, Y. Liu, L. Spinu, and Z.Q. Mao. Superconductivity close to magnetic instability in Fe($Se_{1-x}Te_x$)$_{0.82}$. Phys. Rev. B, **78** 224503, 2008.

[26] J.H. Tapp, Z. Tang, B. Lv, K. Sasmal, B. Lorenz, P.C.W. Chu, and A.M. Guloy. LiFeAs: An intrinsic FeAs-based superconductor with $T_c = 18\,\mathrm{K}$. Phys. Rev. B, **78** 060505, 2008.

[27] X.C. Wang, Q.Q. Liu, Y.X. Lv, W.B. Gao, L.X. Yang, R.C. Yu, F.Y. Li, C.Q. Jin. The superconductivity at 18 K in LiFeAs system. Solid. State. Commun., **148** 538-540, 2008.

[28] D.R. Parker, M.J. Pitcher, P.J. Baker, I. Franke, T. Lancaster, S.J. Blundell, and S.J. Clarke. Structure, antiferromagnetism and superconductivity of the layered iron arsenide NaFeAs. Chem. Commun., **16** 2189-2191, 2009.

[29] M. Rotter, M. Tegel, and D. Johrendt. Superconductivity at 38 K in the Iron Arsenide $Ba_{1-x}K_xFe_2As_2$. Phys. Rev. Lett., **101** 107006, 2008.

[30] A.S. Sefat, R. Jin, M.A. McGuire, B.C. Sales, D.J. Singh, and D. Mandrus. Superconductivity at 22 K in Co-Doped $BaFe_2As_2$ Crystals. Phys. Rev. Lett., **101** 117004, 2008.

[31] X. Zhu, F. Han, G. Mu, B. Zeng, P. Cheng, B. Shen, and H.-H. Wen. $Sr_3Sc_2Fe_2As_2O_5$ as a possible parent compound for FeAs-based superconductors. Phys. Rev. B, **79** 024516, 2009.

[32] X. Zhu, F. Han, G. Mu, P. Cheng, B. Zeng, and H.-H. Wen. Transition of stoichiometric Sr_2VO_3FeAs to a superconducting state at 37.2 K. Phys. Rev. B, **79** 220512, 2009.

[33] C.W. Chu. High-temperature superconductivity: Alive and kicking. Nat. Phys., **5** 787, 2009.

[34] I.I. Mazin, D.J. Singh, M.D. Johannes, and M.H. Du. Unconventional superconductivity with a Sign Reversal in the Order Parameter of $LaFeAsO_{1-x}F_x$. Phys. Rev. Lett., **101** 057003, 2008.

[35] I.I. Mazin, and J. Schmalian. Pairing symmetry and pairing state in ferropnictides: Theoretical overview. Physica C, **469** 614, 2009.

[36] K. Kuroki, S. Onari, R. Arita, H. Usui, Y. Tanaka, H. Kontani, and H. Aoki. Unconventional Pairing Originating from the Disconnected Fermi Surfaces of Superconducting $LaFeAsO_{1-x}F_x$. Phys. Rev. Lett., **101** 087004, 2008.

[37] F. Krüger, S. Kumar, J. Zaanen, and J. van den Brink. Spin-orbital frustrations and anomalous metallic state in iron-pnictide superconductors. Phys. Rev. B, **79** 054504, 2009.

[38] W. Lv, J. Wu, and P. Phillips. Orbital ordering induces structural phase transition and the resistivity anomaly in iron pnictides. Phys. Rev. B, **80** 224506, 2009.

[39] C.-C. Lee, W.-G. Yin, and W. Ku. Ferro-Orbital Order and Strong Magnetic Anisotropy in the Parent Compounds of Iron-Pnictide Superconductors. Phys. Rev. Lett., **103** 267001, 2009.

[40] J. Zhang, R. Sknepnek, R.M. Fernandes, and J. Schmalian. Orbital coupling and superconductivity in the iron pnictides. Phys. Rev. B, **79** 220502, 2009.

[41] H. Kontani and S. Onari. Orbital-Fluctuation-Mediated Superconductivity in Iron Pnictides: Analysis of the Five-Orbital Hubbard-Holstein Model. Phys. Rev. Lett., **104** 157001, 2010.

[42] Y. Yanagi and Y. Yamakawa. Two types of s-wave pairing due to magnetic and orbital fluctuations in the two-dimensional 16-band d-p model for iron-based superconductors. Phys. Rev. B, **81** 054518, 2010.

[43] T. Saito, S. Onari, and H. Kontani. Orbital fluctuation theory in iron pnictides: Effects of As-Fe-As bond angle, isotope substitution, and Z^2-orbital pocket on superconductivity. Phys. Rev. B, **82** 144510, 2010.

[44] T.D. Stanescu, V. Galitski, and S. Das Sarma. Orbital fluctuation mechanism for superconductivity in iron-based compounds. Phys. Rev. B, **78** 195114, 2008.

[45] M. Daghofer, A. Nicholson, A. Moreo, and E. Dagotto. Three orbital model for the iron-based superconductors. Phys. Rev. B, **81** 014511 2010.

[46] T. Hanaguri, S. Niitaka, K. Kuroki, H. Takagi. Unconventional s-Wave Superconductivity in Fe(Se,Te). Science, **328** 474, 2010.

[47] A.D. Christianson, E.A. Goremychkin, R. Osborn, S. Rosenkranz, M.D. Lumsden, C.D. Malliakas, I.S. Todorov, H. Claus, D.Y. Chung, M.G. Kanatzidis, R.I. Bewley, and T. Guidi. Unconventional superconductivity in $Ba_{0.6}K_{0.4}Fe_2As_2$ from inelastic neutron scattering. Nature, **456** 930, 2008.

[48] M. Sato, Y. Kobayashi, S. Chul Lee, H. Takahashi, E. Satomi, and Y. Miura. Studies on Effects of Impurity Doping and NMR Measurements of La 1111 and/or Nd 1111 Fe-Pnictide Superconductors. J. Phys. Soc. Jpn., **79** 014710, 2010.

[49] T. Shimojima, F. Sakaguchi, K. Ishizaka, Y. Ishida, T. Kiss, M. Okawa, T. Togashi, C.-T. Chen, S. Watanabe, M. Arita, K. Shimada, H. Namatame, M. Taniguchi, K. Ohgushi, S. Kasahara, T. Terashima, T. Shibauchi, Y. Matsuda, A. Chainani, S. Shin. Orbital-Independent Superconducting Gaps in Iron Pnictides. Science, **332** 564, 2011.

[50] S. Nandi, M.G. Kim, A. Kreyssig, R.M. Fernandes, D.K. Pratt, A. Thaler, N. Ni, S.L. Bud'ko, P.C. Canfield, J. Schmalian, R.J. McQueeney, and A.I. Goldman. Anomalous Suppression of the Orthorhombic Lattice Distortion in Superconducting $Ba(Fe_{1-x}Co_x)_2As_2$ Single Crystals. Phys. Rev. Lett., **104** 057006, 2010.

[51] S.-H. Lee, G. Xu, W. Ku, J.S. Wen, C.C. Lee, N. Katayama, Z.J. Xu, S. Ji, Z.W. Lin, G.D. Gu, H.-B. Yang, P.D. Johnson, Z.-H. Pan, T. Valla, M. Fujita, T.J. Sato, S. Chang, K. Yamada, and J.M. Tranquada. Coupling of spin and orbital excitations in the iron-based superconductor $FeSe_{0.5}Te_{0.5}$. Phys. Rev. B, **81** 220502, 2010.

[52] M. Daghofer, Q.-L. Luo, R. Yu, D.X. Yao, A. Moreo, and E. Dagotto. Orbital-weight redistribution triggered by spin order in the pnictides. Phys. Rev. B, **81** 180514, 2010.

[53] P. Fulde, R.A. Ferrell. Superconductivity in a Strong Spin-Exchange Field. Phys. Rev., **135** A550, 1964.

[54] A.I. Larkin and Y.N. Ovchinnikov. Inhomogeneous of superconductors. Sov. Phys. JETP, **20** 762, 1965.

[55] Y. Matsuda and H. Shimahara. Fulde-Ferrell-Larkin-Ovchinnikov State in Heavy Fermion Superconductors. J. Phys. Soc. Jpn., **76**: 051005, 2007.

[56] A. Bianchi, R. Movshovich, C. Capan, P.G. Pagliuso, and J.L. Sarrao. Possible Fulde-Ferrell-Larkin-Ovchinnikov Superconducting State in $CeCoIn_5$. Phys. Rev. Lett., **91** 187004, 2003.

[57] K. Gloos, R. Modler, H. Schimanski, C.D. Bredl, C. Geibel, F. Steglich, A.I. Buzdin, N. Sato, and T. Komatsubara. Possible formation of a nonuniform superconducting state in the heavy-fermion compound UPd_2Al_3. Phys. Rev. Lett., **70** 501-504, 1993.

[58] H. Shimahara. Theory of the Fulde-Ferrell-Larkin-Ovchinnikov State and Application to Quasi-Low-Dimensional Organic Superconductors. A.G. Lebed (ed.): The Physics of Organic Superconductors and Conductors, Springer, Berlin, 2008.

[59] G. Zwicknagl and J. Wosnitza. BCS: *50 years* edited by L.N. Cooper and D. Feldman (World Scientific, Singapore, 2011) p. 337-371; Int. J. Mod. Phys. B, **24** 3915, 2010.

[60] A.K. Clogston. Upper limit for the critical field in hard superconductors. Phys. Rev. Lett., **9** 266, 1962.

[61] K. Maki and T. Tsuneto. Pauli Paramagnetism and Superconducting State. Prog. Theor. Phys., **31** 945, 1964.

[62] L.W. Gruenberg and L. Gunther. Fulde-Ferell effect in type-II superconductors. Phys. Rev. Lett., **16** 996, 1966.

[63] R. Lortz, Y. Wang, A. Demuer, P.H.M. Böttger, B. Bergk, G. Zwicknagl, Y. Nakazawa, and J. Wosnitza. Calorimetric Evidence for a Fulde-Ferrell-Larkin-Ovchinnikov Superconducting State in the Layered Organic Superconductor κ-$(BEDT\text{-}TTF)_2Cu(NCS)_2$. Phys. Rev. Lett., **99** 187002, 2007.

[64] B. Bergk, A. Demuer, I. Sheikin, Y. Wang, J. Wosnitza, Y. Nakazawa, and R. Lortz. Magnetic torque evidence for the Fulde-Ferrell-Larkin-Ovchinnikov state in the layered organic superconductor κ-(BEDT-TTF)$_2$Cu(NCS)$_2$. Phys. Rev. B, **83** 064506, 2011.

[65] R. Beyer, B. Bergk, S. Yasin, J.A. Schlueter, and J. Wosnitza. Angle-Dependent Evolution of the Fulde-Ferrell-Larkin-Ovchinnikov State in an Organic Superconductor. Phys. Rev. Lett., **109** 027003, 2012.

[66] K. Andres and J.E. Graebner. $4f$-Virtual-Bound-State Formation in CeAl$_3$ at Low Temperatures. Phys. Rev. Lett., **35** 1779, 1975.

[67] K.H. Bennemann, and J.B. Ketterson. Superconductivity. Bd. 1-2. Springer Verlag Berlin Heidelberg, 762, 2008.

[68] S. Doniach. The Kondo lattice and weak antiferromagnetism. Physica B+C, vol. **91** 231-234, 1977.

[69] Y. Onuki, R. Settai, K. Sugiyama, T. Takeuchi, T.C. Kobayashi, Y. Haga, and E. Yamamoto. Recent Advances in the Magnetism and Superconductivity of Heavy Fermion Systems. J. Phys. Soc. Jpn., **73** 769-787, 2004.

[70] Z. Fisk, D.W. Hess, C.J. Pethick, D. Pines, J.L. Smith, J.D. Thompson, J.O. Willis. Heavy-electron metals - New highly correlated states of matter. Science, **239** 33, 1988.

[71] H.v. Löhneysen, T. Pietrus, G. Portisch, H.G. Schlager, A. Schröder, M. Sieck, and T. Trappmann. Non-Fermi-liquid behavior in a heavy-fermion alloy at a magnetic instability. Phys. Rev. Lett., **72** 3262, 1994.

[72] L.D. Landau. The Theory of a Fermi Liquid. Zh. Eksp. Teor. Fiz., **30** 1058, 1956. [Sov. Phys. JETP, **3** 920, 1957].

[73] P. Nozières. Theory of Interacting Fermi Systems. (New York: Benjamin), 1964.

[74] D. Pines and P. Nozières. The Theory of Quantum Liquids vol 1. (New York: Benjamin), 1966.

[75] P. Coleman, C. Pepin, Q. Si, and R. Ramazashvili. How do Fermi liquids get heavy and die? J. Phys.: Condens. Matter, **13** 723, 2001.

[76] A.J. Schofield. Non-fermi liquids. Contemp. Phys., **40** 95, 1999.

[77] L. Onsager. Interpretation of the de Haas-van Alphen Effect. Phil. Mag., **43** 1006, 1952.

[78] A.V. Gold. Electrons in metals. Solid state Physics. J.F. Cohran and R.R. Haering. New York: Gordon and Breach, 1968.

[79] M. Springford. Electrons at the Fermi Surface. Cambridge University Press, 1980.

[80] D. Shoenberg. Magnetic oscillations in metals. Cambridge University Press, 1984.

[81] W.J. de Haas and P.M. van Alphen. Commun. Phys. Lab. Univ. Leiden, **21** 215, 1930; Proc. R. Acad. Sci. Amsterdam, **33** 1106, 1930.

[82] L.D. Landau. Paramagnetism of metals. Z. Phys., **64** 629, 1930.

[83] I.M. Lifshitz. Unpublished lecture, 1950.

[84] I.M. Lifshitz and A.M. Kosevich. Zh. Eksp. Teor. Fiz., **29** 730, 1955. [Sov. Phys. JETP, **2** 636, 1956].

[85] R.B. Dingle. Some Magnetic Properties of Metals. II. The Influence of Collisions on the Magnetic Behaviour of Large Systems. Proc. Roy. Soc. A, **211**, 517, 1952.

[86] K. Yamaji. On the angle dependence of the magnetoresistance in quasi-two-dimensional organic superconductors. J. Phys. Soc. Jpn., **58** 1520, 1989.

[87] C. Bergemann, A.P. Mackenzie, S.R. Julian, D. Forsythe, and E. Ohmichi. Quasi-two-dimensional fermi liquid properties of the unconventional superconductor Sr_2RuO_4. Adv. Phys., **52** 7, 2003.

[88] J.S. Brooks, M.J. Naughton, Y.P. Ma, P.M. Chaikin, and R.V. Chamberlin. Small sample magnetometers for simultaneous magnetic and resistive measurements at low temperatures and high magnetic fields. Rev. Sci. Instrum., **58** 117, 1987.

[89] A. Polyakov, O. Ignatchik, B. Bergk, K. Götze, A.D. Bianchi, S. Blackburn, B. Prévost, G. Seyfarth, M. Côté, D. Hurt, C. Capan, Z. Fisk, R.G. Goodrich, I. Sheikin, M. Richter, and J. Wosnitza. Fermi-surface evolution in Yb-substituted $CeCoIn_5$. Phys. Rev. B, **85** 245119, 2012.

[90] Q. Si and F. Steglich. Heavy Fermions and Quantum Phase Transitions. Science, **329** 1161, 2010.

[91] H.v. Löhneysen, A. Rosch, M. Vojta, and P. Wölfle . Fermi-liquid instabilities at magnetic quantum phase transitions. Rev. Mod. Phys., **79** 1015, 2007.

[92] C. Petrovich, R. Movshovich, M. Jaime, P.G. Pagliuso, M.F. Hundley, J.L. Sarrao, Z. Fisk, and J.D. Thompson. A new heavy-fermion superconductor $CeIrIn_5$: A relative of the cuprates? Europhys. Lett., **53** 354, 2001.

[93] C. Petrovich, P.G. Pagliuso, M.F. Hundley, R. Movshovich, J.L. Sarrao, J.D. Thomson. Z. Fisk, and P. Monthoux. Heavy-fermion superconductivity in $CeCoIn_5$. J. Phys.: Condens. Matter, **13** 337, 2001.

[94] R. Movshovich, M. Jaime, J.D. Thompson, C. Petrovic, Z. Fisk, P.G. Pagliuso, and J.L. Sarrao. Unconventional Superconductivity in $CeIrIn_5$ and $CeCoIn_5$: Specific Heat and Thermal Conductivity Studies. Phys. Rev. Lett., **86** 5152, 2001.

[95] C. Capan, G. Seyfarth, D. Hurt, B. Prevost, S. Roorda, A.D. Bianchi, and Z. Fisk. Wilson ratio in Yb-substituted $CeCoIn_5$. Europhys. Lett., **92** 47004, 2010.

[96] Y. Kohori, Y. Y. Yamato, Y. Iwamoto, T. Kohara, E.D. Bauer, M.B. Maple, and J.L. Sarrao. NMR and NQR studies of the heavy fermion superconductors CeTIn$_5$ (T=Co and Ir). Phys. Rev. B, **64** 134526, 2001.

[97] N.J. Curro, B. Simovic, P.C. Hammel, P.G. Pagliuso, J.L. Sarrao, J.D. Thompson, G.B. Martins. Anomalous NMR magnetic shifts in CeCoIn$_5$. Phys. Rev. B, **64** 180514, 2001.

[98] K. Izawa, H. Yamaguchi, Matsuda, Yuji, H. Shishido, R. Settai, and Y. Onuki. Angular Position of Nodes in the Superconducting Gap of Quasi-2D Heavy-Fermion Superconductor CeCoIn$_5$. Phys. Rev. Lett., **87** 057002, 2001.

[99] D. Hall, E.C. Palm, T.P. Murphy, S.W. Tozer, Z. Fisk, U. Alver, R.G. Goodrich, J.L. Sarrao, P.G. Pagliuso, and T. Ebihara. Fermi surface of the heavy-fermion superconductor CeCoIn5: The de Haas-van Alphen effect in the normal state. Phys. Rev. B, **64** 212508, 2001.

[100] R. Settai, H. Shishido, S. Ikeda, Y. Murakawa, M. Nakashima, D. Aoki, Y. Haga, H. Harima, and Y. Onuki. Quasi-two-dimensional Fermi surfaces and the de Haas-van Alphen oscillation in both the normal and superconducting mixed states of CeCoIn$_5$. J. Phys.: Condens. Matter, **13** 627, 2001.

[101] A. McCollam, S.R. Julian, P.M.C. Rourke, D. Aoki, and J. Flouquet. Anomalous de Haas-van Alphen Oscillations in CeCoIn$_5$. Phys. Rev. Lett., **94** 186401, 2005.

[102] A. Bianchi, R. Movshovich, N. Oeschler, P. Gegenwart, F. Steglich, J.D. Thompson, P.G. Pagliuso, and J.L. Sarrao. First-Order Superconducting Phase Transition in CeCoIn$_5$. Phys. Rev. Lett., **89** 137002, 2002.

[103] M. Kenzelmann, S. Gerber, N. Egetenmeyer, J.L. Gavilano, T. Strassle, A.D. Bianchi, E. Ressouche, R. Movshovich, E.D. Bauer, J.L. Sarrao, and J.D. Thompson. Evidence for a Magnetically Driven Superconducting Q Phase of CeCoIn$_5$. Phys. Rev. Lett., **104** 127001, 2010.

[104] H.A. Radovan, N.A. Fortune, T.P. Murphy, S.T. Hannahs, E.C. Palm, S.W. Tozer, and D. Hall. Magnetic enhancement of superconductivity from electron spin domains. Nature, **425** 51, 2003.

[105] C. Capan, A. Bianchi, R. Movshovich, A.D. Christianson, A. Malinowski, M.F. Hundley, A. Lacerda, P.G. Pagliuso, J.L. Sarrao. Anisotropy of thermal conductivity and possible signature of the Fulde-Ferrell-Larkin-Ovchinnikov state in $CeCoIn_5$. Phys. Rev. B, **70** 134513, 2003.

[106] C. Martin, C.C. Agosta, S.W. Tozer, H.A. Radovan, E.C. Palm, T.P. Murphy, and J.L. Sarrao. Evidence for the Fulde-Ferrell-Larkin-Ovchinnikov state in CeCoIn$_5$ from penetration depth measurements. Phys. Rev. B, **71** 020503, 2005.

[107] K. Kumagai, M. Saitoh, T. Oyaizu, Y. Furukawa, S. Takashima, M. Nohara, H. Takagi, and Y. Matsuda. Fulde-Ferrell-Larkin-Ovchinnikov State in a Perpendicular Field of Quasi-Two-Dimensional $CeCoIn_5$. Phys. Rev. Lett., **97** 227002, 2006.

[108] V.F. Correa, T.P. Murphy, C. Martin, K.M. Purcell, E.C. Palm, G.M. Schmiedeshoff, J.C. Cooley, and S.W. Tozer. Magnetic-Field-Induced Lattice Anomaly inside the Superconducting State of $CeCoIn_5$: Anisotropic Evidence of the Possible Fulde-Ferrell-Larkin-Ovchinnikov State. Phys. Rev. Lett., **98** 087001, 2007.

[109] B.-L. Young, R.R. Urbano, N.J. Curro, J.D. Thompson, J.L. Sarrao, A.B. Vorontsov, and M.J. Graf. Microscopic Evidence for Field-Induced Magnetism in $CeCoIn_5$. Phys. Rev. Lett., **98** 036402, 2007.

[110] M. Kenzelmann, T. Strassle, C. Niedermayer, M. Sigrist, B. Padmanabhan, M. Zolliker, A.D. Bianchi, R. Movshovich, E.D. Bauer, J.L. Sarrao, J.D. Thompson. Coupled Superconducting and Magnetic Order in $CeCoIn_5$. Science, **321** 1652, 2008.

[111] E. Blackburn, P. Das, M.R. Eskildsen, E.M. Forgan, M. Laver, C. Niedermayer, C. Petrovic, and J.S. White. Exploring the Fragile Antiferromagnetic Superconducting Phase in $CeCoIn_5$. Phys. Rev. Lett., **105** 187001, 2010.

[112] J. Spehling, R.H. Heffner, J.E. Sonier, N. Curro, C.H. Wang, B. Hitti, G. Morris, E.D. Bauer, J.L. Sarrao, F.J. Litterst, and H.-H. Klauss. Field-Induced Coupled Superconductivity and Spin Density Wave Order in the Heavy Fermion Compound $CeCoIn_5$. Phys. Rev. Lett., **103** 237003, 2009.

[113] Y. Kato, C.D. Batista, and I. Vekhter. Antiferromagnetic Order in Pauli-Limited Unconventional Superconductors. Phys. Rev. Lett., **107** 096401, 2011.

[114] G. Koutroulakis, M.D. Stewart, Jr., V.F. Mitrović, M. Horvatić, C. Berthier, G. Lapertot, and J. Flouquet. Field Evolution of Coexisting Superconducting and Magnetic Orders in $CeCoIn_5$. Phys. Rev. Lett., **104** 087001, 2010.

[115] A. Bianchi, R. Movshovich, I. Vekhter, P. G. Pagliuso, and J. L. Sarrao. Avoided Antiferromagnetic Order and Quantum Critical Point in $CeCoIn_5$ Phys. Rev. Lett., **91** 257001, 2003.

[116] J. Paglione, M.A. Tanatar, D.G. Hawthorn, E. Boaknin, R.W. Hill, F. Ronning, M. Sutherland, L. Taillefer, C. Petrovic, and P.C. Canfield. Field-Induced Quantum Critical Point in $CeCoIn_5$. Phys. Rev. Lett., **91** 246405, 2003.

[117] S. Zaum, K. Grube, R. Schäfer, E.D. Bauer, J.D. Thompson, and H.v. Löhneysen. Towards the Identification of a Quantum Critical Line in the (p, B) Phase Diagram of $CeCoIn_5$ with Thermal-Expansion Measurements. Phys. Rev. Lett., **106** 087003, 2011.

[118] L. Howald, G. Seyfarth, G. Knebel, G. Lapertot, D. Aoki, and J.-P. Brison. Behavior of the Quantum Critical Point and the Fermi-Liquid Domain in the Heavy Fermion Superconductor $CeCoIn_5$ Studied by Resistivity. J. Phys. Soc. Jpn., **80** 024710, 2011.

[119] V.A. Sidorov, M. Nicklas, P.G. Pagliuso, J.L. Sarrao, Y. Bang, A.V. Balatsky, and J.D. Thompson. Superconductivity and Quantum Criticality in $CeCoIn_5$. Phys. Rev. Lett., **89** 157004, 2002.

[120] W. Higemoto, A. Koda, R. Kadono, Y. Kawasaki, Y. Haga, D. Aoki, R. Settai, H. Shishido, and Y. Onuki. μSR Studies on Heavy Fermion Superconductors $CeIrIn_5$ and $CeCoIn_5$. J. Phys. Soc. Jpn., **71** 1023, 2002.

[121] J.S. Kim, J. Alwood, G.R. Stewart, J.L. Sarrao, and J.D. Thompson. Specific heat in high magnetic fields and non-Fermi-liquid behavior in $CeMIn_5$ (M=Ir, Co). Phys. Rev. B, **64** 134524, 2001.

[122] F. Ronning, C. Capan, A. Bianchi, R. Movshovich, A. Lacerda, M.F. Hundley, J.D. Thompson, P.G. Pagliuso, and J.L. Sarrao. Field-tuned quantum critical point in $CeCoIn_5$ near the superconducting upper critical field. Phys. Rev. B, **71** 104528, 2005.

[123] F. Ronning, C. Capan, E.D. Bauer, J.D. Thompson, J.L. Sarrao, and R. Movshovich. Pressure study of quantum criticality in $CeCoIn_5$. Phys. Rev. B, **73** 064519, 2006.

[124] J. Paglione, T.A. Sayles, P.-C. Ho, J.R. Jeffries, and M.B. Maple. Incoherent non-Fermi-liquid scattering in a Kondo lattice. Nat. Phys., **3** 703, 2007.

[125] S.K. Goh, J. Paglione, M. Sutherland, E.C.T. Farrell, C. Bergemann, T.A. Sayles, and M.B. Maple. Fermi-Surface Reconstruction in $CeRh_{1-x}Co_xIn_5$. Phys. Rev. Lett., **101** 056402, 2008.

[126] C. Capan, Y.-J. Jo, L. Balicas, R.G. Goodrich, J.F. DiTusa, I. Vekhter, T.P. Murphy, A.D. Bianchi, L.D. Pham, J.Y. Cho, J.Y. Chan, D.P. Young, and Z. Fisk. Fermi surface evolution through a heavy-fermion superconductor-to-antiferromagnet transition: de Haas-van Alphen effect in Cd-substituted $CeCoIn_5$. Phys. Rev. B, **82** 035112, 2010.

[127] Y. Tokiwa, R. Movshovich, F. Ronning, E.D. Bauer, A.D. Bianchi, Z. Fisk, and J.D. Thompson. Anomalous effect of doping on the superconducting state of $CeCoIn_5$ in high magnetic fields. Phys. Rev. B, **82** 220502, 2010.

[128] C.H. Booth, T. Durakiewicz, C. Capan, D. Hurt, A.D. Bianchi, J.J. Joyce, and Z. Fisk. Electronic structure and f-orbital occupancy in Yb-substituted $CeCoIn_5$. Phys. Rev. B, **83** 235117, 2011.

[129] L. Shu, R.E. Baumbach, M. Janoschek, E. Gonzales, K. Huang, T.A. Sales, J. Paglione, J. O'Brian, J.J. Hamlin, D.A. Zocco, P.-C. Ho, C.A. McElroy, and M.B. Maple. Correlated Electron State in $Ce_{1-x}Yb_xCoIn_5$ Stabilized by Cooperative Valence Fluctuations. Phys. Rev. Lett., **106** 156403, 2011.

[130] E.D. Bauer, Y.-F. Yang, C. Capan, R.R. Urbano, C.F. Miclea, H. Sakai, F. Ronning, M.J. Graf, A.V. Balatsky, R. Movshovich, A.D. Bianchi, A.P. Reyes, P.L. Kuhns, J.D. Thompson, and Z. Fisk. Electronic inhomogeneity in a Kondo lattice. Proc. Natl. Acad. Sci., **108** 6857, 2011.

[131] L.D. Pham, T. Park, S. Maquilon, J.D. Thompson, and Z. Fisk. Reversible Tuning of the Heavy-Fermion Ground State in $CeCoIn_5$. Phys. Rev. Lett., **97** 056404, 2006.

[132] P. Coleman. Introduction to Many Body Physics. Rutgers University. 143, 2012.

[133] M. Daniel, E.D. Bauer, S.-W. Han, C.H. Booth, A.L. Cornelius, P.G. Pagliuso, and J.L. Sarrao. Perturbing the Superconducting Planes in $CeCoIn_5$ by Sn Substitution. Phys. Rev. Lett., **95** 016406, 2005.

[134] C.H. Booth, E.D. Bauer, A.D. Bianchi, F. Ronning, J.D. Thompson, J.L. Sarrao, J.Y. Cho, J.Y. Chan, C. Capan, and Z. Fisk. Local structure and site occupancy of Cd and Hg substitutions in $CeTIn_5$ (T = Co, Rh, and Ir). Phys. Rev. B, **79** 144519, 2009.

[135] E.D. Bauer, F. Ronning, C. Capan, M.J. Graf, D. Vandervelde, H.Q. Yuan, M.B. Salamon, D.J. Mixson, N.O. Moreno, S.R. Brown, J.D. Thompson, R. Movshovich, M.F. Hundley, J.L. Sarrao, P.G. Pagliuso, and S.M. Kauzlarich. Thermodynamic and transport investigation of $CeCoIn_{5-x}Sn_x$. Phys. Rev. B, **73** 245109, 2006.

[136] R.R. Urbano, B.-L. Young, N.J. Curro, J.D. Thompson, L.D. Pham, and Z. Fisk. Interacting Antiferromagnetic Droplets in Quantum Critical $CeCoIn_5$. Phys. Rev. Lett., **99** 146402, 2007.

[137] Y.-F. Yang, Z. Fisk, H.-O. Lee, J.D. Thompson, and D. Pines. Scaling the Kondo lattice. Nat. phys, **454** 611, 2008.

[138] Y.M. Kalychak, V.I. Zaremba, V.M. Baranyak, V.A. Bruskov, and P.Yu. Zavalii. Russ. Metall., **1** 213, 1989.

[139] V.I. Zaremba, U.Ch. Rodewald, R.-D. Hoffmann, Y.M. Kalychak, and R. Pittgen. The Indium-Rich Intermetallics $YbCoIn_5$, $YbRhIn_5$, and $YbPtIn_4$. Z. Anorg. Allg. Chem., **629** 1157, 2003.

[140] J.P. Perdew, K. Burke, and M. Ernzerhof. Generalized Gradient Approximation Made Simple. Phys. Rev. Lett., **77** 3865, 1996.

[141] X. Gonze, B. Amadon, P.-M. Anglade, J.-M. Beuken, F. Bottin, P. Boulanger, F. Bruneval, D. Caliste, R. Caracas, M. Côté. ABINIT: First-principles approach to material and nanosystem properties. Comput. Phys. Commun., **180** 2582, 2009.

[142] N. Marzari and D. Vanderbilt. Maximally localized generalized Wannier functions for composite energy bands Phys. Rev. B, **56** 12847, 1997.

[143] http://www.fplo.de/.

[144] K. Koepernik and H. Eschrig, Phys. Rev. B, **59** 1743, 1999.

[145] S. Elgazzar, I. Opahle, M. Richter, and P.M. Openeer. Electronic structure and Fermi surface of $PrMIn_5$ (M = Co, Rh, and Ir) compounds. Phys. Rev. B, **77** 125105, 2008.

[146] B. Amadon, F. Jollet, and M. Torrent. γ and β cerium: LDA+U calculations of ground-state parameters. Phys. Rev. B, **77** 155104, 2008.

[147] M. Dzero and X. Huang. Correlated disorder in Kondo lattice. J. Phys.: Condens. Matter, **24** 075603, 2012.

[148] N. Harrison, U. Alver, R.G. Goodrich, I. Vekhter, J.L. Sarrao, P.G. Pagliuso, N.O. Moreno, L. Balicas, Z. Fisk, D. Hall, R.T. Macaluso, and J.Y. Chan. $4f$-Electron Localization in $Ce_xLa_{1-x}MIn_5$ with M = Co, Rh, or Ir. Phys. Rev. Lett., **93** 186405, 2004.

[149] J. Paglione and R.L. Greene. High-temperature superconductivity in iron-based materials. Nat. Phys., **6** 645-658, 2010.

[150] D.N. Basov and A.V. Chubukov. Manifesto for higher T_c. Nat. Phys., **7** 272, 2011.

[151] K. Ishida, Y. Nakaii, H. Hosono. To What Extent Iron-Pnictide New Superconductors Have Been Clarified: A Progress Report. J. Phys. Soc. Japan, **78** 062001, 2009.

[152] D.C. Johnston. The Puzzle of High Temperature Superconductivity in Layered Iron Pnictides and Chalcogenides. Adv. Phys., **59** 803-1061, 2010.

[153] M. Rotter, M. Tegel, D. Johrendt, I. Schellenberg, W. Hermes, and R. P$\ddot{o}$ttgen. Spin-density-wave anomaly at 140 K in the ternary iron arsenide $BaFe_2As_2$. Phys. Rev. B, **78** 020503, 2008.

[154] L.X. Yang, Y. Zhang, H.W. Ou, J.F. Zhao, D.W. Shen, B. Zhou, J. Wei, F. Chen, M. Xu, C. He, Y. Chen, Z.D. Wang, X. F. Wang, T. Wu, G. Wu, X.H. Chen, M. Arita, K. Shimada, M. Taniguchi, Z.Y. Lu, T. Xiang, and D.L. Feng. Electronic Structure and Unusual Exchange Splitting in the Spin-Density-Wave State of the $BaFe_2As_2$. Parent Compound of Iron-Based Superconductors. Phys. Rev. Lett., **102** 107002, 2009.

[155] D. Hsieh, Y. Xia, L. Wray, D. Qian, K.K. Gomes, A. Yazdani, G.F. Chen,J.L. Luo, N.L. Wang, and M.Z. Hasan. Experimental determination of the microscopic origin of magnetism in parent iron pnictides. arXiv:0812.2289.

[156] S.O. Diallo, V.P. Antropov, T.G. Perring, C. Broholm, J.J. Pulikkotil, N. Ni, S.L. Bud'ko, P.C. Canfield, A. Kreyssig, A.I. Goldman, and R.J. McQueeney. Phys. Rev. Lett., **102** 187206, 2009.

[157] P.L. Alireza, Y.T.C. Ko, J. Gillett, C.M. Petrone, J.M. Cole, G.G. Lonzarich, and S.E. Sebastian. Superconductivity up to 29 K in $SrFe_2As_2$ and $BaFe_2As_2$ at high pressures. J. Phys. Condens. Matter, **21** 012208, 2009.

[158] E. Colombier, S.L. Bud'ko, N. Ni, and P.C. Canfield. Complete pressure-dependent phase diagrams for $SrFe_2As_2$ and $BaFe_2As_2$. Phys. Rev. B, **79** 224518, 2009.

[159] F. Ishikawa, N. Eguchi, M. Kodama, K. Fujimaki, M. Einaga, A. Ohmura, A. Nakayama, A. Mitsuda, and Y. Yamada. Zero-resistance superconducting phase in $BaFe_2As_2$ under high pressure. Phys. Rev. B, **79** 172506, 2009.

[160] H. Fukazawa, N. Takeshita, T. Yamazaki, K. Kondo, K. Hirayama, Y. Kohori, K. Miyazawa, H. Kito, H. Eisaki, and A. Iyo. Suppression of magnetic order by pressure in $BaFe_2As_2$. J. Phys. Soc. Jpn., **77** 105004, 2008.

[161] K. Matsubayashi, N. Katayama, K. Ohgushi, A. Yamada, K. Munakata, T. Matsumoto, and Y. Uwatoko. Intrinsic properties of AFe_2As_2 (A = Ba, Sr) single crystal under highly hydrostatic pressure conditions. J. Phys. Soc. Jpn., **78** 073706 (2009).

[162] T. Yamazaki, N. Takeshita, R. Kobayashi, H. Fukazawa, Y. Kohori, K. Kihou, C.-H. Lee, H. Kito, A. Iyo, H. Eisaki. Appearance of pressure-induced superconductivity in $BaFe_2As_2$ under hydrostatic conditions and its extremely high sensitivity to uniaxial stress. Phys. Rev. B, **81** 224511, 2010.

[163] N. Ni, M.E. Tillman, J.-Q. Yan, A. Kracher, S.T. Hannahs, S.L. Bud'ko, and P.C. Canfield. Effects of Co substitution on thermodynamic and transport properties and anisotropic H_{c2} in $Ba(Fe_{1-x}Co_x)_2As_2$ single crystals. Phys. Rev. B, **78** 214515, 2008.

[164] L.J. Li, Y.K. Luo, Q.B. Wang, H. Chen, Z. Ren, Q. Tao, Y.K. Li, X. Lin, M. He, Z.W. Zhu, G.H. Cao, and Z.A. Xu. Superconductivity induced by Ni doping in $BaFe_2As_2$ single crystals. New J. Phys., **11** 025008, 2009.

[165] S. Sharma, A. Bharathi, S. Chandra, V. Raghavendra Reddy, S. Paulraj, A.T. Satya, V.S. Sastry, A. Gupta, and C.S. Sundar. Superconductivity in Ru-substituted polycrystalline $BaFe_{2-x}Ru_xAs_2$. Phys. Rev. B, **81** 174512, 2010.

[166] S. Jiang, H. Xing, G. Xuan, C. Wang, Z. Ren, C. Feng, J. Dai, Z. Xu, and G. Cao. Superconductivity up to 30 K in the vicinity of the quantum critical point in $BaFe_2(As_{1-x}P_x)_2$. J. Phys. Condens. Matter, 21 382203, 2009.

[167] S.A.J. Kimber, A. Kreyssig, Y.-Z. Zhang, H.O. Jeschke, R. Valent, F. Yokaichiya, E. Colombier, J. Yan, T.C. Hansen, T. Chatterji, R.J. McQueeney, P.C. Canfield, A.I. Goldman, and D.N. Argyriou. Similarities between structural distortions under pressure and chemical doping in superconducting $BaFe_2As_2$. Nature Mater., **8** 471, 2009.

[168] T. Goko, A.A. Aczel, E. Baggio-Saitovitch, S.L. Bud'ko, P.C. Canfield, J.P. Carlo, G.F. Chen, P. Dai, A.C. Hamann, W.Z. Hu, H. Kageyama, G.M.Luke, J.L. Luo, B. Nachumi, N. Ni, D. Reznik, D.R. Sanchez-Candela, A.T. Savici, K.J. Sikes, N.L. Wang, C.R. Wiebe, T.J. Williams, T. Yamamoto, W. Yu, and Y.J. Uemura. Superconducting

state coexisting with a phase-separated static magnetic order in (Ba,K)Fe_2As_2, (Sr,Na)Fe_2As_2, and $CaFe_2As_2$. Phys. Rev. B, **80** 024508, 2009.

[169] F. Massee, Y. Huang, R. Huisman, S. de Jong, J.B. Goedkoop, and M.S. Golden. Nanoscale superconducting-gap variations and lack of phase separation in optimally doped $BaFe_{1.86}Co_{0.14}As_2$. Phys. Rev. B, **79** 220517, 2009.

[170] M.-H. Julien, H. Mayaffre, M. Horvatić, C. Berthier, X.D. Zhang, W. Wu, G.F. Chen, N.L. Wang, and J.L. Luo. Homogeneous vs. inhomogeneous coexistence of magnetic order and superconductivity probed by NMR in Co- and K-doped iron pnictides. Europhys. Lett., **87** 37001, 2009.

[171] J.T. Park, D.S. Inosov, C. Niedermayer, G.L. Sun, D. Haug, N.B. Christensen, R. Dinnebier, A.V. Boris, A.J. Drew, L. Schulz, T. Shapoval, U. Wolff, V. Neu, X. Yang, C.T. Lin, B. Keimer, and V. Hinkov. Electronic Phase Separation in the Slightly Underdoped Iron Pnictide Superconductor $Ba_{1-x}K_xFe_2As_2$. Phys. Rev. Lett., **102** 117006, 2009.

[172] A.A. Aczel, E. Baggio-Saitovitch, S.L. Bud'ko, P.C. Canfield, J.P. Carlo, G.F. Chen, P. Dai, T. Goko, W.Z. Hu, G.M. Luke, J.L. Luo, N. Ni, D.R. Sanchez-Candela, F.F. Tafti, N.L. Wang, T.J. Williams, W. Yu, and Y.J. Uemura. Muon-spin-relaxation studies of magnetic order and superfluid density in antiferromagnetic NdFeAsO, $BaFe_2As_2$, and superconducting $Ba_{1-x}K_xFe_2As_2$. Phys. Rev. B, **78** 214503, 2008.

[173] A.V. Chubukov, D.V. Efremov, and I. Eremin. Magnetism, superconductivity, and pairing symmetry in iron-based superconductors. Phys. Rev. B, **78** 134512, 2008.

[174] V. Stanev, J. Kang, and Z. Tesanovic. Spin fluctuation dynamics and multiband superconductivity in iron pnictides. Phys. Rev. B, **78** 184509, 2008.

[175] Y. Ran, F. Wang, H. Zhai, A. Vishwanath, and D.-H. Lee. Nodal spin density wave and band topology of the FeAs-based materials. Phys. Rev. B, **79** 014505 2009.

[176] S. Lebĝue. Electronic structure and properties of the Fermi surface of the superconductor LaOFeP

[177] D.J. Singh and M.-H. Du. Density Functional Study of $LaFeAsO_{1-x}F_x$: A Low Carrier Density Superconductor Near Itinerant Magnetism. Phys. Rev. Lett., **100** 237003, 2008.

[178] D.J. Singh. Electronic structure and doping in $BaFe_2As_2$ and LiFeAs: Density functional calculations. Phys. Rev. B, **78** 094511, 2008.

[179] G. Xu, H. Zhang, X. Dai, and Z. Fang. Electron-hole asymmetry and quantum critical point in hole-doped $BaFe_2As_2$. Europhys. Lett., **84** 67015, 2008.

[180] K. Kuroki, H. Usui, S. Onari, R. Arita, and H. Aoki. Pnictogen height as a possible switch between high-T_c nodeless and low-T_c nodal pairings in the iron-based superconductors. Phys. Rev. B, **79** 224511, 2009.

[181] A. Carrington, A.I. Coldea, J.D. Fletcher, N.E. Hussey, C.M.J. Andrew, A.F. Bangura, J.G. Analytis, J.-H. Chu, A.S. Erickson, I.R. Fisher, R.D. McDonald. Quantum oscillation studies of the Fermi surface of LaFePO. Physica C, **469** 459, 2009.

[182] A.I. Coldea, J.D. Fletcher, A. Carrington, J.G. Analytis, A.F. Bangura, J.-H. Chu, A.S. Erickson, I.R. Fisher, N.E. Hussey, and R.D. McDonald. Fermi Surface of Superconducting LaFePO Determined from Quantum Oscillations. Phys. Rev. Lett., **101** 216402, 2008.

[183] D.H. Lu, M. Yi, S.K. Mo, A.S. Erickson, J. Analytis, J.C. Chu, D.J. Singh, Z. Hussain, T.H. Geballe, I.R. Fisher, Z.X. Shen. Electronic structure of the iron-based superconductor LaOFeP. Nature, **455** 81, 2008.

[184] T. Kondo, A.F. Santander-Syro, O. Copie, C. Liu, M.E. Tillman, E.D. Mun, J. Schmalian, S.L.Bud'ko, M.A. Tanatar, P.C. Canfield, and A. Kaminski. Momentum Dependence of the Superconducting Gap in $NdFeAsO_{0.9}F_{0.1}$. Single Crystals Measured by Angle Resolved Photoemission Spectroscopy. Phys. Rev. Lett., **101** 147003, 2008.

[185] G. Liu, H. Liu, L. Zhao, W. Zhang, X. Jia, J. Meng, X. Dong, J. Zhang, G.F. Chen, G. Wang, Y. Zhou, Y. Zhu, X. Wang, Z. Xu, C. Chen, and X.J. Zhou. Band-structure reorganization across the magnetic transition in $BaFe_2As_2$ seen via high-resolution angle-resolved photoemission. Phys. Rev. B, **80** 134519, 2009.

[186] C. Liu, G.D. Samolyuk, Y. Lee, N. Ni, T. Kondo, A.F. Santander-Syro, S.L. Bud'ko, J.L. McChesney, E. Rotenberg, T. Valla, A.V. Fedorov, P.C. Canfield, B.N. Harmon, and A. Kaminski. K-Doping Dependence of the Fermi Surface of the Iron-Arsenic $Ba_{1-x}K_xFe_2As_2$ Superconductor Using Angle-Resolved Photoemission Spectroscopy. Phys. Rev. Lett., **101** 177005, 2008.

[187] H. Ding, P. Richard, K. Nakayama, K. Sugawara, T. Arakane, Y. Sekiba, A. Takayama, S. Souma, T. Sato, T. Takahashi, Z. Wang, X. Dai, Z. Fang, G.F. Chen, J.L. Luo and N.L. Wang. Observation of Fermi-surface-dependent nodeless superconducting gaps in $Ba_{0.6}K_{0.4}Fe_2As_2$. Europhys. Lett, **83** 47001, 2008.

[188] T. Yoshida, I. Nishi, S. Ideta, A. Fujimori, M. Kubota, K. Ono, S. Kasahara, T. Shibauchi, T. Terashima, Y. Matsuda, H. Ikeda, and R. Arita. Two-Dimensional and Three-Dimensional Fermi Surfaces of Superconducting $BaFe_2(As_{1-x}P_x)_2$ and Their Nesting Properties Revealed by Angle-Resolved Photoemission Spectroscopy. Phys. Rev. Lett., **106** 117001, 2011.

[189] T. Terashima, N. Kurita, M. Tomita, K. Kihou, C.-H. Lee, Y. Tomioka, T. Ito, A. Iyo, H. Eisaki, T. Liang, M. Nakajima, S. Ishida, S.-i. Uchida, H. Harima, and S. Uji. Complete Fermi Surface in $BaFe_2As_2$ Observed via Shubnikov-de Haas Oscillation Measurements on Detwinned Single Crystals. Phys. Rev. Lett., **107** 176402, 2011.

[190] J.G. Analytis, R.D. McDonald, J.-H. Chu, S.C. Riggs, A.F. Bangura, C. Kucharczyk, M. Johannes, and I.R. Fisher. Quantum oscillations in the parent pnictide $BaFe_2As_2$: Itinerant electrons in the reconstructed state. Phys. Rev. B, **80** 064507, 2009.

[191] S.E. Sebastian, J. Gillett, N. Harrison, P.H.C. Lau, D.J. Singh, C.H. Mielke. and G.G. Lonzarich. Quantum oscillations in the parent magnetic phase of an iron arsenide high temperature superconductor. J. Phys.: Condens. Matter, **20** 422203, 2008.

[192] N. Harrison, R.D. McDonald, C.H. Mielke, E.D. Bauer, F. Ronning, and J.D. Thompson. Quantum oscillations in antiferromagnetic $CaFe_2As_2$ on the brink of superconductivity. J. Phys.: Condens. Matter, **21** 322202, 2009.

[193] H. Sugawara, R. Settai, Y. Doi, H. Muranaka, K. Katayama, H. Yamagami, and Y. Onuki. de Haas-van Alphen Effect in LaFePO with Two-Dimensional Cylindrical Fermi Surfaces. J. Phys. Soc. Jpn., **77** 113711, 2008.

[194] H. Muranaka, Y. Doi, K. Katayama, H. Sugawara, R. Settai, F. Honda, T.D. Matsuda, Y. Haga, H. Yamagami, and Y. Onuki. Two-dimensional Fermi surfaces in LaRuPO and LaFePO versus three-dimensional Fermi surfaces in $LaFe_2P_2$. J. Phys. Soc. Jpn., **78** 053705, 2009.

[195] H. Shishido, A.F. Bangura, A.I. Coldea, S. Tonegawa, K. Hashimoto, S. Kasahara, P.M.C. Rourke, H. Ikeda, T. Terashima, R. Settai, Y. Ōnuki, D. Vignolles, C. Proust, B. Vignolle, A. McCollam, Y. Matsuda, T. Shibauchi, and A. Carrington. Evolution of the Fermi Surface of $BaFe_2(As_{1-x}P_x)_2$ on Entering the Superconducting Dome. Phys. Rev. Lett., **104** 057008, 2010.

[196] J.G. Analytis, J.-H. Chu, R.D. McDonald, S.C. Riggs, and I.R. Fisher. Enhanced Fermi-Surface Nesting in Superconducting $BaFe_2(As_{1-x}P_x)_2$ Revealed by the de Haas-van Alphen Effect. Phys. Rev. Lett., **105** 207004, 2010.

[197] B.J. Arnold, S. Kasahara, A.I. Coldea, T. Terashima, Y.Matsuda, T. Shibauchi, and A. Carrington. Nesting of electron and hole Fermi surfaces in nonsuperconducting $BaFe_2P_2$. Phys. Rev. B, **83** 220504, 2011.

[198] J.G. Analytis, C.M.J. Andrew, A.I. Coldea, A. McCollam, J.-H. Chu, R.D. McDonald, I.R. Fisher, and A. Carrington. Fermi Surface of $SrFe_2P_2$ Determined by the de Haas-van Alphen Effect. Phys. Rev. Lett., **103** 076401, 2009.

[199] P.J.W. Moll, J. Kanter, R.D. McDonald, F. Balakirev, P. Blaha, K. Schwarz, Z. Bukowski, N.D. Zhigadlo, S. Katrych, K. Mattenberger, J. Karpinski, and B. Batlogg. Quantum oscillations of the superconductor $LaRu_2P_2$: Comparable mass enhancement $\lambda \approx 1$ in Ru and Fe phosphides. Phys. Rev. B, **84** 224507, 2011.

[200] V. Cvetkovic and Z. Tesanovic. Multiband magnetism and superconductivity in Fe-based compounds. Europhys. Lett., **85** 37002, 2009.

[201] V. Brouet, M. Marsi, B. Mansart, A. Nicolaou, A. Taleb-Ibrahimi, P. Le Fèvre, F. Bertran, F. Rullier-Albenque, A. Forget, and D. Colson. Nesting between hole and electron pockets in Ba($Fe_{1-x}Co_x$)$_2$As$_2$ ($x = 0$-0.3) observed with angleresolved photoemission. Phys. Rev. B, **80** 165115, 2009.

[202] Y. Sekiba, T. Sato, K. Nakayama, K. Terashima, P. Richard, J.H. Bowen, H. Ding, Y.-M. Xu, L.J. Li, G.H. Cao, Z.-A. Xu, and T. Takahashi. Electronic structure of heavily electron-doped $BaFe_{1.7}Co_{0.3}As_2$ studied by angle-resolved photoemission, New J. Phys., **11** 025020, 2009.

[203] H. Wadati, I. Elfimov, and G.A. Sawatzky. Where Are the Extra d Electrons in Transition-Metal-Substituted Iron Pnictides? Phys. Rev. Lett., **105** 157004, 2010.

[204] M. Reehuis, and W. Jeitschko. Structure and magnetic properties of the phosphides $CaCo_2P_2$ and LnT_2P_2 with $ThCr_2Si_2$ structure and LnTP with PbFCl structure (Ln = lanthanoids, T = Fe, Co, Ni). J. Phys. Chem. Solids, **51** 961, 1990.

[205] E. Mörsen, B.D. Mosel, W. Müller-Warmuth, M. Reehuis, W. Jeitschko. Mössbauer and magnetic susceptibility investigations of strontium, lanthanum and europium transition metal phosphides with $ThCr_2Si_2$ type structure. J. Phys. Chem. Solids, **49** 785, 1988.

[206] R. Marchand, W. Jeitschko. Ternary lanthanoid-transition metal pnictides with $ThCr_2Si_2$-type structure. J. Solid State. Chem., **24** 351, 1978.

[207] A.I. Coldea, C.M.J. Andrew, J.G. Analytis, R.D. McDonald, A.F. Bangura, J.-H. Chu, I.R. Fisher, and A. Carrington. Topological Change of the Fermi Surface in Ternary Iron Pnictides with Reduced c/a Ratio: A de Haas-van Alphen Study of $CaFe_2P_2$. Phys. Rev. Lett., **103** 026404, 2009.

[208] T. Terashima, M. Kimata, H. Satsukawa, A. Harada, K. Hazama, M. Imai, S. Uji, H. Kito, A. Iyo, H. Eisaki, and H. Harima. Fermi Surface in $BaNi_2P_2$. J. Phys. Soc. Jpn., **78** 033706, 2009.

[209] N.R. Werthamer, E. Helfand, and P.C. Hohenberg. Temperature and Purity Dependence of the Superconducting Critical Field, H_{c2}. III. Electron Spin and Spin-Orbit Effects. Phys. Rev., **147** 295, 1996.

[210] G.F. Chen, Z. Li, J. Dong, G. Li, W.Z. Hu, X.D. Zhang, X.H. Song, P. Zheng, N.L. Wang, and J.L. Luo. Transport and anisotropy in single-crystalline $SrFe_2As_2$ and $A_{0.6}K_{0.4}Fe_2As_2$ (A = Sr, Ba) superconductors. Phys. Rev. B, **78** 224512, 2008.

[211] N. Berry, C. Capan, G. Seyfarth, A.D. Bianchi, J. Ziller, and Z. Fisk. Superconductivity without Fe or Ni in the phosphides $BaIr_2P_2$ and $BaRh_2P_2$. Phys. Rev. B, **79** 180502, 2009.

[212] A. Carrington. Quantum oscillation studies of the Fermi surface of iron-pnictide superconductors. Rep. Prog. Phys., **74** 124507, 2011.

[213] B.C. Sales. Filled Skutterudites. Handbook on the Physics and Chemistry of Rare Earths. edited by K.A. Gschneidner Jr., J.-C.G. Bunzli, and V.K. Pecharsky, (Elsevier, Amsterdam, 2003), Vol. 33, p. 1-34.

[214] W. Jeitschko, D. Braun. $LaFe_4P_{12}$ with filled $CoAs_3$-type structure and isotypic lanthanoid-transition metal polyphosphides. Acta Cryst. B, **33** 3401-3406, 1977.

[215] W. Schnelle. Scientific Report 2006-2008 (MPI für Chemische Physik fester Stoffe, Dresden, 2009), p. 31ff.

[216] Y. Aoki, H. Sugawara, H. Harima, and H. Sato. J. Phys. Soc. Jpn., **74** 209, 2005.

[217] M.B. Maple, Z. Henkie, W.M. Yuhasz, P.-C. Ho, T. Yanagisawa, T.A. Sayles, N.P. Butch, J.R. Jeffries, A. Pietraszko. Strongly correlated electron phenomena in Pr-based filled skutterudite compounds. J. Magn. Magn. Mater., **310** 182-187, 2007.

[218] H. Sato, D. Kikuchi, K. Tanaka, H. Aoki, K. Kuwahara, Y. Aoki, M. Kohgi, H. Sugawara, K. Iwasa. Novel electronic states realized in the filled skutterudites containing rare earth elements with more than one $4f$-electrons. J. Magn. Magn. Mater., **310** 188-194, 2007.

[219] G. Mahan, B. Sales, J. Sharp. Thermoelectric Materials: New Approaches to an Old Problem. Phys. Today, **50** 42, 1997.

[220] G.S. Nolas, D.T. Morelli, T.M. Tritt. SKUTTERUDITES: A Phonon-Glass-Electron Crystal Approach to Advanced Thermoelectric Energy Conversion Applications. Annu. Rev. Mater. Sci., **29** 89, 1999.

[221] D.J. Singh, I.I. Mazin. Calculated thermoelectric properties of La-filled skutterudites. Phys. Rev. B, **56** R1650-R1653, 1997.

[222] H. Sugawara, T.D. Matsuda, K. Abe, Y. Aoki, H. Sato, S. Nojiri, Y.Inada, R.Settai, and Y. Onuki. Exotic heavy-fermion state in the filled skutterudite $PrFe_4P_{12}$ uncovered by the de Haas-van Alphen effect. Phys. Rev. B, **66** 134411, 2002.

[223] H. Sugawara, S. Osaki, S.R. Saha, Y. Aoki, H. Sato, Y. Inada, H. Shishido, R. Settai, Y. Onuki, H. Harima, and K. Oikawa. Fermi surface of the heavy-fermion superconductor $PrOs_4Sb_{12}$. Phys. Rev. B, **66** 220504R, 2002.

[224] H. Sato, H. Sugawara, T. Namiki, S.R. Saha, S. Osaki, T.D. Matsuda, Y. Aoki, Y. Inada, H. Shishido, R. Settai, and Y. Onuki. Exotic behaviours in the Pr-based filled skutterudites. J. Phys.: Condens. Matter, **15** S2063-S2070, 2003.

[225] R. Gumeniuk, W. Schnelle, H. Rosner, M. Nicklas, A. Leithe-Jasper, and Yu. Grin. Phys. Rev. Lett., **100** 017002, 2008.

[226] E. Bauer, A. Grytsiv, X.-Q. Chen, N. Melnychenko-Koblyuk, G. Hilscher, H. Kaldarar, H. Michor, E. Royanian, G. Giester, M. Rotter, R. Podloucky, and P. Rogl. Superconductivity in Novel Ge-Based Skutterudites: $\{Sr, Ba\}$ Pt_4Ge_{12}. Phys. Rev. Lett., **99** 217001, 2007.

[227] D. Kaczorowski and V.H. Tran. Superconductivity in the actinoid-bearing filled skutterudite $ThPt_4Ge_{12}$ Phys. Rev. B, **77** 180504, 2008.

[228] E. Bauer, X.-Q. Chen, P. Rogl, G. Hilscher, H. Michor, E. Royanian, R. Podloucky, G. Giester, O. Sologub, and A.P. Goncalves. Superconductivity and spin fluctuations in Th,UPt_4Ge_{12} skutterudites. Phys. Rev. B, **78** 064516, 2008.

[229] A. Maisuradze, M. Nicklas, R. Gumeniuk, C. Baines, W. Schnelle, H. Rosner, A. Leithe-Jasper, Yu. Grin, and R. Khasanov, Superfluid Density and Energy Gap Function of Superconducting $PrPt_4Ge_{12}$. Phys. Rev. Lett., **103** 147002, 2009.

[230] A. Maisuradze, W. Schnelle, R. Khasanov, R. Gumeniuk, M. Nicklas, H. Rosner, A. Leithe-Jasper, Yu. Grin, A. Amato, and P. Thalmeier. Evidence for time-reversal symmetry breaking in superconducting $PrPt_4Ge_{12}$. Phys. Rev. B, **82** 024524, 2010.

[231] F. Kanetake, H. Mukuda, Y. Kitaoka, K. Magishi, H. Sugawara, K.M. Itoh, and E.E. Haller. Superconducting Characteristics of Filled Skutterudites $LaPt_4Ge_{12}$ and $PrPt_4Ge_{12}$: ^{73}Ge-NQR/NMR Studies. J. Phys. Soc. Jpn., **79** 063702, 2010.

[232] Y. Nakamura, H. Okazaki, R. Yoshida, T. Wakita, H. Takeya, K. Hirata, M. Hirai, Y. Muraoka, and T. Yokoya. Comparative photoemission studies on the superconducting gap of the filled skutterudite superconductors $LaPt_4Ge_{12}$ and $PrPt_4Ge_{12}$. Phys. Rev. B, **82** 014521, 2012.

[233] M. Marchevsky, M.J. Higgins, and S. Bhattacharya. Two coexisting vortex phases in the peak effect regime in a superconductor. Nat. Phys., **409** 591-594, 2001.

[234] P.-C. Ho, J. Singleton, M.B. Maple, H. Harima, P.A. Goddard, Z. Henkie, and A. Pietraszko. A de Haas-van Alphen study of the filled skutterudite compounds $PrOs_4As_{12}$ and $LaOs_4As_{12}$. New J. Phys., **9** 269, 2007.

[235] H. Sugawara, Y. Abe, Y. Aoki, H. Sato, M. Hedo, R. Settai, Y. Onuki, and H. Harima. The Fermi Surface in Filled Skutterudite RFe_4P_{12} (R = La and Nd). J. Phys. Soc. Jpn., **69** 2938-2946, 2000.

[236] R.G. Goodrich, N. Harrison, and Z. Fisk. Fermi Surface Changes across the Neél Phase Boundary of NdB_6. Phys. Rev. Lett., **97** 146404, 2006.

Publication

A. Polyakov, O. Ignatchik, B. Bergk, K. Götze, A.D. Bianchi, S. Blackburn, B. Prévost, G. Seyfarth, M. Côté, D. Hurt, C. Capan, Z. Fisk, R.G. Goodrich, I. Sheikin, M. Richter, and J. Wosnitza;
Fermi-surface evolution in Yb-substituted $CeCoIn_5$
Physical Review B, **85** 245119, 2012.

Acknowledgements

I would like to thank my supervisor, Prof. Jochen Wosnitza, for giving me the opportunity to carry out this work in his laboratory. I wish to thank Prof. Andrea Bianchi, not only because of providing high-quality $Ce_{1-x}Yb_xCoIn_5$ *and iron-based phosphides single crystals, but also for his kind consent to be a reviewer of this thesis.*

I am obliged to my colleagues at the Dresden High Magnetic Field Laboratory for the friendly atmosphere in the lab; for help, fun, and fruitful discussions, which have made my time in Dresden a pleasant experience. In particular, I wish to thank Dr. Oleg Ignatchik for patiently guiding me during my thesis and for our friendly relationship. From Oleg, I learned a lot about cryogenics and the de Haas-van Alphen measurements. I owe so much to Dr. Marc Uhlarz and Dr. Artem Pronin for their continuous support and willingness to help. I would like to thank my roommates Theo Fischer, Rico Beyer, and Salim Erfanifam for creating beautiful working atmosphere in our office and many fruitful discussions. I wish to thank Kathrin Götze and Geoffrey Chanda for their thoughtful reading of the preliminary version of this thesis with critical eyes and for providing insightful comments and suggestions.

I am indebted to people who contributed to this thesis: Prof. Michael Côté, Simon Blackburn and Bobby Prévost for band-structure calculations, Dr. Christoph Geibel for giving iron-based phosphide $CeFe_2P_2$ *samples, Dr. Helge Rosner and Vivien Petzold for providing skutterudite* $PrPt_4Ge_{12}$ *samples and FPLO calculations for this system, Dr. Ilya Sheikin and Dr. Beate Bergk for night measurements at the LNCMI-Grenoble.*

This thesis could not have been written without the inspiration of my family and friends, to whom I am heartily thankful. I am grateful to my parents for their encouragements all along. I express deepest gratitude to my dear wife, Elena, to whom I dedicate this work. Without her patience, delicate attitude, and her support in everything I do, this work would not have been done.

Versicherung

Hiermit versichere ich, dass ich die vorliegende Arbeit ohne unzulässige Hilfe Dritter und ohne Benutzung anderer als der angegebenen Hilfsmittel angefertigt habe. Die aus fremden Quellen direkt oder indirekt übernommenen Gedanken sind als solche kenntlich gemacht. Die Arbeit wurde bisher weder im Inland noch im Ausland in gleicher oder ähnlicher Form einer anderen Prüfungsbehörde vorgelegt.

Die vorliegende Doktorarbeit wurde am Hochfeld-Magnetlabor Dresden im Helmholtz-Zentrum Dresden-Rossendorf e. V. unter der wissenschaftlichen Betreuung von Herrn Prof. Dr. Joachim Wosnitza angefertigt.

Ich erkenne die Promotionsordnung der Technischen Universität Dresden an.

Dresden, den 06. Dezember 2012

Andrey Polyakov